OPTICS STUDIES FOR MULTIPASS ENERGY RECOVERY AT CEBAF: ER@CEBAF

by

N. H. Isurumali Neththikumara
B.S. November 2015, University of Peradeniya, Sri Lanka
M.S. May 2019, Old Dominion University

A Dissertation Submitted to the Faculty of
Old Dominion University in Partial Fulfillment of the
Requirements for the Degree of

DOCTOR OF PHILOSOPHY

PHYSICS

OLD DOMINION UNIVERSITY
December 2023

Approved by:

Todd J. Satogata (Director)

S. Alex Bogacz (Member)

Geoffrey A. Krafft (Member)

Hani El-Sayed Ali (Member)

Helmut Baumgart (Member)

ABSTRACT

OPTICS STUDIES FOR MULTIPASS ENERGY RECOVERY AT CEBAF: ER@CEBAF

N. H. Isurumali Neththikumara
Old Dominion University, 2023
Director: Dr. Todd J. Satogata

Energy recovery linacs (ERLs), focus on recycling the kinetic energy of electron beam for the purpose of accelerating a newly injected beam within the same accelerating structure. The rising developments in the super conducting radio frequency technology, ERL technology has achieved several noteworthy milestones over the past few decades. In year 2003, Jefferson Lab has successfully demonstrated a single pass energy recovery at the CEBAF accelerator. Furthermore, they conducted successful experiments with IR-FEL demo and upgrades, as well as the UV FEL driver. This multi-pass, multi-GeV range energy recovery demonstration proposed to be carried out at CEBAF accelerator at Jefferson Lab focuses on demonstrating highest energy recovery in super conducting linac in the low-current range. Continuous electron beam accelerate up to 7.5 GeV within 5-passes and decelerate in the next 5-passes recovering RF energy and dumps at a low energy dump. The beamline optics design for recirculating linacs require special attention to avoid beam instabilities due to RF wakefields. Usually, multi-pass linac beam lines require stronger focusing at lower energies as that is necessary to avoid beam breakup (BBU) instabilities, even with this small beam current. The CEBAF linac optics optimization is focused on balancing over-focusing at higher energies and beta excursions at lower energies. The race-track-shaped geometry of CEBAF accelerator allows its linacs to accommodate multiple energy beams simultaneously, while individual recirculating arcs transporting one beam energy, are shared between accelerating/decelerating beams. For the linac optics optimization process, an extended strategy is used that is originally used in 6-pass Recirculating Linac design of the LHeC, to represent the ten passes through a single linac. Using proper mathematical expressions, linac optics optimization can be achieved with evolutionary genetic algorithms, with Multi-Objective optimization. This thesis introduces a CEBAF optics redesign tailored to accommodates the ER@CEBAF multi-pass ER scheme. The isochronous arcs were retuned to match into

optics solutions for optimized 10-pass linacs. Within this work, a single bunch particle tracking analysis presented here focuses on the further improvements of the beamline and beam transportation.

To my Family, Teachers, Friends and all everyone who supported me through this journey…

ACKNOWLEDGMENTS

First and foremost I would like to express my sincere gratitude to my supervisor, Dr. Todd Satogata for providing invaluable guidance and unwavering encouragement during my Ph.D. journey. I am thankful to him for accepting me as a student, consistently sharing his knowledge, and particularly for allowing me to explore new paths at my own pace, as well as for his patience and assistance in addressing my weaknesses. I am thankful to my Jefferson Lab mentor, Dr. Alex Bogacz for leading me on this project and offering valuable insights, support, and guidance throughout the journey.

A special thank goes to Dr. Geoffrey Krafft and Dr. Balša Terzić for their introduction to the field of Accelerator Physics and for acquainting me with the Jefferson Lab's Center for Advanced Studies of Accelerators (CASA). A heartfelt appreciation extends to Dr. Ryan Bodenstein and Arthur Vandenhoeke, for helping me during the initial phase of this project. Dr. Bodenstein, being a CASA member has consistently been available to share his knowledge and insights. I am thankful for Dr. Yves Roblin and Dennis Turner, Daniel Moser and Accelerator Operations division at Jefferson Lab, for their immense support on preparation and carrying out of the beam study.

I would like to thank Dr. Hani El-Sayed Ali and Dr. Helmut Baumgart, for serving in my committee and offering valuable feedback during annual evaluation meetings. I would also like to thank all the CASA members at Jefferson Lab, where I have spent almost five years working on multiple projects.

My sincere thanks goes to the Physics Department at Old Dominion University for accepting me as a graduate student and supporting me throughout this journey. I am deeply appreciative of all the graduate program directors for their invaluable guidance, as well as the dedicated academic staff. Additionally, I am thankful for all the support provided by Lisa, Annette and Delicia, during this period.

I would extend my heartfelt gratitude to my family, including my parents and sisters for their unconditional love, encouragement and understanding. Thank you for believing in me and supporting my pursuit of my dreams, even during challenging moments.

A special thanks goes to my friends Dhanushki, Lashika, Jayendrika, Sajini, Subhashini, Bhawin and Bhanuka for supporting me all the way and tolerating me during the times I got stressed. Additionally, I would like to thank all of Sri Lankan friends for their immense support and friendship. I am also thankful for the support and friendship of my colleagues at ODU and Jefferson Lab.

This work is supported by the U.S. Department of Energy under contract DE-AC05-06OR23177. Additional support came from the JSA initiatives fund program.

TABLE OF CONTENTS

Page

LIST OF TABLES

Table Page

LIST OF FIGURES

Figure Page

Figure Page

CHAPTER 1

INTRODUCTION

Modern particle accelerators find diverse applications across a broad spectrum, spanning from high-energy physics colliders to compact accelerators utilized in medical and archaeological research areas. These machines come in various sizes, ranging from a few meters to thousands of kilometers. However, the tendency in accelerator development is gravitating towards the need for high-intensity, shorter bunches with continuous wave beams. The pursuit of developing cost-effective and energy-efficient accelerators has gained continuous interest in the active accelerator community and has led to more research and development work.

Linear accelerators (linacs) are preferred for electron acceleration to high energies as synchrotron radiation limitations that exist in storage rings are absent. The incorporation of superconducting technology and beam recirculation strategies in linacs holds the potential for significant cost savings, particularly concerning real estate expenses. An excellent example of this strategy is the CEBAF accelerator at the Jefferson Lab in Virginia, where a superconducting radio frequency (SRF) accelerating system and five pass beam recirculation methods are effectively utilized.

Chapter 3 section provides a concise introduction to the multi-pass, multi-GeV range energy recovery demonstration that will be carried out at the CEBAF accelerator at Jefferson Lab: ER@CEBAF. Energy Recovery Linacs (ERLs) have the unique capability of accelerating electron beams with the specific linac beam characteristics mentioned above and subsequently decelerating through the same linac line before dumping at a low energy beam dump. The advancement of ERL technologies involves improvements in several sectors, including beam injector, beam optics, beam stability, instrumentation, commissioning, and operation experiences. This drive for improvement served as the motivation behind the research and development work on the ER@CEBAF project as an investigative initiative for the proposed EIC - ERL operations, to identify the difficulties and new challenges as detailed in [2].

The objective of this project is to leverage a Multi-Objective Evolutionary Algorithm (MOGA) process in the optics design task, enabling the generation of optimized optics solutions for the special ten-pass linac lattice. While manual optimization is possible, it may not adequately explore the vast variable space available. Chapter 4 elaborates on the incorporation of MOGA techniques into the optics optimization process. An advantage is taken of the inherent symmetry between two CEBAF linacs in the design of this special linac lattice. This technique has previously proven successful in the LHeC ERL design.

The arcs within the CEBAF lattice are achromats with localised dispersion. The arcs combined with spreaders and recombiners are psuedo isochronous, ensuring that they provide a path length equal to an integer multiple of the RF wavelength. However, to accommodate the additional five passes, these arcs have to recirculate beams by sharing both accelerating and decelerating beam passes. In Chapter 5, the process of redesigning arc optics is detailed, which includes the introduction of four-fold symmetry into the horizontal bends. Isochronous arcs are achieved with the tunable M_{56} method described there. In Chapter 6, the results of start-to-end simulations are outlined, which involve particle tracking through the ER@CEBAF beam using the redesigned optics. The initial section in this chapter describes the transverse optics comparison between the data from the beam and the lattice. Subsequently, the following section focuses on the effects resulting from synchrotron radiation losses. Specifically, it compares variations in energy spread and bunch length.

Chapter 7 provides a comprehensive analysis of the beam study conducted using the redesigned optics for Arc 1 and Arc 2, where the horizontal dispersion was reduced. The initial section of this chapter includes observations of the dispersion and M_{56} correction on these arcs. Followed by the orbit deviation analysis performed using the collected data from the Fast Optics tool.

CHAPTER 2

BEAM DYNAMICS THEORY

This section includes an introduction to the fundamental concepts in accelerator physics, linear beam dynamics, beamline modeling, and energy recovery of beams. preceding sections in this chapter includes background of 6D beam phase space, and theoretical background of energy recovery linacs.

2.1 MAXWELL'S EQUATION OF MOTION

Electromagnetic fields drive the motion of the charged particle beams and acceleration. Particle accelerators are built up with components capable of beam generation, acceleration, and controlled transport with adequate focusing while minimizing beam losses. Throughout this the process, charged particles interact with electromagnetic fields. The relativistic Lorentz force acts on charged particles as they move through electromagnetic fields:

$$\vec{F} = q\left(\vec{E} + (\vec{v} \times \vec{B})\right) = \frac{d(\gamma m\vec{v})}{dt}. \tag{1}$$

Here, q is the charge of the particle that the beam is composed of, γ is the relativistic factor, $\vec{v}$ is the velocity of the moving particle, and $\vec{E}$ and $\vec{B}$ represent the applied electric and magnetic field vectors respectively. The particle motion under the influence of static or varying electromagnetic fields is the purview of beam dynamics. The core principles of beam dynamics revolve around the linear relationship between these field vectors and the variation of particle trajectory from the ideal orbit.

In the non-relativistic regime, transverse particle motion is affected by both electric and magnetic fields. Nevertheless, as transitioning into the relativistic regime, magnetic fields dominate the control of the transverse beam motion. In this context, electric fields primarily contribute for particle acceleration, while magnetic fields are responsible for bending and focusing the beam.

If the $\vec{E}$ is set to zero in Eq. (1), and using the relation of the vector cross product, the force exerted on a charged particle by the magnetic field is calculated using the following

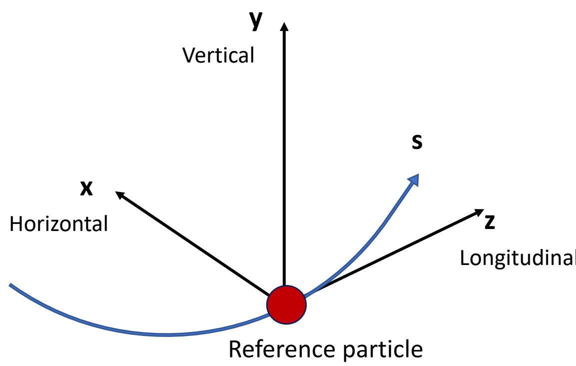

FIG. 1: Coordinate system used in Particle Accelerators, x and y denotes transverse directions and $z(= s - ct)$ denotes the longitudinal position (reproduced from [3]).

relation

$$\vec{v} \times \vec{B} = \begin{vmatrix} i & i & k \\ v_x & v_y & v_z \\ B_x & B_y & B_z \end{vmatrix}. \tag{2}$$

Here x, y and z define the three planes in the Cartesian coordinate system. Force components due to the applied magnetic fields are then expressed as

$$F_x = \frac{d(\gamma m v_x)}{dt} = e\left[v_y B_z - v_z B_y\right], \tag{3}$$

$$F_y = \frac{d(\gamma m v_y)}{dt} = e\left[v_z B_x - v_x B_z\right], \tag{4}$$

$$F_z = \frac{d(\gamma m v_z)}{dt} = e\left[v_x B_y - v_y B_x\right]. \tag{5}$$

The magnetic fields are aligned perpendicular to the direction of motion of the particles, for most common accelrator magnets except solenoids. The coordinate system used in accelerators is illustrated in Figure 1. Therefore transverse velocity components have smaller magnitudes compared to the longitudinal velocity component ($v_{x,y} \ll v_z$), according to the paraxial approximation. The resulting longitudinal force (F_z) component is much smaller compared to the transverse (F_x and F_y) force components.

The equations 3, 4 and 5 are then written as

$$m\gamma\vec{v}^2\,\kappa + e[\vec{v} \times \vec{B}] = 0. \tag{6}$$

In the above equation, $\kappa = (\kappa_x, \kappa_y, 0)$ defines the local curvature vector. Following [1], the local bending radius of the trajectory is defined as

$$\kappa_{x,y} \equiv \frac{1}{\rho_{x,y}}. \tag{7}$$

2.1.1 MULTIPOLE MAGNETIC COMPONENTS

The relations between Eq. (6) and (7) defines the equilibrium particle trajectory balancing the contributions from Lorentz force and the centrifugal force

$$\frac{\gamma m \vec{v}^2}{\rho} + e[\vec{v} \times \vec{B}] = 0. \tag{8}$$

The product of the velocity vetor and the magnetic field vector which is orthogonal to the velocity vector is parallel and opposite to the direction of the centrifugal force. Hence the Eq. (8) reduces to

$$\frac{\gamma m v^2}{\rho} = -evB_{\perp}. \tag{9}$$

The local bend radius (ρ) is now written as

$$\frac{1}{\rho} = \left|\frac{e\,B}{p}\right| = \left|\frac{ec}{\beta E}B\right|. \tag{10}$$

The horizontal bending of a particle trajectory results due to the vertical magnetic field component ($B_y(x)$), and taking the expansion of $B_y(x)$, its components are written as

$$B_y(x) = B_{y0} + \frac{\partial B_y}{\partial x}x + \frac{1}{2!}\frac{\partial^2 B_y}{\partial x^2}x^2 + \frac{1}{3!}\frac{\partial^3 B_y}{\partial x^3}x^3 + \frac{1}{4!}\frac{\partial^4 B_y}{\partial x^4}x^4 + \ldots. \tag{11}$$

Using Eq. (6) and (11) [4]

$$\frac{e}{p}B_y = \frac{e}{p}B_{y0} + \frac{e}{p}\frac{\partial B_y}{\partial x}x + \frac{e}{p}\frac{1}{2}\frac{\partial^2 B_y}{\partial x^2}x^2 + \frac{e}{p}\frac{1}{6}\frac{\partial^3 B_y}{\partial x^3}x^3 + \ldots, \tag{12}$$

$$= \frac{1}{\rho} + kx + \frac{1}{2}mx^2 + \frac{1}{6}ox^3 + \ldots. \tag{13}$$

This field expansion around the reference orbit allows obtaining the field components of magnet elements such as dipoles, quadrupoles, sextupoles, and octupoles. Table 1 lists the definitions of these multipole components and the principal task associated with each component. The CEBAF accelerator design uses more than 2000 magnet elements, including dipoles, quadrupoles, sextupoles, and correctors. The following section includes a brief description of these magnets.

TABLE 1: Dominating multipole field components of each magnet and their primary purpose.

Element	Multipole component	Function
Dipole	$\frac{1}{\rho} = \frac{e}{p} B_y$	Beam steering
Quadrupole	$\mathrm{k} = \frac{e}{p} \frac{\partial B_y}{\partial x}$	Beam focusing
Sextupole	$\mathrm{m} = \frac{e}{p} \frac{\partial^2 B_y}{\partial x^2}$	Chromaticity compensation
Octupole	$\mathrm{o} = \frac{e}{p} \frac{\partial^3 B_y}{\partial x^3}$	Field error correction

The curvature of the equilibrium trajectory in cartesian coordinates can be obtained from analytical geometry as

$$\frac{1}{\rho} = \frac{-x''}{\sqrt{1+x'^2}^3}. \tag{14}$$

Here, x' denotes the time derivative of x and x'' denotes the time derivative of x'. Using paraxial approximation, this term can be simplifies using the assumption of $x' \approx 0$, which leads to the relation $1/\rho \approx -x''$. Then the equation of motion in linear approximation is now written as

$$-x'' = \frac{eB_y}{p} = \frac{1}{\rho} + kx + \frac{1}{2}mx^2 + \frac{1}{6}ox^3 + \ldots. \tag{15}$$

2.2 LINEAR EQUATIONS OF MOTION

The orbital motion in the transverse direction occurs around a closed orbit that is referred to as *betatron motion*. Linearized Hill's equations are used to study motions of these kinds

$$u'' + K(s)\, u = 0, \tag{16}$$

where, u represent transverse coordinates, either x or y. u'' denotes the double time derivative of u. $K(s) = K(L{+}s)$ is the periodic focusing function, for a period structure of length L, while s ($s = \beta ct$) denotes the transformed longitudinal coordinate, depending on time. When dealing with uncoupled particle motion in horizontal and vertical planes, the solutions of Hill's equation can be approached independently for horizontal and vertical planes. There exist three sets of different solutions for Eq. (16) for the cases of $K < 0$, $K = 0$, and $K > 0$.

Considering $K > 0$, the solutions to this equation resemble those of a simple harmonic oscillator, and can be expressed as follows:

$$u(s) = A\cos(\sqrt{K}s) + B\sin(\sqrt{K}s), \tag{17}$$

$$u'(s) = -\sqrt{K}\,A\sin(\sqrt{K}s) + \sqrt{K}\,B\cos(\sqrt{K}s). \tag{18}$$

The notations A and B are the integration constants and their values are determined by evaluating the boundary conditions usually expressed as $u(0) = s_0$, $u'(0) = u'_0$. These systems of linear equations can now be expressed with a system of matrices

$$\begin{pmatrix} u(s) \\ u'(s) \end{pmatrix} = \begin{pmatrix} \cos(\sqrt{K}s) & \frac{1}{\sqrt{K}}\sin(\sqrt{K}s) \\ -\sqrt{K}\sin(\sqrt{K}s) & \cos(\sqrt{K}s) \end{pmatrix} \begin{pmatrix} u_0(s_0) \\ u'_0(s_0) \end{pmatrix}. \tag{19}$$

General formalism of the transfer matrix from position s_0 to s is represented in the equation the equation below

$$\begin{pmatrix} u(s) \\ u'(s) \end{pmatrix} = M(s|s_0) \begin{pmatrix} u_0(s_0) \\ u'_0(s_0) \end{pmatrix}. \tag{20}$$

The $K > 0$ represents the focusing plane solutions

$$M(s|s_0) = \begin{pmatrix} \cos(\sqrt{K}s) & \frac{1}{\sqrt{K}}\sin(\sqrt{K}s) \\ -\sqrt{K}\sin(\sqrt{K}s) & \cos(\sqrt{K}s) \end{pmatrix}. \tag{21}$$

The condition $K < 0$ corresponds to the solutions in the defocusing plane, and the transfer matrix is expressed as

$$M(s|s_0) = \begin{pmatrix} \cosh(\sqrt{K}s) & \frac{1}{\sqrt{K}}\sinh(\sqrt{K}s) \\ \sqrt{K}\sinh(\sqrt{K}s) & \cosh(\sqrt{K}s) \end{pmatrix}. \tag{22}$$

Eq. (20) and (21) denote the transfer matrix of quadrupole magnets in focusing and defocusing planes respectively. Here $s - s_0 = l$ is the length of the quadrupole magnet. Thin-lens quadrupoles are used in the case of $f = \lim_{l\to 0} 1/|K|l$. Then Eq. (20) and (21) reduce to

$$M_{\text{focusing}} = \begin{pmatrix} 1 & 0 \\ -1/f & 1 \end{pmatrix}, \quad M_{\text{defocusing}} = \begin{pmatrix} 1 & 0 \\ 1/f & 1 \end{pmatrix}. \tag{23}$$

The $K = 0$ solutions represent the motion without any external influences, i. e. a drift space. The transfer matrix of a drift space is given in the below equation

$$M(s|s_0) = \begin{pmatrix} 1 & l \\ 0 & 1 \end{pmatrix}. \tag{24}$$

In this context, $s - s_0 = l$ is the length of the drift region.

In the case of a sector bend dipole, the Hill's equation is written as,

$$u'' + \frac{1}{\rho(s)} u = 0. \tag{25}$$

Here, $\rho(s)$ defines the radius of the bending trajectory. The solutions to the Eq. (25) are as follows:

$$u(s) = A\,\cos\theta + B\,\rho\,\sin\theta, \tag{26}$$

$$u'(s) = -\frac{1}{\rho}\,A\,\sin\theta + B\,\cos\theta. \tag{27}$$

In most cases, beam trajectory bends within the horizontal plane. Therefore, the uncoupled transfer matrices for dipoles are expressed as follows [5]

$$M_x(s|s_0) = \begin{pmatrix} \cos\theta & \rho\,\sin\theta \\ -\frac{1}{\rho}\,\sin\theta & \cos\theta \end{pmatrix}, \tag{28}$$

$$M_y(s|s_0) = \begin{pmatrix} 1 & \rho\theta \\ 0 & 1 \end{pmatrix}. \tag{29}$$

An accelerator lattice comprised of various elements such as dipoles, quadrupoles, sextupoles, RF structures, and beam position monitors. When employing linear approximation, motion through an accelerator lattice can be mathematically described using transfer matrices. For a lattice consisting of n elements located at distances $(s_1, s_2, \ldots, s_n)$, their transfer matrices denote as $M(s_1|s_0)$, $M(s_2|s_1)$, $\ldots$, $M(s_n|s_{n-1})$.The product of these individual transfer matrices defines total transfer matrix from element *1* to *n*. Then this can be expressed in a simplified formalism

$$M(s_n|s_0) = M(s_n|s_{n-1}).M(s_{n-1}|s_{n-2})\ldots M(s_1|s_0). \tag{30}$$

This matrix multiplication relation is used for tracking the motion of particles as they traverse through the accelerator. Both existing lattice design and particle tracking software utilize this matrix relation for formulation of linear tracking results.

2.2.1 DISPERSION FUNCTION

A beam composed with hundreds of thousands of particles and these particles have a finite spread of momenta about the design momentum p_0. The variations in momentum within a particle beam lead to deviations from the ideal motion along the designed particle

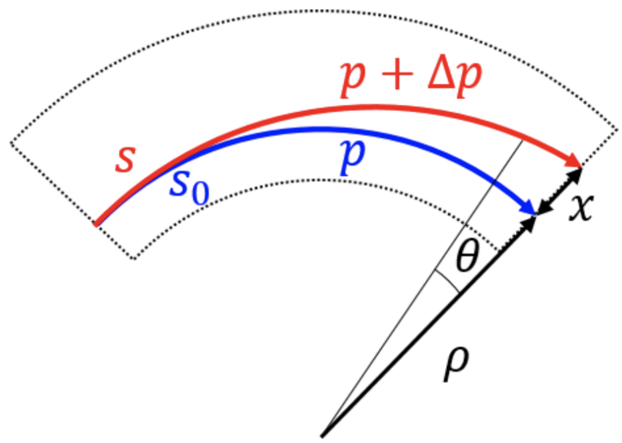

FIG. 2: Off momentum particle orbit due momentum deviation of Δp shown in red color orbit s. The design orbit of a particle with momentum p is denoted with s_0 curve [6].

orbit as illustrated in Figure 2. The Eq. (16) has now taken on the following form, Hill's equation with a perturbed term $\kappa_{0u}(s)\delta$:

$$u'' + \left(\frac{1-\delta}{\rho^2(a+\delta)} - \frac{K(s)}{(1+\delta)}\right)u = \frac{\delta}{\rho(1+\delta)}. \tag{31}$$

Here, δ is the fractional momentum offset coordinate ($\delta = \Delta p/p_0$) and ρ is the bend radius of the perturbed orbit. Since $\delta \ll 1$, this equation is simplified into

$$u'' + \left(\frac{1}{\rho^2} - K(s)\right)u = \frac{\delta}{\rho}. \tag{32}$$

The solution to this linear inhomogeneous equation can be written as a superposition of the particular solution and the solution of the homogeneous equation as $u = u_\beta(s) + D(s)\delta$. The solutions to Eq. (31) are expressed as follows:

$$u(s) = A\cos(\sqrt{K}s) + B\sin(\sqrt{K}s) + \delta D_u(s), \tag{33}$$

$$u'(s) = -A\,\sqrt{K}\sin(\sqrt{K}s) + B\,\sqrt{K}\cos(\sqrt{K}s) + \delta\, D'_u(s). \tag{34}$$

Here, $D_u(s)$ is the transverse dispersion function and $D'_u(s)$ is its derivative with respect to s. The $D(s)$ function is expressed as

$$D_u(s) = \int_0^s \frac{1}{\rho}\left[\sin(s)\cos(\tilde{s}) - \cos(s)\sin(\tilde{s})\right] d\tilde{s}. \tag{35}$$

For a pure sector dipole of length l, bend angle (θ) corresponds to a bend radius(ρ) is defined as $l = \rho\theta$. The solution for Eq. (31) can expressed by expanding the 2×2 matrices obtained for the solutions of Eq. (16) in to 3×3 matrix, including first order chromatic correction terms

$$\begin{pmatrix} u(s) \\ u'(s) \\ \delta \end{pmatrix} = \begin{pmatrix} \cos\theta & \rho\sin\theta & \rho(1-\cos\theta) \\ -(1/\rho)\sin\theta & \cos\theta & \sin\theta \\ 0 & 0 & 1 \end{pmatrix} \begin{pmatrix} u_0(s_0) \\ u_0'(s_0) \\ \delta_0 \end{pmatrix}. \tag{36}$$

The particle motion now depends on the relative momentum spread of the beam as well, hence each particle in the beam can have different path lengths through the dispersive regions.

2.2.2 PATH LENGTH AND MOMENTUM COMPACTION

The path length of the beam bunch is an important parameter, and in linear beam dynamics additional contributions for path length arise when the trajectory bends. For a single particle, total path length is then expressed as:

$$L = \int (1 + \kappa x)\, dz. \tag{37}$$

The reference path, or the ideal design length (L_0) is defined for zero fractional momentum offset. Changes in path length due to betatron oscillations are negligible as it is proportional to the square of the betatron oscillation amplitude. But the path length deviations depend linearly on the relative momentum spread and the dispersion function as denoted by the equation:

$$\Delta L = \delta \int \kappa(z) D(z) dz. \tag{38}$$

The synchronization of particle motion depends on the path length of the beam, and it is a critical parameter for linacs with multiple beam recirculations. The momentum compaction factor (α_c) is defined to determine the path length variation with momentum

$$\alpha_c = \frac{\Delta L/L_0}{\Delta p/p_0} = \frac{1}{L_0} \int_0^{L_0} \left\langle \frac{D(z)}{\rho} \right\rangle dz. \tag{39}$$

The term within the integral in Eq. (39) determines the average path length variations within the dispersion functions at bend magnets. For a particle motion independent of the momentum spread, momentum compaction factor needs to be zero.

2.3 PHASE SPACE AND TWISS PARAMETERS

The previous section briefly outlined the motion of particles in transverse phase space (*x - x' and y - y'*), characterized by their initial parameters. In principle, it is possible to calculate the trajectories of all the particles in the beam, but this approach becomes impractical for a large number of particles. Instead methods from statistical mechanics are used for the studies of dynamics of evolution of a large ensemble of particles. A six dimensional space

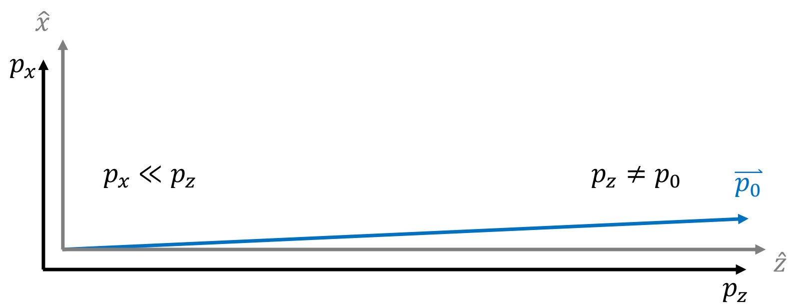

FIG. 3: Diagram illustrating 2D paraxial approximation, p_x and p_z are the transverse and longitudinal momentum components and p_0 is the reference momentum.

representing position and momentum with coordinates $x,\ p_x,\ y,\ p_y,\ z,\ p_z$ is used to denote each particle in the beam. Here, $p_x \approx p_0 x'$ and $p_y \approx p_0 y'$ are the transverse momenta.

Liouville's theorem offers a means to characterize a beam consists of N particles by quantifying the volume occupied by the beam in phase space. Understanding the initial phase space that is occupied by the beam allows to determine the distribution and location of the beam at any place within the transport line without calculating individual particle trajectories.

The area occupied by the particles in the beam is approximated as an ellipse and referred to as the *phase ellipse*. The parameters of the beam ellipse are inter-related as expressed in the Eq. (40). This equation represents the ellipse in $x - x'$ space

$$\gamma\, x^2 + 2\alpha\, x\, x' + \beta\, x'^2 = \epsilon. \tag{40}$$

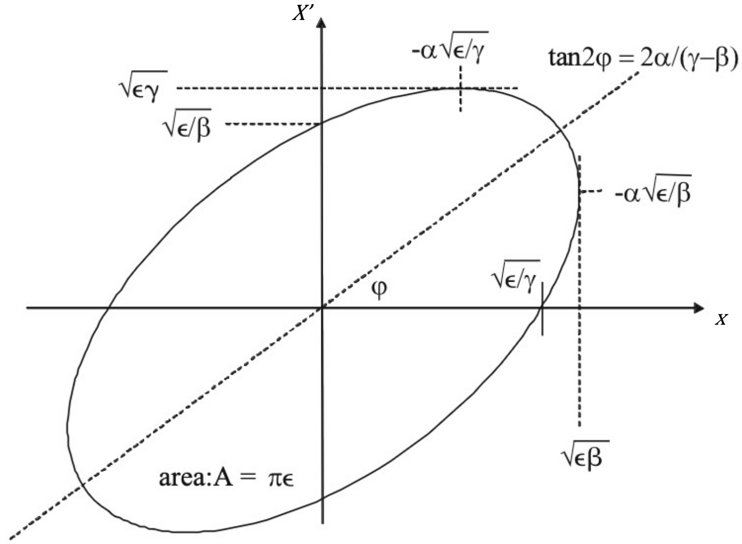

FIG. 4: Beam ellipse in phase space characterizing its shape using Twiss parameters (reproduce from [1]).

Here, $x' = dx/ds = p_x$, and α, β, γ are Twiss parameters which characterize the shape and orientation of the phase ellipse as illustrated in Figure 4. The area enclosed by the phase ellipse is defined using geometric beam emittance (ϵ) and can be expressed as:

$$\int_{\text{ellipse}} dx\, dx' = \pi\, \epsilon = \text{Area}. \tag{41}$$

The phase space ellipse continuously changes its shape and orientation during the propagation of beam along the beamline. The transformation of Twiss parameters is expressed in a matrix formalism from position s_0 to s.

$$\begin{pmatrix} \beta(s) \\ \gamma(s) \\ \alpha(s) \end{pmatrix} = \begin{pmatrix} C^2 & -2CS & S^2 \\ -CC' & CS' + SC' & -SS' \\ C'^2 & -2C'S' & S'^2 \end{pmatrix} \begin{pmatrix} \beta_0 \\ \gamma_0 \\ \alpha_0 \end{pmatrix}. \tag{42}$$

Here, C and S are cosine and sine "like" solutions of the equation of motion starting at s_0 ($s = 0$), and C' and S' are their derivatives with respect to s. The beam parameters at any location within the beamline can be extrapolated using the knowledge of initial Twiss parameters and the relations defined in Eq. (42).

The quantity normalized emittance (ϵ_n) is defined as a relation of momentum and phase space and it is defined as,

$$\epsilon_n = \beta\gamma\epsilon, \tag{43}$$

is an invariant with no dissipative forces present, causing particle losses.

2.3.1 BEAM EMITTANCE

The Eq. (40) represents the beam emittance defined by the area enclosed by the particles of the beam. When the three orthogonal planes (x, p_x), (y, p_y) and (z, p_z) are uncoupled, emittances in each plane are constant. The quantity root mean squared (rms) emittance (ϵ_{rms}) is then defined using the second moments of the particle distribution in each plane

$$\epsilon_{rms} = \sqrt{\sigma_x^2\sigma_{x'}^2 - \sigma_{xx'}^2} = \sqrt{< x^2 >< x'^2 > - < xx' >^2}. \tag{44}$$

Here σ_x and $\sigma_{x'}$ are the rms values of the beam envelope in (x, x') plane.

The Twiss parameters are also known as Courant-Snyder invariant and are then defined in trace space as:

$$\beta_x = \frac{< x^2 >}{\epsilon_{rms,x}}, \tag{45}$$

$$\gamma_x = \frac{< x'^2 >}{\epsilon_{rms,x}}, \tag{46}$$

$$\alpha_x = -\frac{< x\, x' >}{\epsilon_{rms,x}}. \tag{47}$$

These Twiss parameters satisfy the relationship of $\beta_x\gamma_x - \alpha_x^2 = 1$. The rms transverse beam sizes ($\sigma_{x,y}$) are correlated with the beam emittances and follow the relation:

$$\sigma_i(s) = \sqrt{\epsilon_i\beta_i + D_i^2(s)\sigma_\delta^2}. \tag{48}$$

Here, i denotes either x or y and σ_δ denotes the rms relative energy spread of the beam.

The 6D beam motion in phase-space is represented by the similar matrix formalism.

$$\begin{pmatrix} x \\ x' \\ y \\ y' \\ z \\ \delta \end{pmatrix} = \begin{pmatrix} M_{11} & M_{12} & M_{13} & M_{14} & M_{15} & M_{16} \\ M_{21} & M_{22} & M_{23} & M_{24} & M_{25} & M_{26} \\ M_{31} & M_{32} & M_{33} & M_{34} & M_{35} & M_{36} \\ M_{41} & M_{42} & M_{43} & M_{44} & M_{45} & M_{46} \\ M_{51} & M_{52} & M_{53} & M_{54} & M_{55} & M_{56} \\ M_{61} & M_{62} & M_{63} & M_{64} & M_{65} & M_{66} \end{pmatrix} \begin{pmatrix} x_0 \\ x'_0 \\ y_0 \\ y'_0 \\ z_0 \\ \delta_0 \end{pmatrix}. \tag{49}$$

Note that the longitudinal phase space coordinated are now transformed into z and δ, incorporating the time dependence factors of the particle motion.

2.4 THEORY OF ENERGY RECOVERY LINACS

The concept of Energy Recovery Linacs (ERLs) first emerged in 1965 during the proposal for a high-energy electron-positron collider [7]. In colliders, both accelerated beams are dumped after their collision, resulting in significant inefficiency. Enhancing the efficiency of these accelerators becomes feasible when the energy from these accelerated beams can be reclaimed within the same cavities where the initial acceleration occurred. While the concept may seem straightforward, the effective design and implementation depended upon the development of either normal conducting or SRF cavities.

In 1977, the first-ever demonstration of beam energy recovery was demonstrated at the Chalk River Nuclear Laboratory. In a two-pass reflexotron setup, the beam traverses an accelerating structure and then retraces its path through the structure in the opposite direction using a 180° reflecting magnet. The phase of the beam relative to the accelerating structure was obtained by changing the distance between this reflecting magnet and the accelerating structure.

In 1986, the first energy recovery demonstration with superconducting RF cavities was carried out at Stanford University's High Energy Physics Lab (HEPL)[8]. In this setup, a recirculation loop with adjustable path length allowed electrons to traverse the accelerating cavities in either an accelerating or decelerating mode during the second pass of the beam. This marked the initial showcase of same-cell energy recovery within a SRF linac. While the beam wasn't applied for any specific purpose, its clear success was evident in meeting the RF power requirements, thus affirming the feasibility of energy recovery.

The Los Alamos National Laboratory's free electron laser showcased energy recovery through a multi-cavity setup. In theory, this configuration aimed to enhance the overall Free Electron Laser (FEL) efficiency. However, due to losses in the cavities and RF transport, it unexpectedly led to an increase in the overall demand for RF power. Consequently, this led to the selection of nearly lossless SRF cavities in the same-cell energy recovery mode [9].

The progress in Energy Recovery (ER) technology has captured the interest of Free Electron Lasers (FELs), as it has the potential to significantly improve FEL efficiency. In conventional FELs, roughly a 1% of the energy from the accelerated beam is typically converted into laser radiation, while the remaining beam energy is discarded at beam dump. Recovering the supposedly discarded beam power at the FEL's exit has the potential to

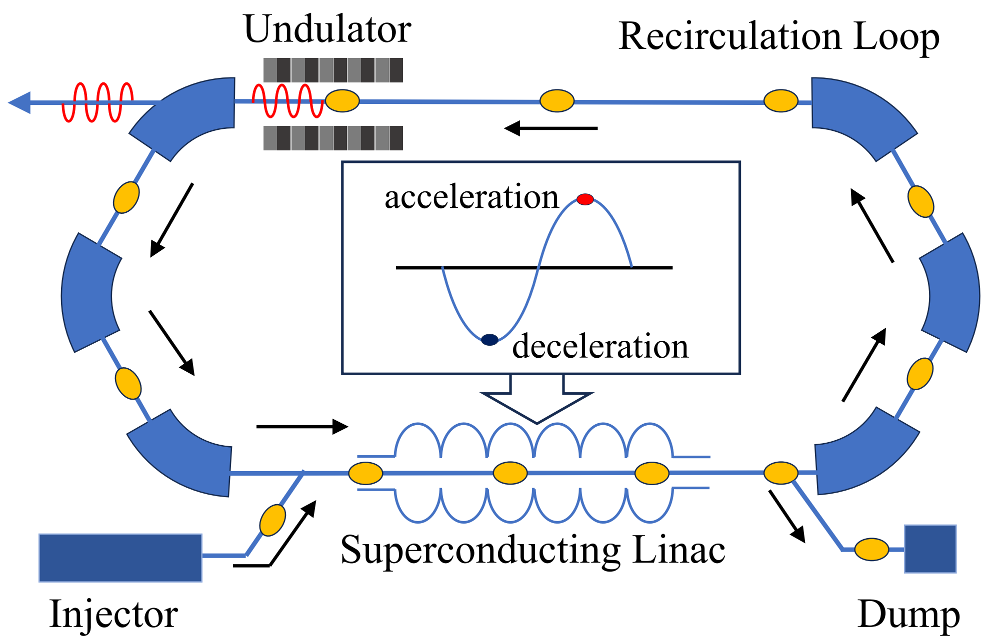

FIG. 5: Schematic of a generic light source based on an ERL (reproduced from [10]).

significantly boost the overall laser efficiency. The Jefferson Lab's IR demo project emerged as a direct outcome of conceptualizing the integration of ERLs into FELs. The utilization of SRF cavities, with features akin to those in CEBAF cryomodules, marked a remarkable success in achieving the initial goals.

ERL technology represents an exceptionally efficient approach for accelerating electron beams with a high average current. This high-current electron beam serves its designated functions, such as serving as a gain medium for FELs, generating synchrotron light, acting as a source for ion beam cooling, or facilitating beam collisions with ions. In most cases, these applications tend to induce significant emittance growth and energy spread in to the electron beam, yet the bulk of the beam's power remains intact. To harness this remaining beam power, the beam is recirculated through the accelerator, undergoing an additional 180° phase shift. During this process, the beam gradually decelerates, transferring its power to the RF system, until it is disposed of with a small residual energy. Figure 5 illustrates a schematic of a generic light source based on ERL technology [10]. The intended purpose here is the generation of synchrotron radiation at the undulator. Since the decelerated beam counterbalance the beam loading effects, ERLs can efficiently accelerate electrons with high average beam current with a modest amount of RF power.

There are three major system benefits of implementing ER technology into an accelerator.

- The required RF power is significantly reduced.
- The dissipated beam power in the dump is reduced by a large factor.
- Dump energy of the electron beam can be reduced, below the photo-neutron threshold which minimizes the activation area of the dump region. This eventually reduces the required shielding of the facility.

2.4.1 FUNDAMENTAL CHALLENGES IN ERLS

The energy recovery linacs hold immensely promising potential, yet there are multiple challenges need to overcome. These can be categorized in to three sections, challenges at injector, superconducting RF and beam dynamics and optics. A brief introduction to some of the important issues are discussed below, particularly focus on the multipass ERLs [11].

Injector

Injector specifications play a pivotal role within a linac, significantly influencing beam quality. The injector complex primarily comprises the electron gun and the booster section, where the beam initialization and initial beam acceleration takes place. Additionally, various elements are incorporated into the injector to further refine and manipulate the beam's quality.

The primary designs for electron guns are based on DC, normal conducting RF or superconducting RF technologies. Key areas of research revolve around enhancing the performance of these gun designs. For delivering continuous wave (CW) beams, one can opt for either a DC gun or a CW-RF gun. Each type of these electron guns has its own technical challenges to assess.

Superconducting RF

There exists numerous challenges in SRF technology to support CW electron beams with a high duty factor. These include maintaining precise beam control of the cavity fields in the presence of microphonics and Lorentz force detuning, maximizing cryogenic efficiency and damping higher order mode (HOM) excitations. In an ERL, SRF devices are implemented in two distinct regions, injector and linac. Energy recovery does not occur in the injector, but does happen at linacs. Therefore, SRF technology in the linacs must effectively address several key aspects, including efficient damping of higher order mode (HOM) excitation, that can lead to beam break-up (BBU) instabilities, which could heavily limit ERL performance. SRF cavities operating at their fundamental frequencies can achieve high quality factors (Q), however, having very high Q values result presence of HOM at these cavities. This results the need of implementing strong HOM damping methods. Recirculating linacs, multi-pass ERLs in particular have very high susceptibility to these instabilities and these can support beams with higher currents.

Incomplete energy recovery can introduce dynamic loading issues in ERLs, and these errors imposed on the energy recovered beam which may arise from either deliberate or accidental sources. It is necessary to incorporate a sufficient RF power headroom within the system to manage rapid RF phase changes in the energy-recovered beam caused by these dynamics. Control of these dynamic loading with fast tuners are challenging.

Regenerative BBU instabilities are more prone to the recirculating linacs, and specially in ERLs. Electron beam interaction with the HOMs of RF cavities in multiple beam passes can cause BBU, which eventually lead to head-tail instabilities in a bunch causing particle losses. However, in the case of ERLs with extended linac lattices, active damping techniques targeting specific HOMs become imperative. One effective approach involves an external feedback system that couples with the cavity voltage, selecting a specific frequency of interest, and returning it at a phase shift of 180°. This can effectively reduce the quality factor of the targeted mode.

Beam Dynamics and optics

The design of accelerators necessitates careful consideration for the proper transportation of beams, ensuring precisely controlled phase-space alignment at their designated user stations. Maintaining the beam quality consistently across the entire system, starting from the electron gun, proceeding through the acceleration sections, bending regimes, merging points, and deceleration areas. ERLs face many common challenges as in other accelerators, despite their different architecture. The following paragraphs provide a concise overview of some key concerns.

ERL beams typically exhibit non-Gaussian distributions, often featuring beam components with notable intensities extending beyond the central core, known as beam halo. Nevertheless, comprehensive investigations into particles with larger amplitudes reveal that these halo particles respond to the applied electric fields in a predictable manner. However, these characteristics introduce complexities into the conventional diagnostics employed to align the beam with the lattice. In high-power ERLs, it is essential to minimize losses to just a few parts per million to prevent potential harm to the beamline components.

There are two primary mechanisms of beam interactions within the beam itself, and they are known as space charge (SC) and coherent synchrotron radiation (CSR). Despite the fact that high-power ERLs are typically engineered with a moderate bunch charge and a high repetition rate, space charge forces wield a significant influence on numerous operational facets within an ERL, impacting both transverse and longitudinal planes. The injector, operating within the sub-relativistic regime, is particularly susceptible to the dominance of space charge forces, making the preservation of beam brightness within this regime a matter of utmost importance. Injecting longer bunches to decrease the charge density by using emittance compensation schemes to preserve beam quality, and accelerating the bunch rapidly to compress it at high energy is the most commonly used mechanism in linacs. The choice of energy at the beam injection requires a careful analysis to optimize all the relevant parameters. In the low-energy regime, transverse space charge forces take precedence, whereas longitudinal space charge forces can pose operational challenges. Asymmetric energy spread gives rise to longitudinal space charge forces, which, in turn, lead to head-tail instabilities.

CSR-driven instabilities are more common in high-intensity ERLs, due to the transportation of shorter electron bunches through dipole magnet, which arises coherent synchrotron radiation emission. These CSR emissions can cause phase-space beam distortion, emittance growth, and beam mismatch in the downstream beamline. However, CSR modulations are intentionally used in ERL-based cooler designs where low-energy beams with lower energy spread are used [12].

Phase-space matching

Achieving precise match in the phase-space is a crucial in an ERLs in both longitudinal and transverse planes. A meticulously matched longitudinal space is essential for the stable transportation of high-current beams, a capability even extended to transporting high-current bunches in a SRF accelerating system. Beam transportation can be accomplished in two ways: on-crest or off-crest. Isochronous transportation systems are necessitated for on-crest transportation. In the case of off-crest transportation, a non-isochronous transport scheme is favored to mitigate energy spread growth linked to RF curvature. Additionally, longer bunch lengths are preferred in SRF systems due to their ability to suppress HOM excitation. In ERL-based Free Electron Lasers (FELs), a notable energy spread is introduced within the FEL interaction zone, and this spread further increases during the energy recovery process. Implementing a precise longitudinal match is essential for compressing this observed energy spread growth while preventing beam losses.

Transverse phase-space matching needs to address the issues of simultaneous transportation of multiple energy beams within a shared linac. This also extends to addressing complexities associated with beam recirculation. When multiple beam energies coexist within an accelerating structure, a primary constraint emerges, which is the delicate balance required for beam focusing across all these energy levels. Low energy beam requires strong focusing to avoid any betatron instabilities without compromising the stability of high-energy passes. Employing multiple focusing techniques such as quadrupole FODO singlet, doublet and triplet focusing arrangements proper transverse phase-space control can be achieved [13].

CHAPTER 3

THE MUTI-PASS ENERGY RECOVERY DESIGN AT CEBAF

Linear accelerators (Linacs) serves as tools that accelerate particle beams over a broad energy range. Unlike ring accelerators, linacs do not possess closed orbits and limitations associated with equilibrium conditions. Hence the beam quality, particularly emittance is primarily determined by the injector. Moreover, the practice of beam recirculation within linacs has become increasingly common, leading to the development of multi-pass linacs. This chapter provides an overview of the world's first large scale Superconducting Radio Frequency (SRF) linac, the Continuous Electron Beam Accelerator Facility (CEBAF). Section 3.3 of this chapter outlines the proposed energy recovery demonstration in the multi-GeV range, utilizing multiple passes within CEBAF.

3.1 CEBAF ACCELERATOR

CEBAF at the Thomas Jefferson National Accelerator Facility is located in Newport News, Virginia. This was the first pioneering large-scale electron accelerator in the world to incorporate SRF technology, combined with multi-pass beam recirculation. Opting for multi-pass beam recirculation is aimed at minimizing the expenses linked to the construction of an extended linac, as well as reducing real estate costs. However, this involves a trade-off, as beam recirculating n times through a linear accelerator with an energy gain of $1/n$ replaces the real estate expenses with the costs of expensive SRF accelerating structures. The accelerator was first designed to deliver 4 GeV polarized electron beam to three experimental halls (Hall A, B and C), with a maximum beam current of 200 µA, and later upgraded to deliver 6 GeV beam [14]. The third CEBAF energy upgrade was successfully demonstrated in 2017, and currently the accelerator is capable of accelerating electron beams up to 12 GeV with a polarization greater than 85%, to the four experimental halls, Hall A, B, C and D as illustrated in Figure 6.

The electron beam is created at an injector complex, where four lasers with frequencies up to 499 MHz sequentially illuminate into a GaAs-based photocathode. The photocathode and its accelerating structure emit polarized electrons up to 300 keV. These electrons are then subjected to various manipulations, including focusing, spin rotations, and acceleration

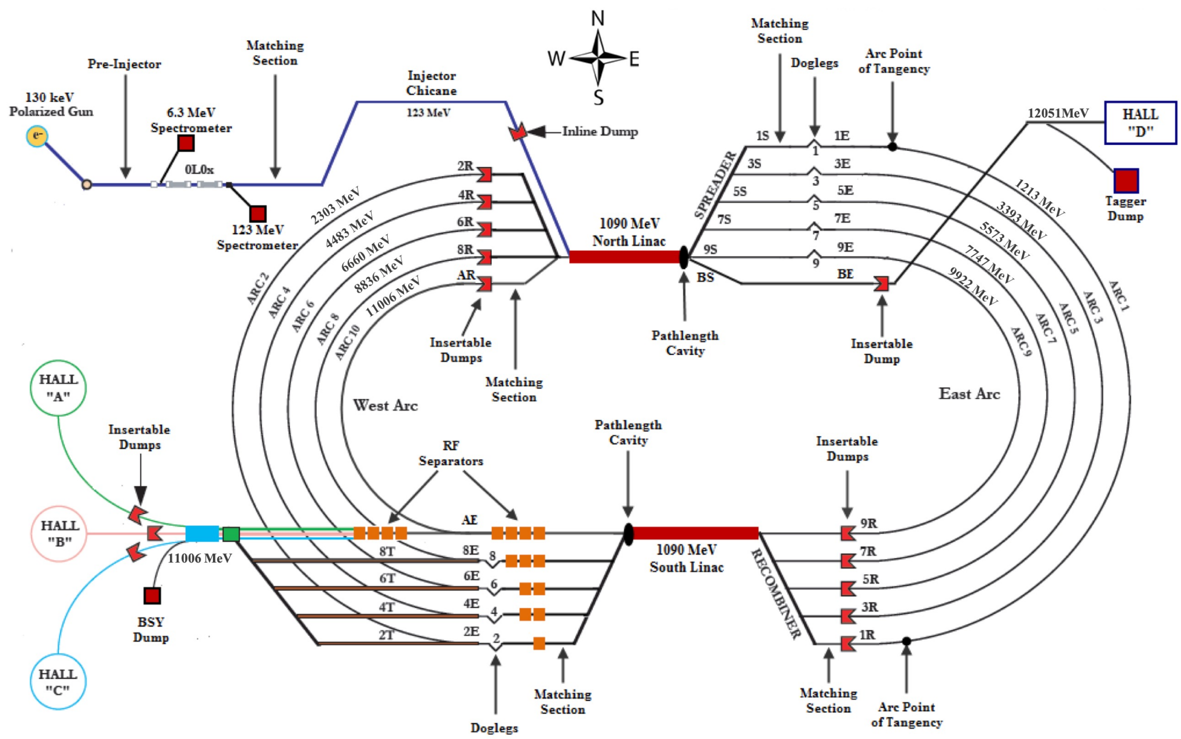

FIG. 6: Layout of the 12 GeV CEBAF accelerator facility [15].

through a series of components such as solenoids, spin rotators, Wien filters, a pre-buncher, and both room-temperature copper cavities and SRF cavities operated at cryogenic temperatures. As a result of this process, the injector accelerates the electron beam up to 123 MeV [16]. Subsequently, efforts are made to scale this energy to align with the energy gain in a single linac for effective beam transportation while lowering the impact from phase slip due to different passes being at different energies. Furthermore, the accelerator must also control the longitudinal phase space of the beam in a manner that minimizes the overall extracted momentum spread.

Following the injector complex, the accelerator complex features a race track-shaped geometry comprising two superconducting linacs: the North linac and the South linac. These two linacs are symmetric and positioned in an anti-parallel manner, connected by ten arcs to form a complete five-beam pass beamline as illustrated in Figure 6. Within the accelerator complex, the beam acceleration takes place in the two linacs. This acceleration occurs within

FIG. 7: A CEBAF 7-cell cavity (C100) with a waveguide higher-order mode coupler (right) and fundamental power coupler (left) [17].

the SRF cavities situated inside cryomodules, which operate at 2 K, which necessitating the use of a cryogenic Helium refrigerator complex.

Each linac comprises twenty five cryomodules with combinations of C20, C50, C75 and C100 RF cavities. The C100 cavities were introduced during the 12 GeV upgrade. They can provide a maximum accelerating voltage of 100 MV. The total maximum energy gain is 1094 MeV per linac pass. Figure 7 illustrates a 7-cell, C100 SRF cavity. The CEBAF operating frequency is 1497 MHz, with the RF wavelength of 20.0 cm.

The 180° bending arcs are interconnected at the linac ends, and their primary function is to ensure beam transportation from linac to linac, ensuring the five pass beam recirculation. These arcs are vertically stacked in two groups, and named as East and West arc segments. Each arc must have a path length equal to an integer multiple of the fundamental RF wavelength of 20 cm, guaranteeing appropriate phasing for beam acceleration. During machine operations, the path length requires slight adjustments and the dogleg dipole magnets are used for this, which are positioned at the extraction region of each arc.

After completing the fifth pass through CEBAF, the beam reaches a maximum energy of 11.02 GeV, disregarding the radiation losses. The delivery of beams into Halls A, B, and C is accomplished using the RF separator magnets. Hall D, on the other hand, receives the beam with maximum energy of 12 GeV with an additional pass through the North linac and synchrotron radiation losses in the last arc [18].

3.2 ENERGY RECOVERY IN CEBAF

In 2003, a single-pass energy recovery demonstration was conducted at the CEBAF accelerator, named CEBAF-ER, with a maximum beam energy of 1056 MeV. This was performed during the 6 GeV operation era with a beam current of 80 µA, hence a linac energy gain of 500 MeV was used [19].

An electron beam with energy 56 MeV comes out from the injector complex and was accelerated up to 550 MeV through North linac. Subsequently, it travelled through Arc 1, reached the South linac, and then progressed through Arc 2. A phase-delay chicane was employed to modify the beam's longitudinal phase by introducing an extra path length of $\lambda_{RF}/2$ at the end of the South linac. As a result, when the beam re-entered the North linac, it became 180° out of phase with respect to the accelerating RF waveform. The decelerated beam was subsequently directed to a dump location, where its energy was brought closer to the initially injected value of 56 MeV. The transverse emittance growth of the energy recovery pass was inconsistent with the accelerating pass emittance growth [20].

At that time, this achievement marked a significant advancement in pushing the boundaries of ERLs since the previous highest energy recovery demonstrated was 48 MeV, achieved through a single SRF cryomodule.

3.3 ER@CEBAF PROPOSAL

The multi-pass, multi-GeV range energy recovery demonstration proposed to be carried out at the CEBAF accelerator at Jefferson Lab is named ER@CEBAF. This proposal is highlighted in the current ERL landscape as illustrated in Figure 8. The dashed lines in the figure are contours of constant beam power [21]. ER@CEBAF marks the highest energy ERL proposal with beam current less than 1 mA.

Utilizing the existing beamline elements, and with a new path length chicane and low energy beam dump, this multipass ER demo could be made a realistic effort. The objective of ER@CEBAF is to perform tolerance and commissioning studies regarding 6D bunch phase

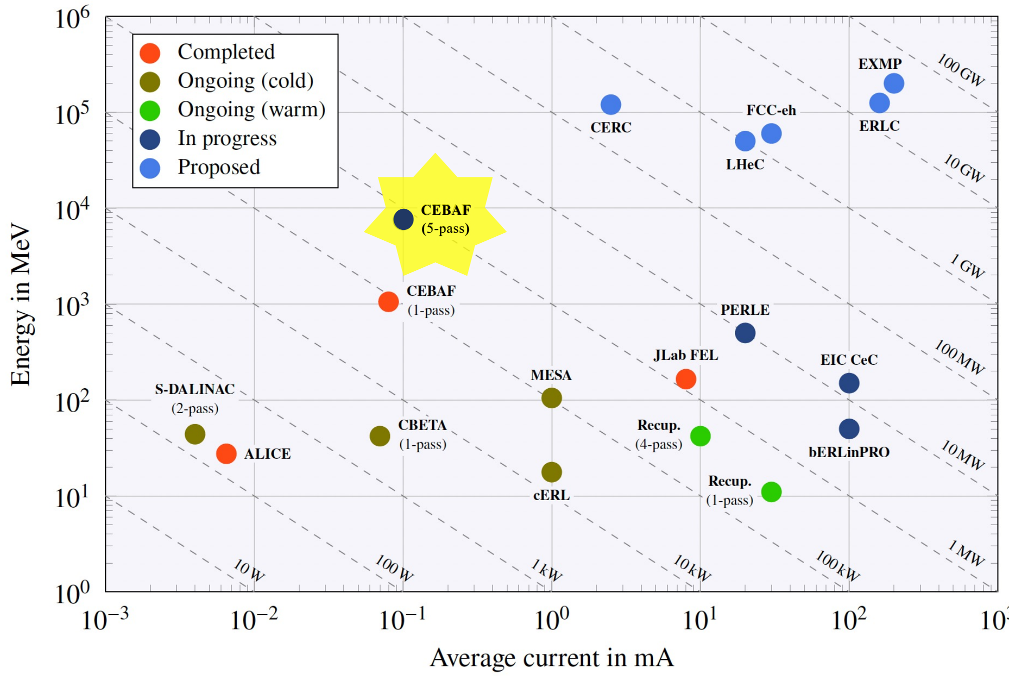

FIG. 8: The ERL landscape with past, present, and proposed ERLs (reproduced from [21]).

space preservation for high-energy ER at 1-pass and at 5-passes [22]. An electron beam would accelerate through five passes, then recirculate through the linacs five more times at a decelerating phase to recover power back into the RF system. During energy recovery, beam decelerates and gets dumped at a low-energy beam dump proposed to be installed at the end of South linac. To facilitate energy recovery, a new path length chicane, providing an additional path length of 10 cm, would be required in highest energy arc (Arc A). The proposed installation sites for both these new hardware segments are illustrated in Figure 9.

The proposed linac energy gain is 700 MeV to 750 MeV based on values obtained with a preliminary longitudinal stability study as described in the project proposal [22]. In the multi-GeV energy range, energy recovery and beam transportation encounter incoherent synchrotron radiation (ISR) energy losses which leads to asymmetry between accelerated and decelerated beam energy profiles. The energy separation between accelerating and decelerating beams needs to be within the arc momentum acceptance, which determines an upper bound to the allowed ISR losses. These energy asymmetries complicate the multi-pass

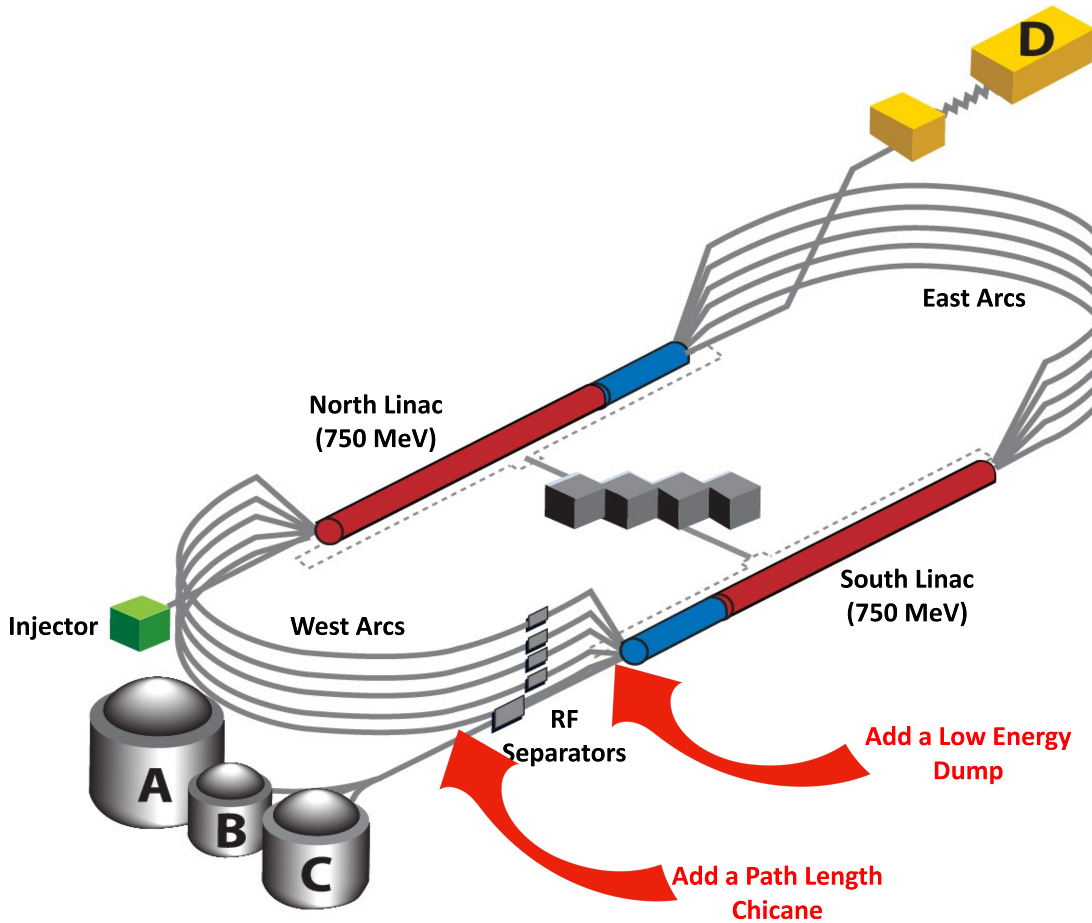

FIG. 9: Layout of the CEBAF accelerator with proposed hardware installation sites (reproduced from [22]).

energy recovery to a great extent, ultimately limiting the energy reach of ER@CEBAF due to recirculating arc momentum acceptance. Having lower dispersion arcs would increase their momentum acceptances, hence low dispersion arcs are preferred for this context. Anti-damping arising with beam deceleration also leads to an energy spread increase, and becomes another important factor determining the maximum energy gain of a linac.

The main machine parameters as listed in the proposal are given table 2, and beam parameters are listed in table 3 [22].

To perform beam diagnostics, energy recovered beam with an energy approximately up to

TABLE 2: Main Machine Parameter List for ER@CEBAF.

Parameter	Values	Units	Description
f_{RF}	1497.0	MHz	Standard CEBAF RF frequency
λ_{RF}	20.0	cm	Standard CEBAF RF wavelength
E_{linac}	700-750	MeV	Energy gain per linac pass
E_{inj}	79-84	MeV	Energy of beam from injector
N_{passes}	5	-	Number of machine passes before energy recovery
$\phi_{FODO,NL}$	60	$^\circ$	Phase advance/cell, North linac
$\phi_{FODO,SL}$	60	$^\circ$	Phase advance/cell, South linac
M_{56} (Arc A)	80-90	cm	M_{56} compression of Arc A
M_{56} (other arcs)	0	cm	M_{56} compression of other arcs
$\theta_{extraction}$	8	$^\circ$	Extraction angle
P_{dump}	20	kW	Maximum dump power (CEBAF standard)
ϕ_{total}	0.25	$^\circ$	Required pathlength control tolerance

TABLE 3: Beam Parameter List for ER@CEBAF.

Parameter	Values	Units	Description
$f_{beam,CW}$	249.5	MHz	Standard CEBAF CW bunch repetition frequency
Tune mode duty cycle	1.5%	-	Tune mode duty cycle relative to CW
$I_{beam;maxCW}$	100	µA	Maximum CW beam current
$q_{bunch;maxCW}$	0.2	pC	Bunch charge (at 100 µA CW)
$\sigma_{bunch,L}$	90-150	µm	Bunch length (high energy)
$\sigma_{bunch,t}$	300-500	fs	Bunch length (high energy)
$\sigma_{bunch,\phi}$	0.16-0.27	$\circ$	Bunch length (high energy)
$\epsilon_{x,y,geom,inj}$	10^{-08}	mrad	Transverse RMS geometric emittance at injector
dp/p_{inj}	$< 10^{-04}$	-	Momentum/energy spread at injector
$\epsilon_{x,y,geom,extraction}$	o(10^{-08})	mrad	Transverse RMS geometric emittance at 10-pass extraction
$dp/p_{extraction}$	2-3%	-	Momentum/energy spread at extraction (ER@CEBAF)

80 MeV, will be extracted to a diagnostic region and directed towards the standard CEBAF 20 kW beam dump. This kind of a beam dump is rated to handle up to 200 µA of continuous wave (CW) beam at 80 MeV.

The optics redesign work performed here for this 10-pass beamline assumes the maximum allowed energy gain of 750 MeV, hence the initial beam energy seen at the entrance of the North linac is scaled to 84 MeV. This initial energy scaling is performed to avoid the phase-slippage errors at the linacs. The maximum energy reach of ER@CEBAF in this configuration is 7.58 GeV.

CHAPTER 4

MULTI-PASS LINAC OPTICS

The ten pass linac lattice constructed from the North linac elements serves as the foundation for the multi-pass linac optics optimization. A multiple objective optimization defined for the search of an optimal solution is performed using genetic algorithms. This chapter explains the Multi-objective optimization (MOO) problem definition and details the implementation process for optimizing the optics.

4.1 MULTI-OBJECTIVE OPTIMIZATION AND PROBLEM DEFINITION

Multi-objective optimization (MOO) refers to the process of optimizing multiple conflicting objective functions simultaneously. In general, the majority of optimization problems involve a single objective to be minimized or maximized. However, in many real-world applications, there are multiple objectives that need to be considered, and these objectives usually conflict with each other. Finding a single global optimal solution is impossible with problems with multiple conflicting objectives. Instead, a set of solutions is obtained by evaluating them according to defined scalar objective functions using a particular set of input parameters within the parameter search space. MOO aims to find a set of solutions that represent the best trade-offs between these objectives, rather than a single optimal solution.

The key concept used in MOO search is the dominance in the solution space, which is used to compare two or more solutions. For a minimization problem dominance is defined as follows.

Take two solutions as x_1 and x_2. If x_1 is no worse for all objectives than x_2 and wholly better for at least one objective, it is said that x_1 dominates x_2, written as $x_1 \prec x_1$.
Thus $x_1 \prec x_2$ iff:

$$F_i(x_1) \leq F_i(x_2) \quad \forall\, i = 1, \ldots, k \quad \text{and} \tag{50}$$

$$F_i(x_1) < F_i(x_2) \quad \text{for at least one } i. \tag{51}$$

Here $F_i(x_1)$ and $F_i(x_2)$ are the values of x_1 and x_2 in objective space and k is the number of objective functions [23].

'Pareto optimality' refers to a set of solutions that dominate all the other solutions at least one objective and cannot be improved in one objective without sacrificing performance in another objective. These solutions represent the best trade-offs among multiple conflicting objectives. The set of all Pareto optimal solutions is known as the 'Pareto front' or 'Pareto set'. The goal of MOO is to search for solutions that lie on the Pareto front, providing a range of trade-offs that decision-makers can choose from based on other considerations outside the model.

The optimization of the 10-pass north linac's optics involves multiple conflicting objectives [24]. Without loss of generality, we consider all of these objectives to be minimized, leading to the following multi-objective problem definition [25]:

$$
\begin{aligned}
&\underset{\boldsymbol{x}}{\text{Minimize}}\, \boldsymbol{F}(\boldsymbol{x}) = [\boldsymbol{F}_1(\boldsymbol{x}), \boldsymbol{F}_2(\boldsymbol{x}), \ldots, \boldsymbol{F}_k(\boldsymbol{x})]^T \\
&\text{subject to} \quad g_j(\boldsymbol{x}) \leq 0, \quad j = 1, 2, \ldots, m \\
&h_l(\boldsymbol{x}) = 0, \quad l = 1, 2, \ldots, e
\end{aligned}
\tag{52}
$$

with m, and e referring to the number of inequality constraints, and equality constraints, respectively. $\boldsymbol{F(x)}$, $g(x)$ and $h(x)$ denote the objective functions, inequality constraints and equality constraints respectively. In general, a solution to such a problem cannot optimize all objectives at once, and instead, one must investigate a set of solutions that fit a predetermined definition for an optimum [25] [26].

Since the number of Pareto optimal solutions to a given problem is large, our goal is to define a multi-objective optimization algorithm that computes the best-known Pareto front, which should ideally be as close as possible to the true front with solutions being uniformly distributed over this front.

4.2 EVOLUTIONARY ALGORITHMS

The majority of search and optimization problems in the real-world involve complexities associated with non-linearities, discontinuity, large dimensionality and mixed nature of variables, multiple disciplines are involved leading classical provable algorithms to be either inefficient, incapable, or ineffective. There are no existing mathematically motivated algorithms to find optimal solutions for all such complex problems within a limited computational time. Thus heuristic search methods, which enable the algorithms to discover solutions using the information about the problem at hand, by learning through the process. Solving much complex real-world problems require higher level heuristic methods, *metaheuristic*, which do not guarantee finding the exact optimal solution, but leads to a nearly-optimal solution in a computationally efficient manner.

Evolutionary Algorithms (EAs) are an interdisciplinary field that draws inspiration from nature and connects biology, numerical optimization, and artificial intelligence. These algorithms serve as metaheuristic search methods, simulating the evolutionary process to iteratively improve problem solutions within a specific environment. EAs operate by modeling the learning process within a population of individuals, where each individual represents a parameter point in the search space and retains knowledge about the environment at each iteration. In the context of evolutionary algorithms, a single iteration is commonly referred to as a 'generation', while each individual within the population is composed of variable vectors called 'genes'.

Solving multi-objective optimization problems with EA enables optimization of all the objectives simultaneously generating a Pareto front.

Three main characteristics of EAs are as follow.

- **Population based :** A group of solutions (individuals) is known as the population and it evolves through each iteration.

- **Fitness oriented :** Every individual in the population and their performances are characterized according to a fitness evaluation. The evolution of the population is based on the principle of 'survival of the fittest'.

- **Variation driven :** Individuals in the population undergo various operations to mimic genetic gene changes.

.

Three different approaches to EA are *Genetic Algorithms* (GAs), *Evolution Strategies* (ESs), and *Evolutionary Programming* (EP) [27]. For the purpose of the optimization work describe later in this chapter, the genetic algorithm technique is adopted.

4.2.1 GENETIC ALGORITHMS

Genetic Algorithms (GAs) are a highly effective class of metaheuristic evolutionary algorithms developed by John Holland in the early 1970s. Solutions in GAs are represented by chromosomes, which are composed of gene vectors. The algorithm begins by creating an initial population of size N, with this population size maintained in every generation. The fitness of each individual is then evaluated using a defined fitness function, and parent individuals for the next generation are probabilistically selected based on their calculated fitness values.

The selected individuals are paired at random to produce offspring and random mutations are introduced into these offspring as well. Due to the higher probability of individuals with greater fitness being selected as parents, these new offspring tend to have higher average fitness values than the previous generation, leading to improved solution space. This process of evolution continues until the termination criteria are met. The termination criteria can be determined in various ways, such as finding a solution that meets the minimum criteria or setting a fixed number of generations. These criteria depend on factors like computational resources or can be based on manual inspection of the solutions [28].

The flowchart given in Figure 10 depicts the key steps involved in an evolutionary genetic algorithm search process.

4.2.2 ELITIST NON-DOMINATED SORTING GENETIC ALGORITHM

In order to sort the population in solution space, each solution must be compared with every other solution. The Fast Non-Dominated Sorting Algorithm (NSGA-II) is a commonly used sorting algorithm used in evolutionary multi-objective optimization procedure. It preserves the diversity of the population explicitly with non-dominated solutions while using the elitist principle, by mitigating the computational complexities. As illustrated in Figure 11 after any generation t, the offspring population $\boldsymbol{Q_t}$ and parent population $\boldsymbol{P_t}$ are combined together. This combined population $\boldsymbol{R_t}$ is classified to different non-dominated fronts as $E_1, E_2, \ldots$. The next generation population is filled using the points of these different non-dominated fronts. This starts from the first non-dominated front (E_1), and continues to E_2, E_3 and so on. The new parent population needs to be in the same size as in the previous generation, hence only a half of this sorted population is chosen, removing all the fronts that cannot be accommodated. *Crowding distance* values are used to select a portion of a sorted front if needed [30].

4.3 MULTIPASS LINAC OPTICS

The race-track topology of the CEBAF machine explicitly requires sharing the same linac and arcs for both accelerating and decelerating beams. This in turn imposes a specific requirement at the linac boundary optics. The Twiss functions need to be identical for both accelerating and decelerating passes that share the same arc corresponding to its converging

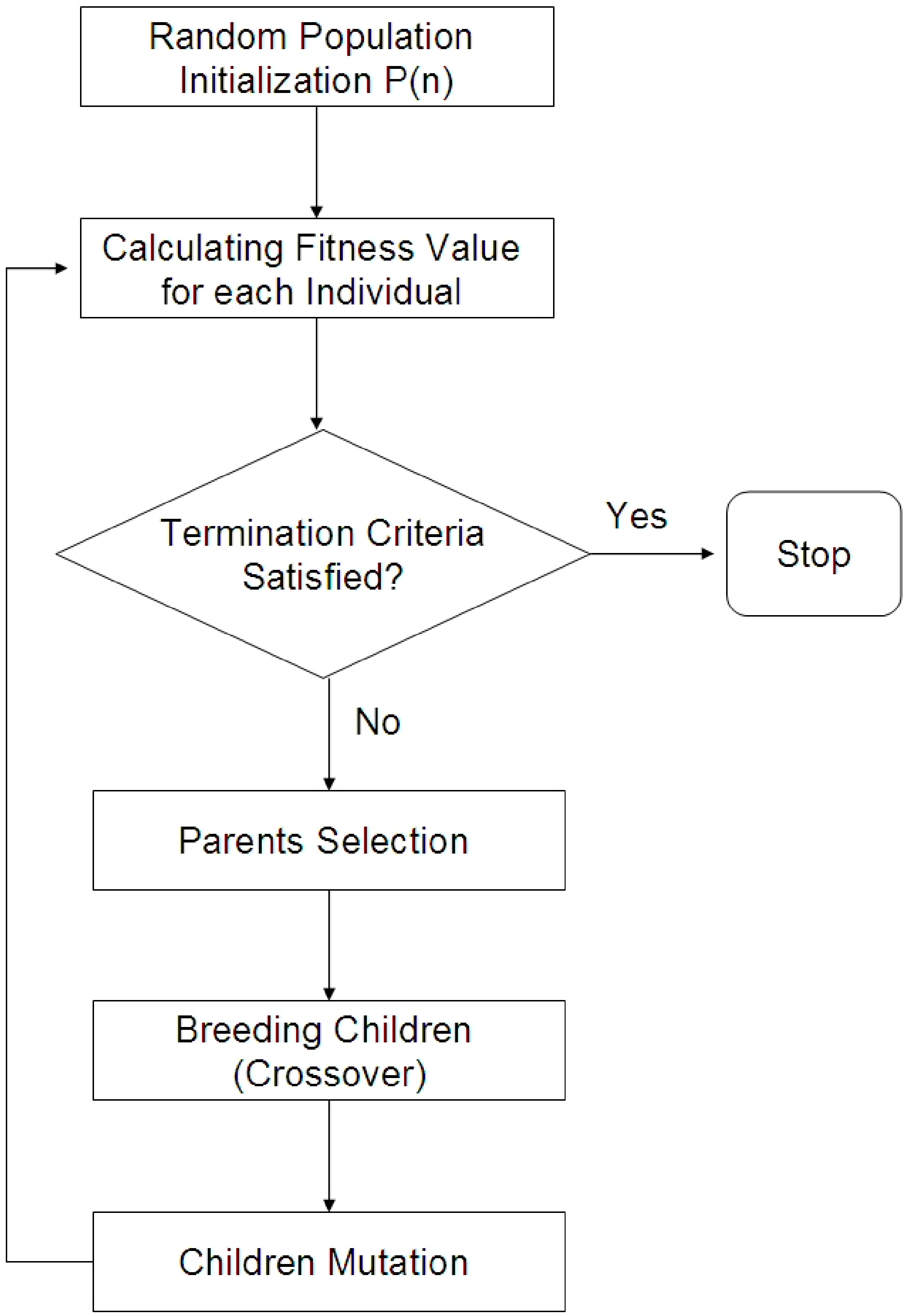

FIG. 10: Flowchart of Evolutionary Algorithm search process (reproduced from [29]).

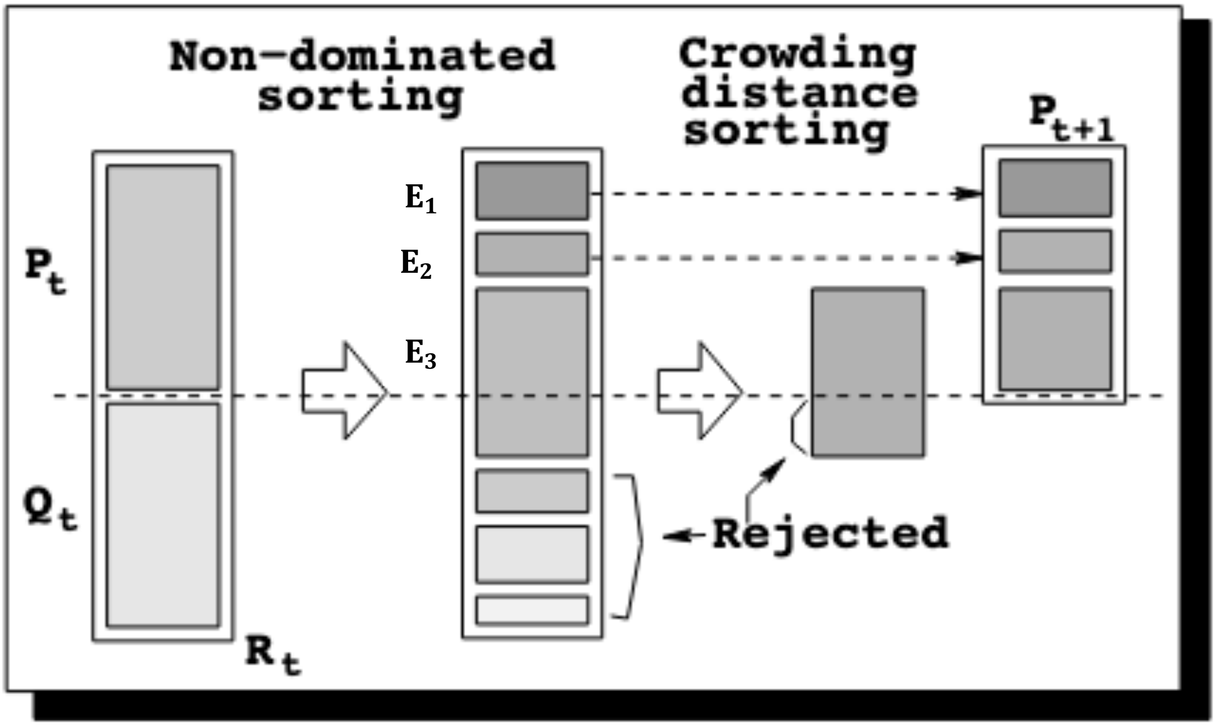

FIG. 11: Schematic of the NSGA-II algorithm (reproduced from [30]).

energy.

The electron beam generated at the injector travels through the North linac, arrives at Arc 1, and bends horizontally to travel towards the South linac and downstream beamline until it completes five passes through the machine to complete the beam acceleration.

During the first five passes, the beam is expected to be at the crest of the RF wave, allowing maximum RF power transfer from RF cavities to the beam, which gains maximum energy. The beam exiting from the South linac at the fifth pass goes towards the highest energy arc, Arc A, and a path length difference of 10 cm is introduced with the use of the added path length chicane. The five energy recovery passes expect maximum energy transfer from the energized beam which then is dumped at the low-energy beam dump with energy close to the injector energy.

The fifth-pass decelerating beam passes through the North linac and goes through Arc 1 and to South linac, then passes toward the low-energy beam dump. Hence ARC 1 needs to be able to pass two energies of beams without allowing any beam losses. Having the same Twiss values at the end of each corresponding pass allows Arc 1 optics design and matching process to be more efficient and symmetric. This requirement is valid for all ten CEBAF arcs. Hence the design of multi-pass ERL optics is much more complicated than the optics design of recirculating linacs.

In order to simplify the process, a special method adopted from LHeC design is utilized, which involves considering all the passes through a single linac [31]. The accelerating and

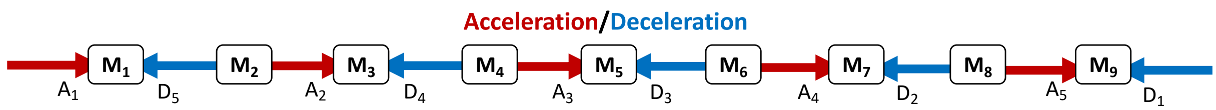

FIG. 12: Representation of accelerating/decelerating passes for North Linac.

decelerating passes of the specific linac are connected alternately through a special zero-length transformation element (M), creating a single beamline. The transformation element M given in Eq. (53) is defined such that it gives the same $\beta(s)$ values before and after that element, but changes the slope of the $\beta(s)$ curve ($\alpha = -(1/2)(d\beta/ds)$), and this can be used to match desired Arc Twiss boundary conditions. Therefore M can be considered as a 'reflective' element.

$$M = \begin{pmatrix} \beta_x \\ -\alpha_x \\ \beta_y \\ -\alpha_y \end{pmatrix}. \tag{53}$$

Accelerating passes are represented by the general linac lattice with a positive RF gradient. Elements are ordered as they are in the CEBAF beamline definition. To denote the decelerating passes, linac elements are arranged in the reversed order in the lattice definition. Interleaving accelerating and decelerating passes are connected using the transformation M. Figure 12, illustrates the ten pass North linac lattice, and the corresponding accelerating

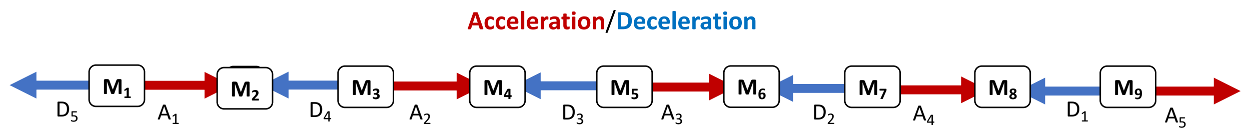

FIG. 13: Representation of accelerating/decelerating passes for South Linac.

and decelerating passes are joined with the M transformation replacing arcs.

The North linac fixes input to *odd arcs* and output to all *even arcs*, whereas the South linac fixes input to *even arcs* and output to *odd arcs*. The North linac lattice contains the elements of the re-injection chicane as these elements are responsible for re-injecting the circulated beam into the North linac. Due to the symmetry of CEBAF linac, the 10-pass South linac arrangement is illustrated in Figure 13.

The initial momentum acceptance studies on ER@CEBAF concluded that the maximum feasible energy gain per linac should be in between 700 -750 MeV to suppress incoherent synchrotron radiation (ISR) energy losses [22]. For the optics studies describe here, a 750 MeV linac gain is considered. The injector beam energy is scaled to match with this new energy gain and calculated to be 84.73 MeV.

Optics design in recirculating linacs that share multiple energy beams simultaneously require special attention to minimize the beam break up instabilities caused by the interactions of the beam and RF system. Resulting RF wake fields can limit the beam current. A threshold current (I_{th}) equation is derived for a two pass beam transportation for pillbox cavity, where subscripts 1 and 2 denote the pass number

$$I_{th} = \frac{2pc}{e\omega Q\frac{R}{Q}} \frac{1}{|M_{12}|\sin(\omega T_{tr})}. \tag{54}$$

Here, Q is the cavity quality factor, p/e is the beam rigidity, ω is the HOM angular frequency and $|T_{tr}|$ is the transfer matrix element. The term $|T_{tr}| = \sqrt{\beta_1\beta_2}\sin(\phi)$ is a measure of displacement at second pass, depends on the $\beta(s)$ function of the second pass. Eq. (54) can be reduced into the Eq. (55), and used for optics optimization to suppress BBU in recirculating linacs by minimizing the left hand side term [32] [33] [34]

$$\left\langle \frac{\beta}{E} \right\rangle = \int \left(\frac{\beta}{E}\right) ds. \tag{55}$$

Prior to this work, a thorough study was carried out to optimize multi-pass ERL lattice optimization using a linear lattice code, *OptiM*. There the linac lattice is arranged as a fodo-like arrangement with 13.5 cells. Optimum phase advance spanning from no focusing (drift linac) to a strongly focusing, 120° per cell. Optimization was a single objective optimization where the aim is to minimize the first pass $\langle \beta/E \rangle$ averaged over focusing (x-plane) and defocusing (y-plane) planes. This is considered to be a driving term for most collective phenomena in Recirculating Linear Accelerators (RLAs). It was found that the linac phase advance of 60° held the optimum value and with slight perturbations to it, an optimum lowest pass linac optics was obtained as in Figure 14 [22].

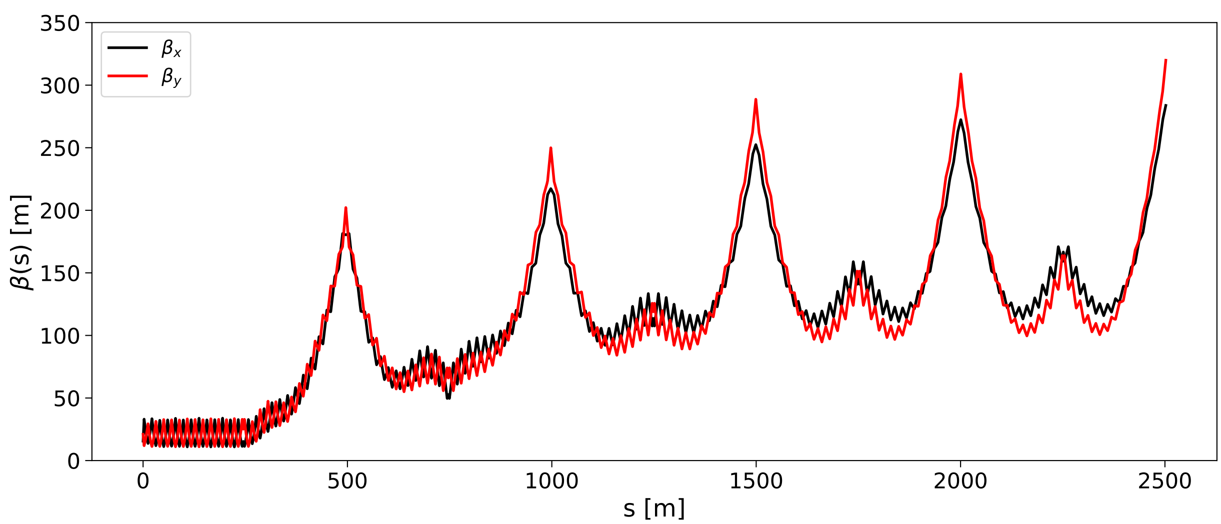

FIG. 14: Multi-pass optics of North linac for 60° FODO-like linac (reproduced from [35]).

Here, the lowest pass β(s) values in both planes are tight and smaller. And the end of even number passes are at peaks, with a partially visible mirror symmetry variation. Required β(s) variation expect the end of all passes to be at peaks, where the differences between the peaks are minimized. Hence, the boundary values for arcs are the same making the arc optics optimization more straight forward.

4.3.1 LINAC OPTICS OPTIMIZATION

Optimization of optics of the 10-pass North linac lattice involves two main goals: minimization of the fluctuations of β(s) function in lower energy passes (< 1 GeV) in order to suppress the beam break-up instabilities occurring due to RF wake-fields, and to control of the peaks of β(s) functions with mirror-symmetric variations for higher passes, while keeping β_x(s) and β_y(s) values as closer as possible at each element. Achieving this second goal is much more important as each accelerating and decelerating pass that converges to the same energy is required to share the same arc. Hence boundary Twiss values of these two passes should be identical to avoid beam losses at arcs due to Twiss mismatch.

The two linacs at CEBAF, are symmetrical to each other and each contains 27 quadrupole magnets. To simplify matters, both linac lattices are designed in a symmetric fodo-like arrangement with 13 cells. The last quadrupole is left with zero field [35].The optics optimization problem for the North linac involves 30 variables: magnetic fields for 26 quadrupole magnets and 4 initial Twiss values of this ten pass beamline lattice.

Due to the 30 variables involved, the search space for the problem is large, and identifying a suitable search space can be complicated. Therefore, systematic studies were conducted with varying objectives and increasing numbers of variables. Initiation of the optimization procedure was done systematically, starting with 4 variables. The used model corresponds to the lattice of Figure 12. The initial optimization model used two objective functions given in Eq. (56) - (57).

To minimize and tighten the $\beta(s)$ variation of the lowest pass according to Eq. (55), the $(\beta(s)/E)$ ratio at each focusing (qf) and defocusing (qd) quadrupole is used. Twiss parameter characterization uses focusing and defocusing quads for horizontal and vertical planes, respectively. The average $(\beta(s)/E)$ for each pass is calculated for each plane separately, and then these 10 values are averaged. To couple both planes, the first objective function is defined as the mean of these two average values, where sums are taken over ten passes and quadrupole instances:

$$F_1 = \frac{\frac{1}{10}\Sigma_{i=1}^{10}\left[\frac{1}{n}\Sigma_{i=1}^{n}\left(\frac{\beta_x}{E}\right)_i^{\mathrm{qd}}\right] + \frac{1}{10}\Sigma_{i=1}^{10}\left[\frac{1}{n}\Sigma_{i=1}^{n}\left(\frac{\beta_y}{E}\right)_i^{\mathrm{qf}}\right]}{2}, \tag{56}$$

$$F_2 = \frac{\frac{1}{n}[\Sigma_{i=1}^{n}\beta_x + \Sigma_{i=1}^{n}\beta_y]}{2}. \tag{57}$$

Initially, the quadrupole magnets located at the end of the North linac were varied, followed by introducing pairs of quadrupole magnets with opposite polarities with increasing search dimensions. However, as the number of optimization variables increased, the effectiveness of the two employed objective functions began to diminish. As a result, multiple constraints were included in the optimization process. The successful initial results were obtained with two objectives listed above, up to 10 variables [36], along with three constraints listed:

$$G_{1,2} = \beta^{\text{first pass}}_{\text{x-max,y-max}} - 40\text{ m}, \tag{58}$$

$$G_3 = (\Sigma\beta_{yi} - \Sigma\beta_{xi})^{\text{arc}} - 40\text{ m}. \tag{59}$$

Using the model North linac lattice with 60° phase advance per cell, the defined objective functions were able to optimize the linac lattice optics up to 10 variables. Eventually, it was determined that a new set of objective functions was necessary. Ultimately, three new objectives were identified and utilized in the 30-variable optimization process.

Defining the new objectives focused mainly on the required optics of the ten-pass linac lattice. The previous study emphasized that there is a counterbalance between tightening the lowest pass $\beta(s)$ variation and preserving mirror symmetry $\beta(s)$ variations in higher passes.

The development of the new objectives primarily revolved around the desired optics of the 10-pass linac lattice. Previous studies highlighted the need for a delicate balance between regulating the lowest pass $\beta(s)$ variation and maintaining mirror symmetry of $\beta(s)$ variations in higher passes. Consequently, a new set of functions was formulated to address these key concerns, resulting in a final set of three objective functions (F_1, F_2, F_3).

The first objective function was defined focusing on the controlled variation of β(s) in both horizontal (x) and vertical (y) planes. It is critical to have a symmetric variation of $\beta(s)$ in both planes, hence the differences between $\beta_x(s)$ and $\beta_y(s)$ values at each element should be minimized. For the purpose of smoothing out the $\beta_x(s)$ and $\beta_y(s)$ curves, simple moving averages of both curves are calculated separately using the Eq. (60)

$$\text{Moving Average (MA}_j) = \left(\frac{1}{k}\right) \times \Sigma_{i=j-1}^{j+k-1} a_i. \tag{60}$$

where, MA_j is the simple moving average of the j^{th} window, k is the window size, a_i is the i^{th} element, which is the $\beta(s)$ value of the i^{th} element.

By analyzing the results of moving averages computed using various window sizes, a window size of $k = 50$ was selected. The mean squared error (MSE) of these calculated moving average values is calculated while minimizing this quantity helps to achieve the primary goal of the optimization

$$F_1 = \mathrm{MSE}[\mathrm{MA}(\beta_x), \mathrm{MA}(\beta_y)]. \tag{61}$$

The ideal solution of the optics of the 10-pass beamline exhibits $\beta(s)$ peaks at the end of each linac pass. The second objective function aims to regulate these peak values. The peak $\beta(s)$ values are computed for each pass assuming the ideal scenario, followed by the determination of the mean value for each plane. The second objective function involves minimizing the geometric mean of the two calculated means to attain the desired outcome, coupling x and y planes as in Eq. (62)

$$F_2 = \prod_{i=x,y} \left[\frac{1}{n} \Sigma_{i=1}^{n} \beta_{\mathrm{i,max}} \right]. \tag{62}$$

Here n is the number of linac passes.

The third function aims to address the issue of suppressing the peak $\beta(s)$ values further. It has been observed that excessive suppression of peak $\beta(s)$ values can lead to a transformation of the end-peaks to end-minima, which can adversely affect the beamline optics. This tends to destroy the preferred mirror-symmetry variation of β(s) in higher passes. In this context, only the peak values of the second, third, fourth, and fifth passes are considered for the final objective definition. These specific peak values are selected because they exhibit a higher sensitivity toward becoming minima. By focusing on these peaks, this objective can effectively regulate the $\beta(s)$ behavior and prevent any undesirable transformations from occurring

$$F_3 = \prod_{i=x,y} \left(\Sigma_{n=2}^{5} |\beta_{\mathrm{i-max}} - \beta_{\mathrm{i+1-max}}| \right). \tag{63}$$

In addition to the three above mentioned objective functions, two constraints are also incorporated into the problem definition. These constraints are designed to regulate the β(s) fluctuations in the lowest energy pass, ensuring that they remain within acceptable limits. By incorporating these constraints, the optimization process can effectively balance the various parameters of the beamline, ensuring that it remains stable and reliable throughout the process. This targeted approach can help to improve the overall performance of the beamline, delivering optimal results for the intended application [37]:

$$G_1 = \beta_{x,\mathrm{max}}^{1^{st}\mathrm{pass}} - 60\ \mathrm{m}, \tag{64}$$

$$G_2 = \beta_{y,\mathrm{max}}^{1^{st}\mathrm{pass}} - 60\ \mathrm{m}. \tag{65}$$

The optimization problem was formulated using the Python framework, ***pymoo***[38], which integrated `Elegant` [39] lattice input and output files. By utilizing these tools, the Twiss output of each lattice setting obtained from the population can be calculated and analyzed. This enables a comprehensive analysis of the beamline's behavior, allowing for targeted optimization of specific parameters.

The optimization process for the 10-pass North linac lattice's optics was systematically carried out by increasing the number of variables, population size, and generation numbers to iterate. This approach allowed for a comprehensive search of the variable space and ensured that all possible solutions were considered. By gradually increasing the number of variables, population size and generation number the optimization process became more refined, and the system was better able to identify optimal solutions.

The termination criteria for this evolutionary search optimization was defined by the generation number. However, due to the larger dimensionality of the 30-dimensional search problem, a significantly larger population size was necessary, resulting in extensive computational time.

The optimization problem with 30 variables ultimately employed three objective functions, and the population consisted of 500 individuals generated randomly within a given range for each variable. Each individual represents a unique lattice setting resulting distinct optics output.

4.3.2 REDUCTION OF SEARCH SPACE

To explore the large search space in this optimization problem with a high-dimensional parameter space, a large population size is necessary, resulting in a considerably large generation number. Both these contributed to the required computational time, which eventually exceeded the maximum allowed walltime in Jefferson lab's scientific computing cluster. The next challenge was to reduce this computational time. Decreasing the generation number was the first suggestion, without complicating the problem. Various methods for reducing the generation number were explored until a reduction in the search space was achieved.

The present study utilized the Pareto front individuals from the 30-variable search with 200 generations. However, upon examining the magnetic fields of these individuals, it became apparent that this set of solutions did not encompass the entire variable space outlined in the problem definition.

The box plots presented in Figure 15 depicts the variations in the fields of 26 quadrupole magnets within the CEBAF North linac lattice. It can be inferred from the plot that most of

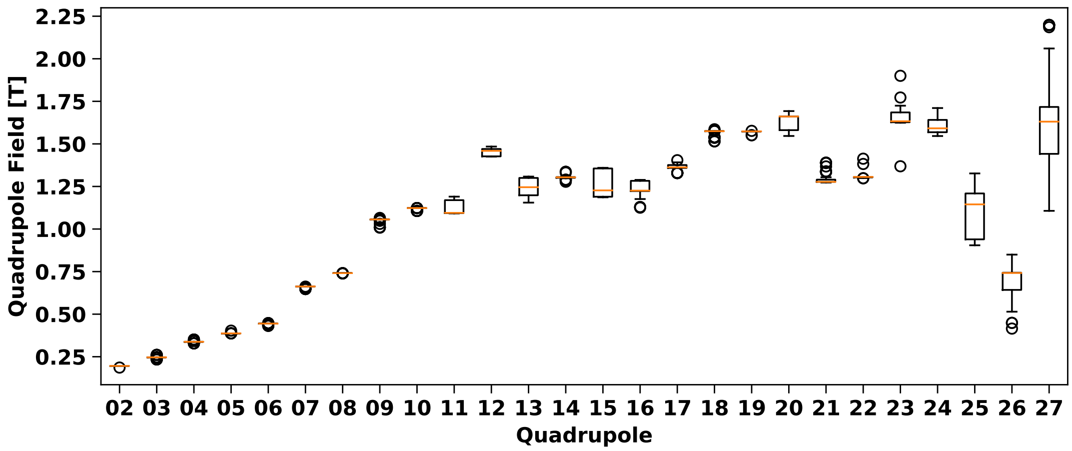

FIG. 15: Magnetic field variation of the Pareto Front for a population size of 500 with a 200 generations iteration.

the quadrupole fields exhibit only minor variations in their field values. Quadrupoles labeled as 02 - 12, show a field variation less than 0.25 T, while the quadrupoles towards the end of the linac lattice exhibit a comparably wider range of field variations. Therefore, it was decided to limit the initial variable space allocated for the magnets with lesser field variations. This was achieved by modifying the upper and lower bounds for the corresponding variables in the problem definition.

By reducing the search space, the evolutionary search could converge efficiently with a lower number of generations, resulting in a significant reduction in required computational time. This allowed us to achieve a Pareto front with a satisfactory number of individual lattice settings. The analysis of optics was performed on the Pareto front individuals obtained after 250 generations, which served as the termination condition for the search.

4.3.3 RESULTS FROM THE MULTI-OBJECTIVE GENETIC ALGORITHM OPTIMIZATION

The three objective functions, as described previously were used for the 30-variable search with the reduced search space. A population of 500 lattice settings was utilized for generations 200, 225, and 250.

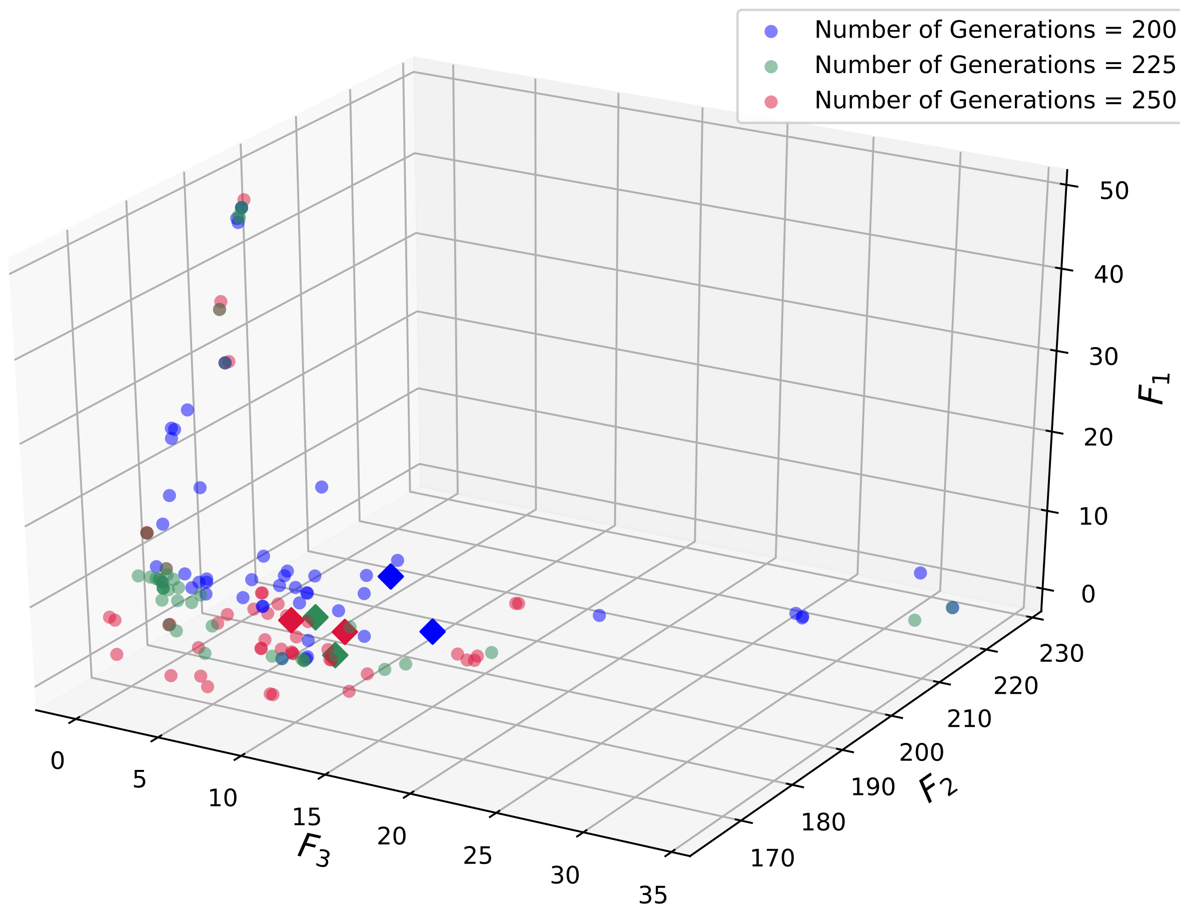

FIG. 16: Pareto fronts for a population of 500 for three different numbers of generations, 200, 225 and 250 in the objective space.

The three different Pareto fronts resulted from the different termination criteria mentioned above are illustrated in Figure 16. In accordance with Figure 16 Pareto fronts obtained with 250 and 225 generations have smaller F_2 values compared to the values of the Pareto front of the 200 generations. Moreover, the majority of the Pareto front individuals of 250 generations have a lower F_1 value compared to the other two Pareto fronts. Some of the solutions are located far from the converged area, indicating the conflicting nature of minimizing all three objectives simultaneously. These outlier points dominate others at least in one objective space (F_1, F_2, F_3). Analysis of the optics of all the Pareto front individuals was performed and acceptable lattice settings were separated. The number of acceptable lattice settings obtained in different search trials are listed in the Table 4.

TABLE 4: Number of solutions in the Pareto Front, solutions with acceptable optics for 30-variable search.

Generations	No. of solutions in PF	No. acceptable Lattices	% of acceptable lattices
200	52	9	17.3 %
225	42	5	16.7 %
250	51	33	64.7 %

The iteration of 250 generations led to a higher percentage of acceptable solutions. Therefore, the solutions obtained from this final search with 250 generations were used to create the 10-pass beamline. The North Linac optics settings for the ER@CEBAF are based on the selected individual with the desired optimized Twiss variations. In the Figure 16, individuals marked with '♦' symbol are chosen for the optics comparison and their β(s) functions are given in Figures 17, 18 and 19.

Figure 17 represents optics of two individual lattice settings for 200 generations. The differences between peak $\beta(s)$ in both planes are not minimized properly. Also the differences between $\beta_x(s)$ and $\beta_y(s)$ need to be further reduced. This agrees with the observations from the Pareto front comparison. With 200 generations, chosen solutions lay farther in F_2 and F_3 spaces compared to others.

As illustrated in Figure 18, both solutions give nearly optimized $\beta(s)$ variations. Higher energy passes have drift linac-like $\beta(s)$ variations in both x and y planes, with tightly controlled $\beta(s)$ in the lowest energy pass. The preferred peak at the end of the third linac pass tends to become a minimum in most of the solutions. This is due to a result of the reduction of the peak $\beta(s)$ values causing over focusing in low energy passes. The reason for performing the search with 250 generations is to verify that the search follows desired optics

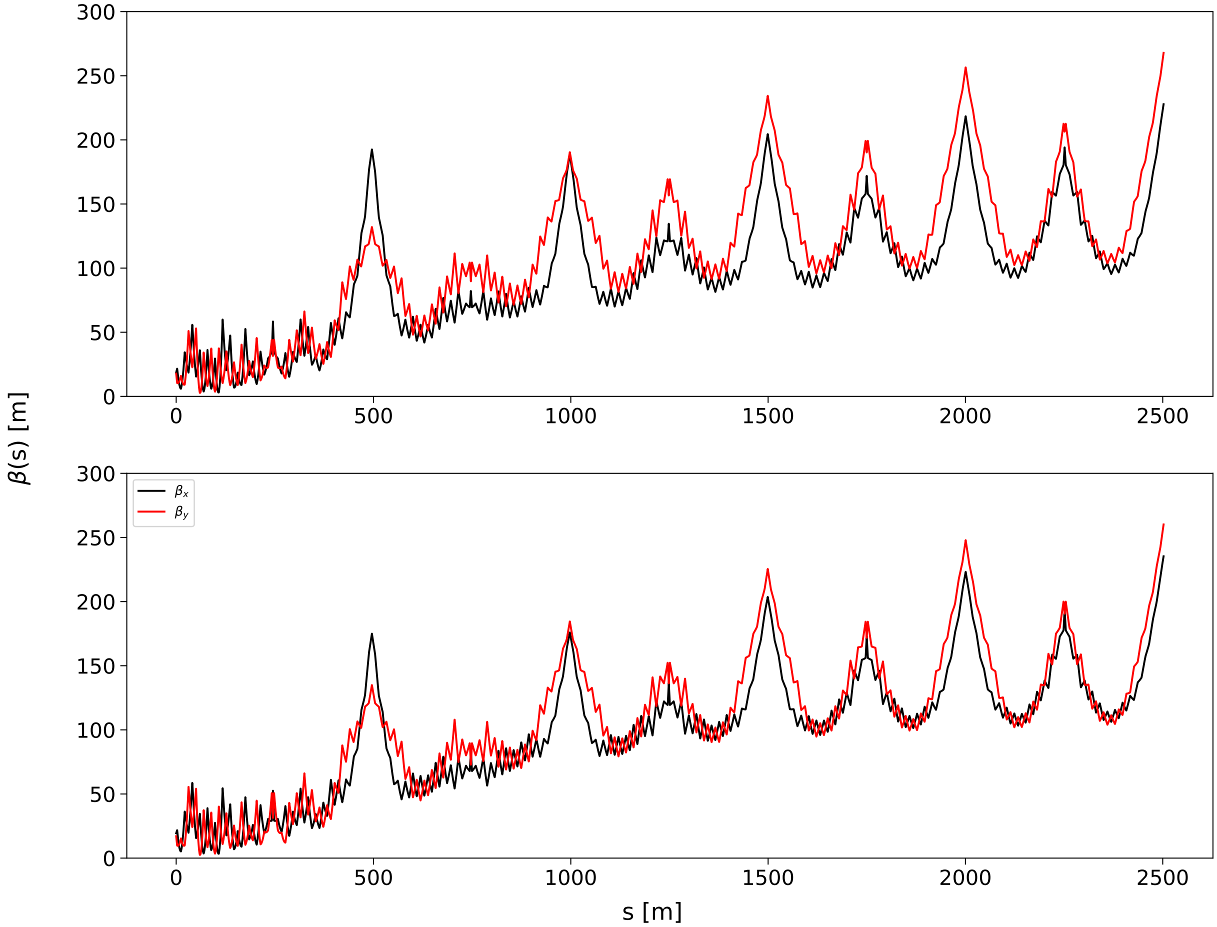

FIG. 17: Optics of two solutions obtained with iterations of 200 generations.

trend if the termination generations are extended, determining the validity of the objective functions used. Figure 19 represents $\beta(s)$ of the two individuals from the search with 250 generations.

It was verified that with the increasing generation number, the optimization search provides more acceptable solutions. But due to the contradictory nature of the three objective functions used, a few individuals ended up with the overly focused $\beta(s)$. This is acceptable as it is the nature of the individuals in a Pareto optimal set as there should be at least one solution that dominates either objective.

According to Figure 19, the features of the Twiss functions through the ten pass North

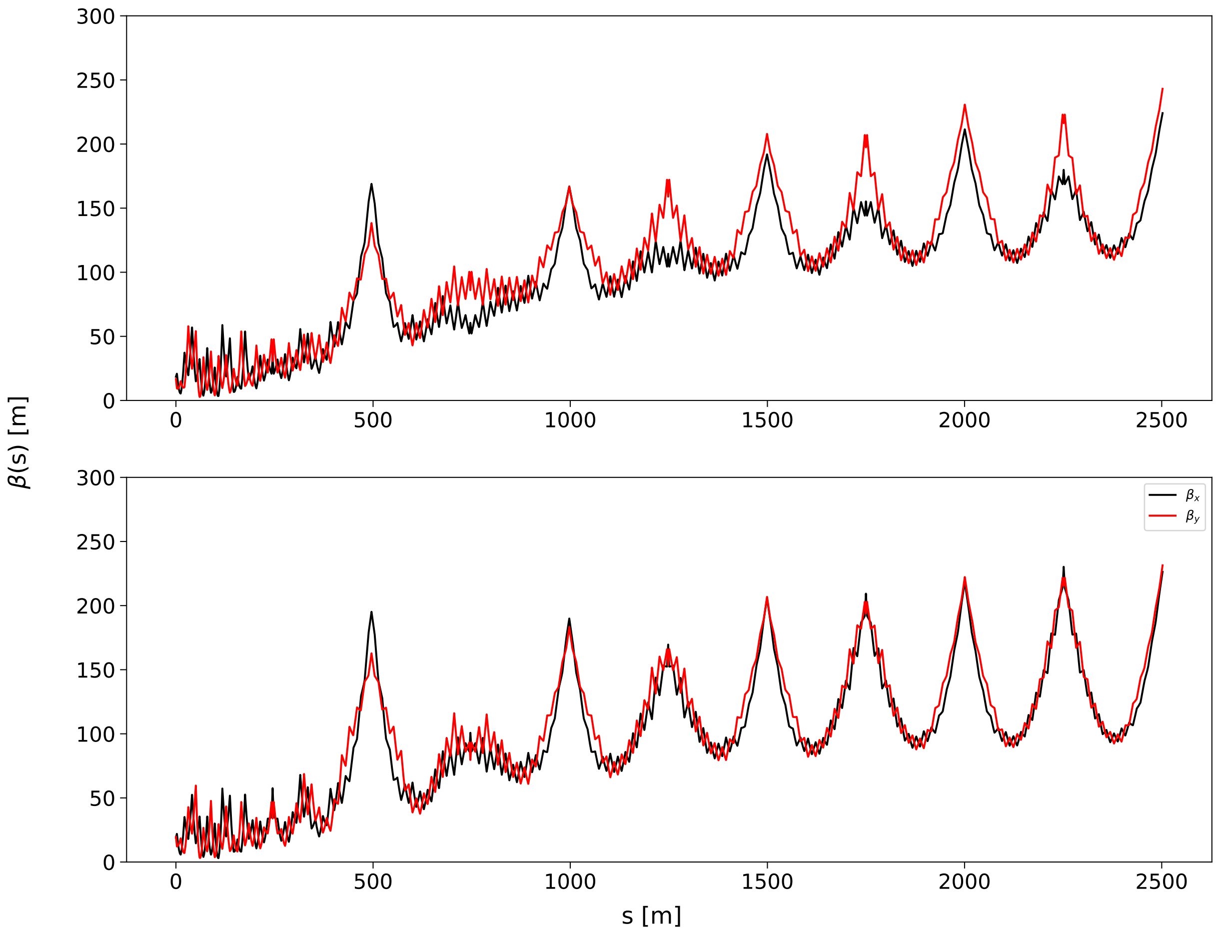

FIG. 18: Optics of two solutions obtained with iterations of 225 generations.

linac lattice are improved.

4.3.4 SOUTH LINAC TEN PASS BEAMLINE

The CEBAF linacs, both South and North, feature a symmetric layout of beamline elements. Leveraging this symmetry, the optimized lattice settings obtained from the ten pass North linac beamline could be applied to the ten pass South linac beamline to derive a solution. Since the reinjection chicane portion is not present in the South linac beamline, minor adjustments were made to the last few quadrupole magnets to incorporate the optimized magnet settings obtained from the North linac beamline. Figure 20 illustrates the Twiss

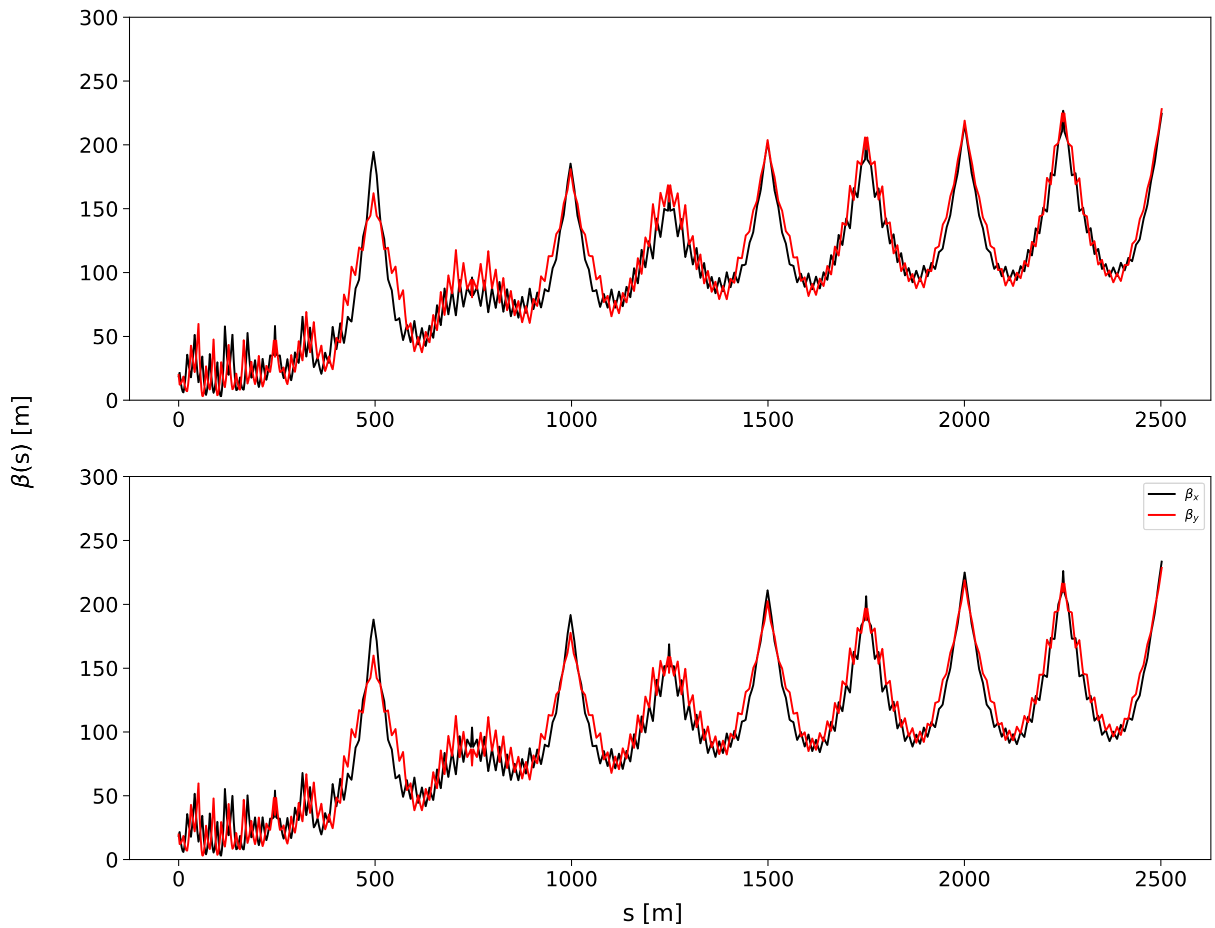

FIG. 19: Optics of two solutions obtained with iterations of 250 generations.

plot of the obtained lattice setting for the ten-pass beamline for South linac.

A single lattice setting from the optimized North linac, from the resulted Pareto front from the search of 250 generations is chosen to be used in the ten pass ER@CEBAF beamline. The South linac lattice optics is also obtained from the solutions from this optimized North linac lattice. The linac passes were segmented from the ten pass beamline and determined the values of Twiss functions $(\beta_x(s), \beta_y(s), \alpha_x(s)$ and $\alpha_y(s))$ at the linac pass boundaries connecting the ten CEBAF arcs, which will be discussed in the next chapter.

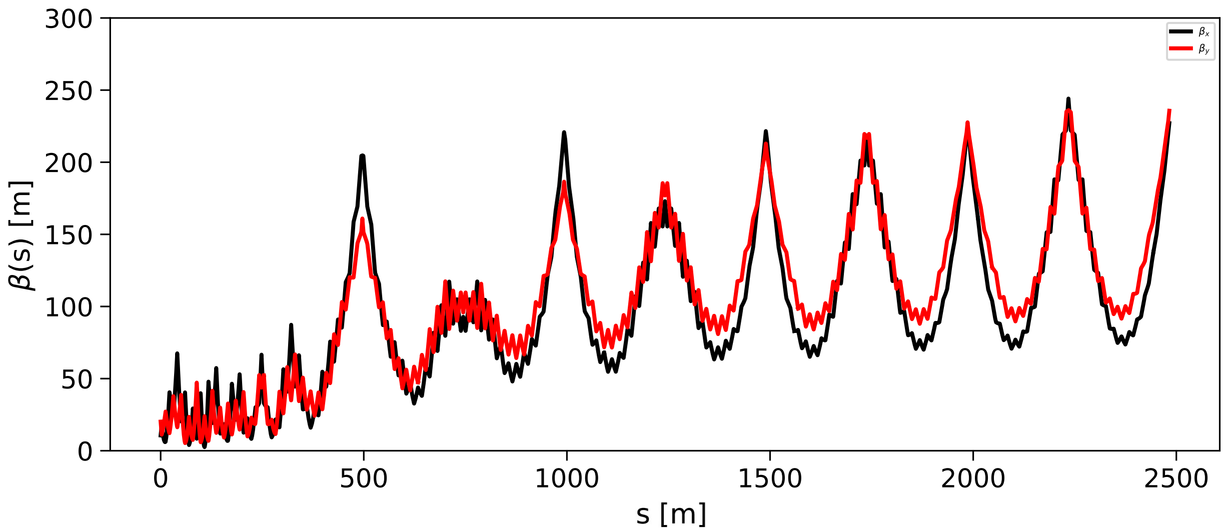

FIG. 20: Optics plot of South linac 10-pass beamline, obtained from a North linac lattice magnet arrangement.

CHAPTER 5

CEBAF ARC RE-DESIGN

The geometry of the CEBAF accelerator during energy recovery requires sharing two accelerating and decelerating beams which converge to the nearly same energy. Electron beams exiting from the North linac travel through the East arc and beams exiting from the South linac travel through the West arc. The corresponding design beam energies for ER@CEBAF, entering into each arc and their converged energies, disregarding synchrotron radiation losses are listed in Table 5. In the vertically stacked CEBAF arcs, the lowest energy

TABLE 5: Corresponding linac passes and desired energy for ER@CEBAF arcs.

East Arcs				West Arcs			
	Linac pass		Energy [MeV]		Linac pass		Energy [MeV]
Arc 1	NL acc01	NL dec05	834	Arc 2	SL acc01	SL dec05	1584
Arc 3	NL acc02	NL dec04	2334	Arc 4	SL acc02	SL dec04	3084
Arc 5	NL acc03	NL dec03	3834	Arc 6	SL acc03	SL dec03	4584
Arc 7	NL acc04	NL dec02	5334	Arc 8	SL acc04	SL dec02	6084
Arc 9	NL acc05	NL dec01	6834	Arc A	SL acc05	SL dec01	7584

arc lies at the top. According to the theory of 'light refraction', where the low-frequency light bends more when traveling through a transparent medium, the beam bend angle depends on the beam momentum

$$\theta = \frac{BL}{B\rho} = BL\left(\frac{q}{p}\right). \tag{66}$$

According to the Eq. (66), for a dipole magnet of length L, with an applied magnetic field B, its bend angle is inversely proportional to beam momentum (p). Here, q is the charge of a single particle.

The arcs are segmented into four regions; the spreader, extraction, proper arc, and recombiner as illustrated in Figure 6. The spreader region is first, splitting the beams into vertically separated bemlines corresponding to their momentum and transporting them toward the horizontal bending 'proper arc'. This occurs with the vertical bending of the electron beam using long dipole magnets and accommodates beam transport through vertically stacked proper arcs. A two-step dogleg layout is used for the spreader and recombiner design, with the purpose of the peak $\beta_y(s)$ minimization [40].

By the design, the spreader and recombiner of each arc are symmetric. A schematic of the dipole magnet layout of West spreaders and recombiners are illustrated in the Figure 21.

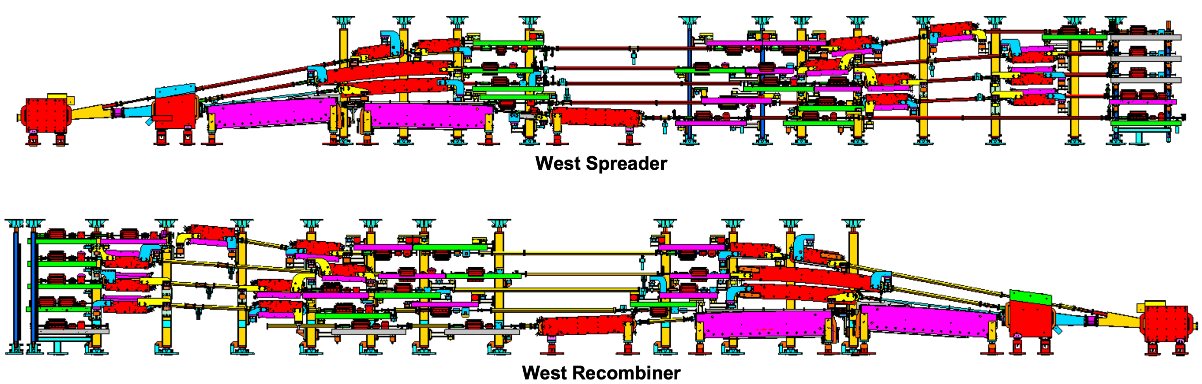

FIG. 21: Schematics of the West arc spreader and recombiner [15].

The extraction region is for Twiss matching into the proper arc. Quadrupole magnets within this region are used for Twiss matching along with ensuring no dispersion leakage from the localized vertically dispersive spreader. Dogleg dipole magnets located here are used for path length corrections during beam operations. Path length is a sensitive parameter to the temperature changes, hence measuring and correcting it is necessary during the beam operations to ensure the proper beam acceleration and transport. Any deviation of path length causes errors in final beam momentum and position, impacting the machine's performance [41].

The proper arc region is where the 180° horizontal bending of the beams occur. These regions consist of horizontally bending dipole magnets with identical topology, 8 sets of quadrupole triplets, and 7 quadrupole singlets. Arcs 1 and 2 consist of only 16 horizontally bending dipole magnets, whereas the remaining eight arcs each consist of 32 dipole magnets. This region is designed to have localized D_x(s), being an achromatic region ensuring no D_x(s) leakage to the downstream beamline. No vertical beam displacement is desinged in this regime, hence need to make sure $D_y(\mathrm{s}) = 0$ throughout the proper arc. Different elevations of the proper arcs are listed in Table 6, assuming linac beamlines lie at $y = 0\,\mathrm{m}$.

TABLE 6: Elevation of CEBAF with respect to the linac heights.

East Arcs	Y orbit [m]	West Arcs
Arc 01	200.0	Arc 02
Arc 03	150.0	Arc 04
Arc 05	100.0	Arc 06
Arc 07	50.0	Arc 08
Arc 09	0.0	Arc A

The horizontally bent beams are then transported towards the next linac. Recombiner segments bend the beams vertically that were previously separated and bring them back together at the next linac entrance, with a proper vertical dispersion closure. The complete arc segments should be achromatic with no dispersion leakage into linac beamlines. Figure 22 illustrates the segmentation of a single arc, with its Twiss output. This figure corresponds to the `OptiM` optics output of Arc 6.

5.1 M_{56} TUNABLE ARCS

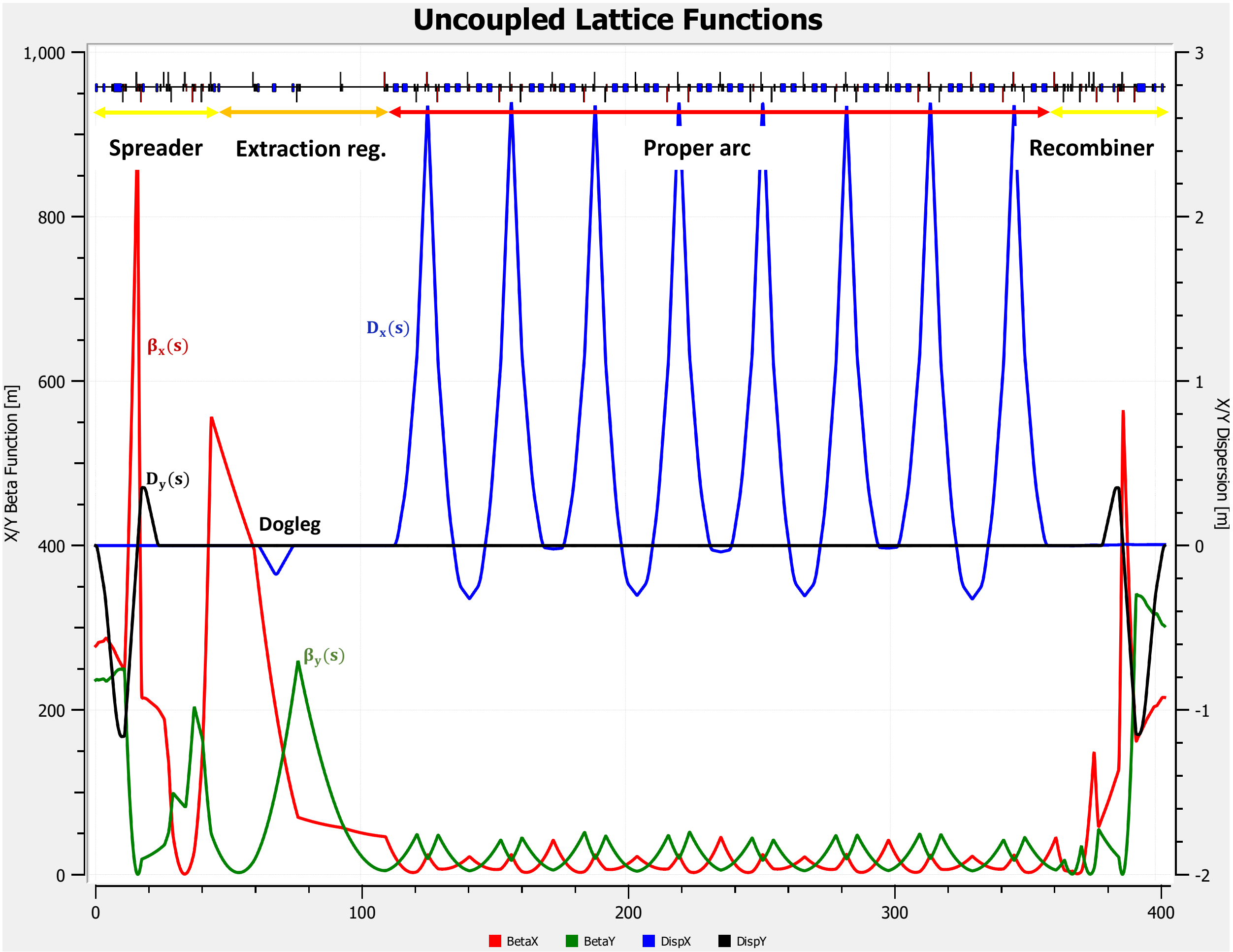

FIG. 22: Segmentation of a CEBAF arc used in the process of tuning M_{56} value of proper arc lattices.

Isochronicity is a property of a lattice in which all particles in the beam have the same time-of-flight, regardless of their initial transverse coordinates and momenta. Isochronous arcs are desired for both CEBAF and ER@CEBAF beamlines since with recirculating arcs, increasing momentum acceptance is required to minimize the beam losses, especially for the decelerating beam. Isochronous lattices are obtained by equating its momentum compaction factor to zero, i.e. $\alpha_c = 0$.

Changing α_c value can be done by varying the M_{56} transfer matrix value through the lattice. This M_{56} value depends on the first-order dispersion $D(s)$ in a lattice over the local bend radius ρ(s):

$$M_{56} = -\int \left(\frac{D(s)}{\rho(s)}\right) ds. \tag{67}$$

Isochronous CEBAF arcs are achieved by counter-balancing M_{56} values between the 180° bending proper arc and the other segments of the arc beamline as shown in Figure 22

$$M_{56(\text{Proper arc})} = -M_{56(\text{Spreader+recombiner+doglegs})}. \tag{68}$$

For the counter-balancing process of M_{56}, the right hand side value of the Eq. (68) is calculated by obtaining transfer matrices for each segment, and the required M_{56} value for the proper arc is calculated. Then the proper arc is segmented in to four cells, where each cell consists of two quadrupole triplets and two quadrupole singlets. The last cell is truncated at the second quadrupole singlet. Figure 23 illustrates the magnet layout of a single cell [42]. Adjustment of α_c follows the procedure describes below.

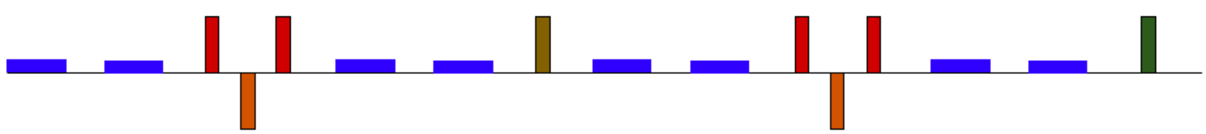

FIG. 23: Schematic of a single cell proper arc magnet layout: triplets and singlet sets are identical. Segmentation of a CEBAF arc used in the process of tuning M_{56} value of proper arc lattices. The dipole magnets are denoted with the blue rectangles and the color-coded vertically aligned blocks represent quadrupoles magnets with different focusing strengths. Two triplet quadrupoles are identical for each cell.

First, the boundary quadrupoles of triplets are used to achieve achromat cells with $D_x(s)$ = $D_y(s)$ = 0 m at the ends of the cell. Then the field gradients of all the quadrupoles are adjusted until the desired α_c value is obtained. The latter step assumed the cell to be a periodic lattice:

$$\alpha_c = \frac{M_{56}}{s}. \tag{69}$$

Here s is the path length of the cell.

Eq. (69) is used to calculate the required M_{56} value at a single cell. The resulting quadrupole field gradient values are used to build up the four-cell structure of the proper arc lattice for all the ten CEBAF arcs. Spreader, extraction region and recombiner segments are added according to the arc lattice structure along with Twiss matching using the spreader and recombiner quadrupoles, for the build-up of the complete arc beamline. Quadrupoles located the non-zero vertical dispersion regime, namely S01, S02, S03, R08, R09 and R10 are kept as they are, so D_y(s) is unchanged [43].

5.2 LATTICE MODIFICATIONS

To achieve low-dispersion, isochronous arcs, the existing CEBAF arc lattice optics have been redesigned. For ER@CEBAF however, the incorporation of an additional segment, namely a pathlength chicane, is necessary before proceeding with the construction of the isochronous arc at Arc A.

5.2.1 THE PATH LENGTH CHICANE

The path length chicane for ER@CEBAF will be installed in Arc A, and needs to provide an additional path length of half of the CEBAF RF-wavelength of 10.0 cm. In the ER@CEBAF proposal, the suggested chicane design uses CEBAF MBA 3-meter 40-turn dipole magnets with a 4.96° bend angle. Eventually, the evaluations performed by the Jefferson Lab's magnet group suggested that the proposed dipole magnets were not up to standards for reusability.

A second chicane design was then proposed which uses 2.0 m steel-length dipole magnets. Four identical magnets with 4.955° bend angle are aligned into a chicane with two dogleg segments. The maximum beam energy considered here is 7.584 GeV, the beam energy exiting from the South linac. For this electron beam energy value, the maximum required magnetic field for the chicane dipole magnets is 1.9 T.

Figure 24 illustrates the magnet layout of the proposed chicane design, with its two symmetric dogleg structure. The total length of the chicane is 32 m, with a total path length of 32.10 m. Path length calculation consists of contributions from the geometric length and

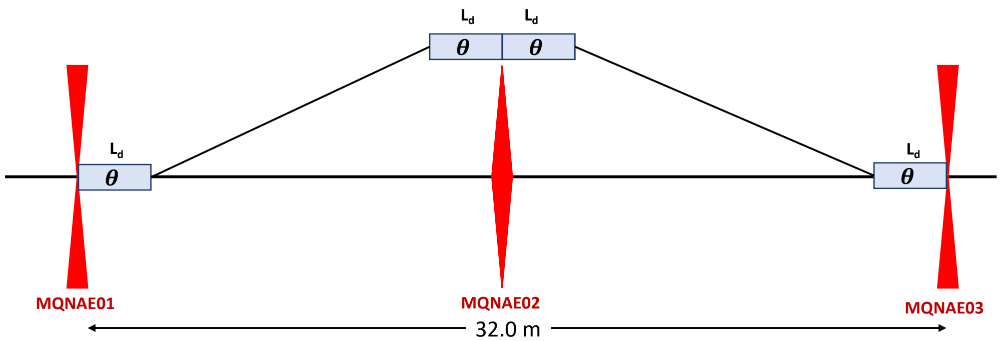

FIG. 24: Magnet layout of the proposed pathlength chicane, bypassing the existing E02 quadrupole magnet (reproduced from [22]).

dipole arc length components

$$\text{Geometric path length} = 2\left(\frac{L_{chicane} - 4L_d}{2}\right)\frac{1}{\cos\theta} + 4L_d = 32.089\,85\,\mathrm{m}, \tag{70}$$

$$\text{Dipole arc length} = 4L_d\left(\frac{\theta}{\sin\theta}\right) = 8.009\,96\,\mathrm{m}. \tag{71}$$

Here, L_d is the dipole steel length, and θ is the bend angle of a dipole magnet. The most significant contribution to this difference in path length arises from the drift sections located between the first and second dipoles, as well as between the third and fourth dipoles.

The path length difference due to the chicane is

$$\Delta s = (32.0902\,\mathrm{m} - 32.0\,\mathrm{m}) + (8.0998\,\mathrm{m} - 8.0\,\mathrm{m}) = 0.1002\,\mathrm{m} = 10.0\,\mathrm{cm}. \tag{72}$$

The proposed installation site for the chicane is the extraction region of arc A, bypassing the E02 quadrupole magnet. The installation of the chicane dipoles within the CEBAF beamline will not have any adverse effects on the regular CEBAF operations at 12 GeV, as the chicane will be turned off in those conditions.

Figure 25 provides a visual representation of the chicane's placement in the beamline, illustrating its path as it bypasses the E02 quadrupole magnets in Arc A. This configuration enables the desired functionality of the chicane while ensuring compatibility with existing CEBAF operations [22].

When determining the dipole bend angle and chicane length, several factors needed to be considered. Firstly, it was important to ensure that the chicane could be accommodated within the existing tunnel area without causing any interference with the clearances in the installation site. The dimensions of the chicane had to be carefully chosen to avoid any physical obstructions or constraints. With the parameters used in the designed chicane two dipoles at the middle extend approximately 1.2 m to the isle of the tunnel. This consideration was crucial for maintaining sufficient space for equipment installation, accessibility, and safety within the facility.

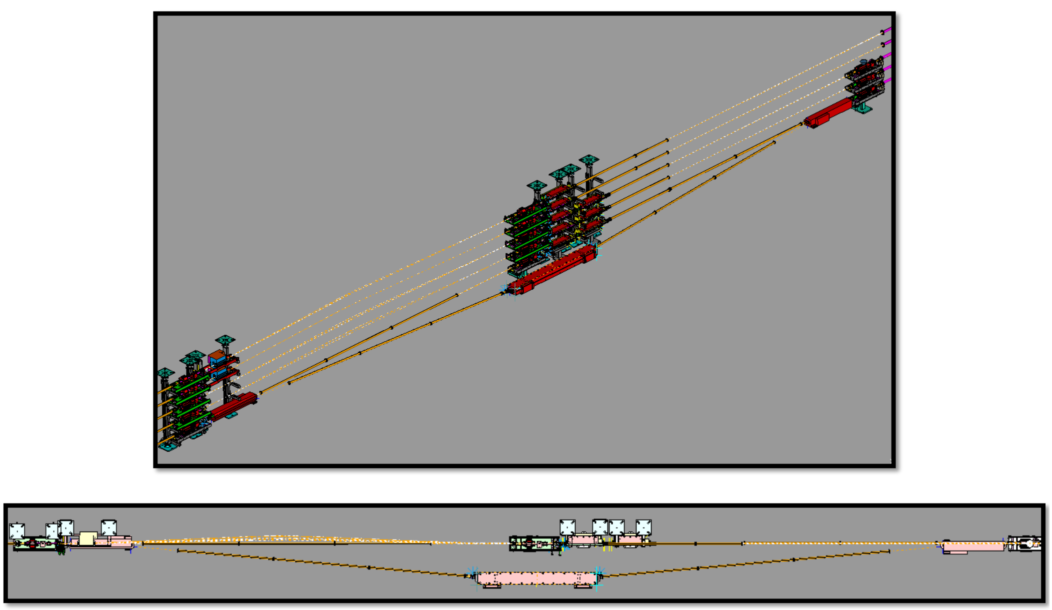

FIG. 25: Overview of the chicane placement in the beamline, bypassing the arc A extraction region (reproduced images from Kelly Tremblay [22]).

By carefully accounting for these factors, it was possible to determine the optimal dipole bend angle and chicane length that would satisfy the installation requirements, fit within the available space, and allow for efficient and effective operation of the CEBAF accelerator.

In order to facilitate both the "straight through" and "chicane bypass" modes, the implementation of a specialized beam pipe design with a 5° split is necessary. A vacuum chamber featuring a similar geometry has already been utilized in the CEBAF transportation system, as seen in the Hall A Compton polarimeter chicane [44]. Therefore, there are no additional vacuum-related concerns associated with the installation of the path-length chicane. The existing experience and success with the vacuum chamber design in similar setups provide assurance that the new chicane installation can be accomplished without significant complications regarding vacuum requirements.

5.2.2 ARC A RECOMBINER

In the current beamline design of CEBAF at 12 GeV, Arc A is responsible for transporting the highest-energy electron beam towards the North linac. However, there is an observed dispersion leak of approximately 3 mm at the end of the recombiner in Arc A.

Although the small dispersion leakage can be managed using operational techniques at present, the situation may become more challenging with the introduction of additional five passes through the machine. Even with a smaller dispersion leak, the increased number of passes in ER@CEBAF can result in significant optics distortion in the downstream beamline.

Addressing this issue and minimizing the impact of the dispersion leak is crucial in maintaining the desired beam quality and performance in the downstream beamline. Achieving dispersion closure with the existing magnet layout in Arc A poses a significant challenge. Additionally, while the spreader and recombiner segments in other arcs are symmetric to each other, this symmetry is not present in Arc A. Therefore we proposed a solution that involves introducing quadrupole magnets into both spreader and recombiner segments. One additional quadrupole magnet of length 15 cm is introduced into the spreader region as illustrated in Figure 26.

Two additional quadrupole magnets of length 15 cm are added in between the R01 and R02 dipoles and R05 and R06 dipoles as illustrated in Figure 27. The use of quadrupoles is necessary since the closure of both D_y(s) and $D'_y(s)$ is required. By incorporating these additional quadrupole magnets, proper dispersion closure can be achieved in Arc A, while making spreader and recombiner chicanes symmetric as in the rest of the CEBAF arcs.

The current M_{56} and α_c values of the re-designed arcs are listed in the Table 7.

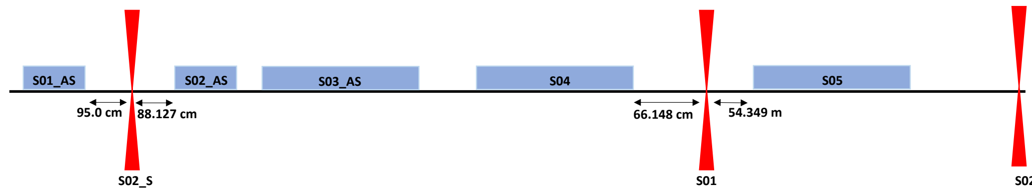

FIG. 26: Magnet layout of the Arc A spreader, with added quadrupole magnet S02_S, marked with corresponding distances from the adjacent dipole magnets.

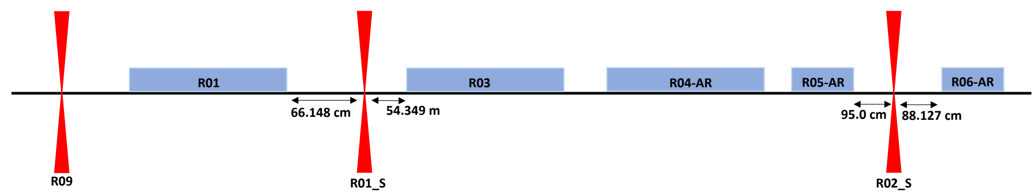

FIG. 27: Magnet layout of the Arc A recombiner, with added quadrupole magnets R01_S and R02_S, marked with corresponding distances from the adjacent dipole magnets.

Optics plots of the re-designed arcs to be matched with the special linac beamlines are shown in Figures 28, 29 and 30. All the ten arcs show four-fold symmetry in optics variation within the proper arc as expected. The peak β(s) values are observed in the horizontal plane, at the vertical bend regions; spreaders and recombiners. Arcs 6,7 and 8 show excessively large β_x(s) peaks and these peak heights solely depend on the boundary Twiss values of the arcs, which were pre-determined from the optimized ten-pass linac beamline.

Since these β_x(s) peaks lie within the regions of the vertical bends, the minimization of these peaks is cumbersome. An analysis was carried out on how effective the peak $\beta(s)$ reduction in the spreader, is compared to the initial $\beta_x(s)$ value. The Arc 6 lattice is used in this analysis. The first analysis was performed by changing the initial $\alpha_x(s)$ value of Arc 6. Table 8 contains the data of the analysis of the dependence of the peak $\beta_x(s)$ reduction with respect to the change in $\alpha_x(s)$ value. It is observed that a change of the $\alpha_x(s)$ value does

TABLE 7: Calculated M_{56} and momentum compaction(α_c) values of re-tuned arcs.

Arc	M_{56} [cm]	Momentum compaction (α_c)
Arc 01	1.792 $\times 10^{-02}$	-6.339 $\times 10^{-08}$
Arc 02	2.717 $\times 10^{-01}$	-6.615 $\times 10^{-06}$
Arc 03	1.366 $\times 10^{-03}$	-1.447 $\times 10^{-08}$
Arc 04	-1.834 $\times 10^{-03}$	7.288 $\times 10^{-08}$
Arc 05	8.955 $\times 10^{-04}$	-4.172 $\times 10^{-09}$
Arc 06	2.075 $\times 10^{-05}$	1.144 $\times 10^{-08}$
Arc 07	1.215 $\times 10^{-06}$	6.277 $\times 10^{-09}$
Arc 08	-2.135 $\times 10^{-02}$	5.359 $\times 10^{-07}$
Arc 09	4.28 $\times 10^{-02}$	-1.050 $\times 10^{-06}$
Arc A	-2.4890 $\times 10^{-03}$	-5.685 $\times 10^{-08}$

not affect much for the peak $\beta_x(s)$ value, but this depends on the initial value of the $\beta_x(s)$ of the corresponding arc. Changing $\beta_x(s)$ is not feasible as then it affects the optimized linac

TABLE 8: Peak $\beta_x(s)$ reduction with respect to the initial $\alpha_x(s)$ value.

$\alpha_x(s)$	$\Delta\alpha_x(s)$	Peak $\beta_x(s)$ [cm]	% $\beta_x(s)$ reduction
-0.97895	0	97706.06	0.0
-0.87895	-0.1	96719.1	-1.010
-0.78795	-0.2	95736.6	-2.015
-0.68795	-0.3	94759.2	-3.016
-0.68795	-0.4	93786.8	-4.011

optics. Therefore, a particle tracking study was performed on each lattice to determine the maximum beam size through each arc.

Before proceeding towards the building up of the ten-pass beamline, the arc lattices obtained in `OptiM` format were translated in `Elegant` input files. `OptiM` is a linear lattice design program with limited features, hence a non-linear particle tracking program was needed for further analysis with particle tracking. The translated arc lattices were re-matched at spreaders and recombiners since the translation from `Optim` to `Elegant` is not a 100% perfect match.

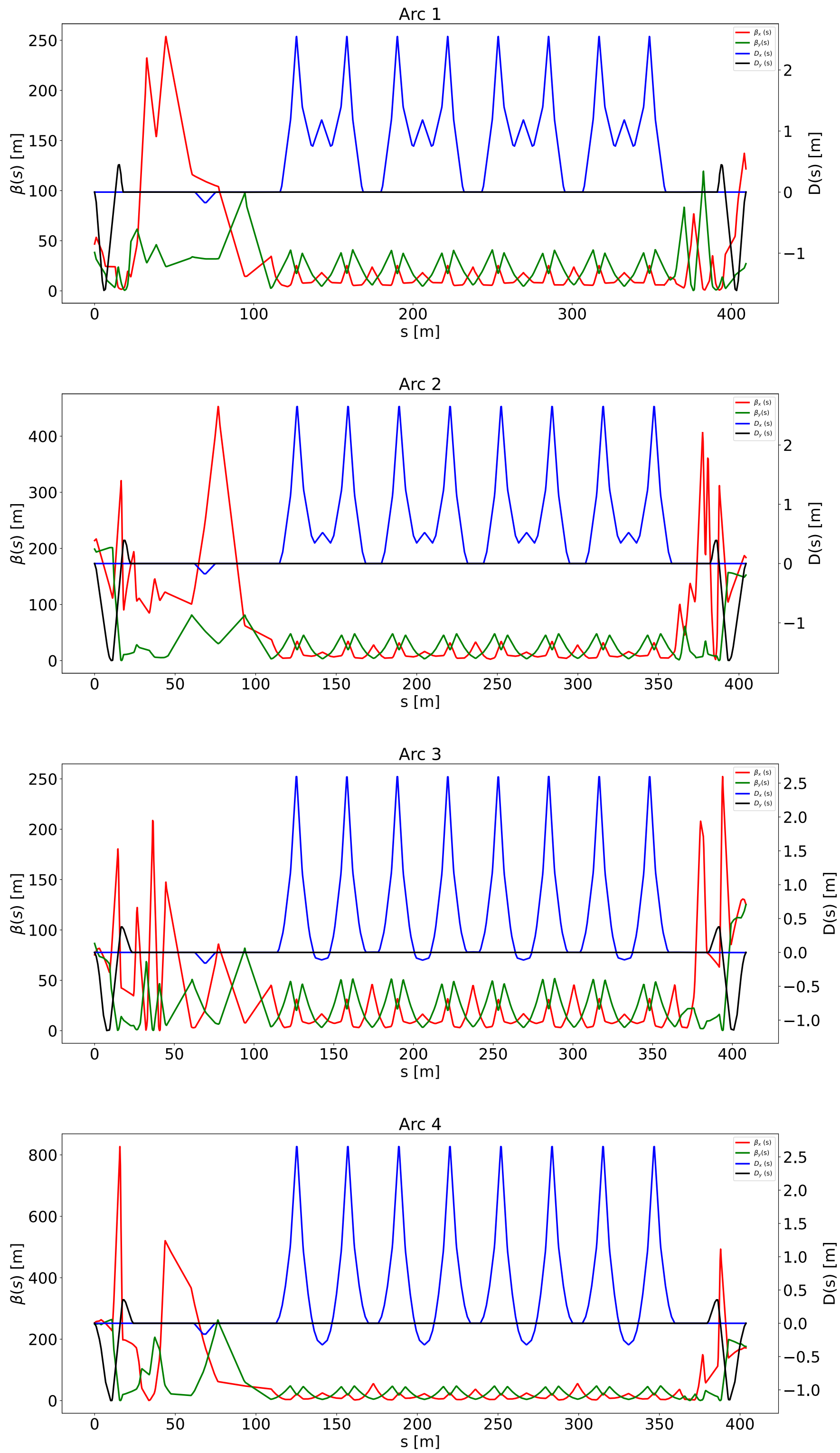

FIG. 28: Optics plots of the Arcs 1 to 4 of the redesigned arcs for ER@CEBAF.

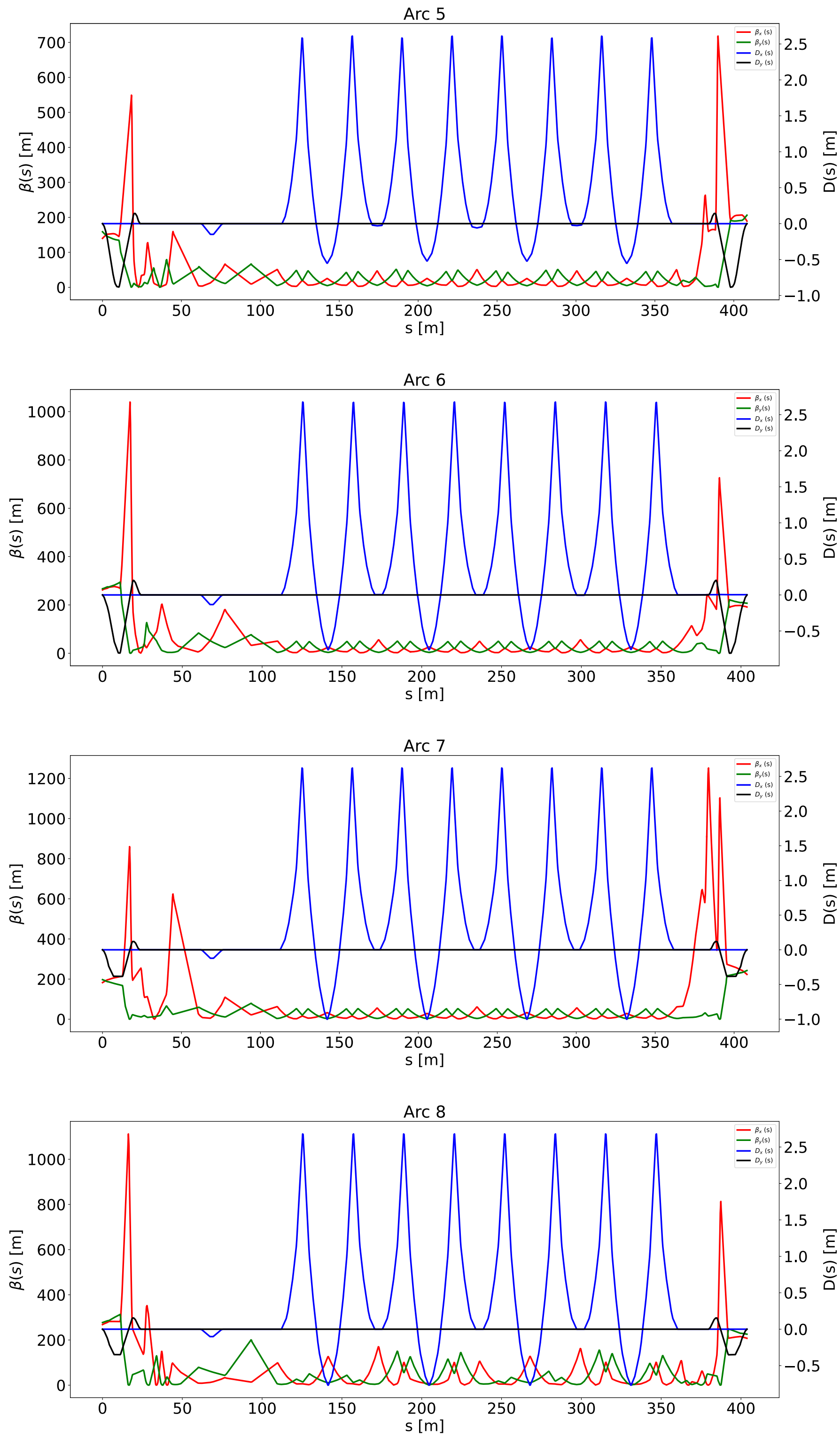

FIG. 29: Optics plots of the Arcs 5 to 8 of the redesigned arcs for ER@CEBAF.

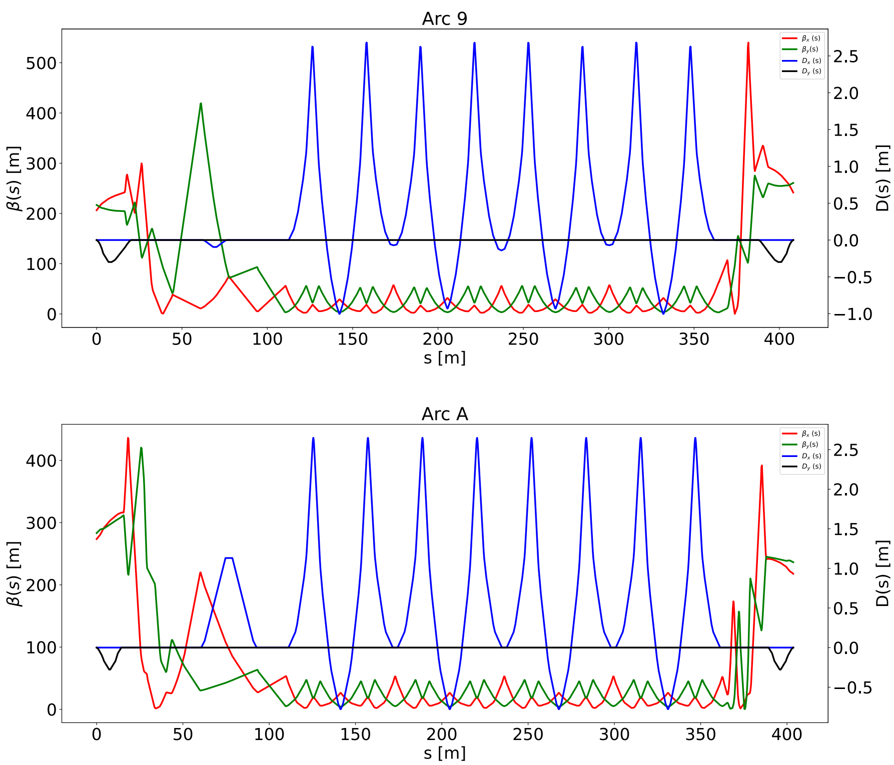

FIG. 30: Optics plots of the Arcs 9 and A of the redesigned arcs for ER@CEBAF.

CHAPTER 6

START TO END TRACKING IN ER@CEBAF BEAMLINE

The ER@CEBAF beamline comprises a total of ten passes, consisting of five accelerating passes followed by five decelerating passes, leading up to a low-energy beam dump. By utilizing the lattice segments derived and optimized in the preceding chapters, the beamline can be effectively constructed, ensuring precise control and manipulation of the beam throughout its multiple passes. The `Elegant` [39] particle tracking code is used for the ten-pass beamline construction and optics studies with tracking analysis. The `OptiM` arc lattice files are converted into `Elegant` input file format using a Python script.

6.1 ER@CEBAF BEAMLINE OPTICS

The energy of the beam exiting from the injector complex towards the north linac is 84 MeV. The North linac and South linac beamline element specifications have been derived through the process of optics optimization, as detailed in chapter 4. Twiss function values at the entrance and exit of the linacs are used for Twiss matching of the corresponding arcs. The optics of the ten CEBAF arcs were redesigned using the tunable M_{56} methodology implemented as described in chapter 5, and are designed to be isochronous and achromatic. The 10-pass beamline is built by adding corresponding linac and arc lattice segments accordingly.

6.1.1 ACCELERATING BEAMLINE

The accelerating beamline of ER@CEBAF commences at the beginning of the North linac, immediately following the injector chicane. The injector beam parameters are assumed here. The accelerating beamline extends up through the fifth pass through the South linac, with scaled linac energy gains of 750 MeV. The peak beam energy is 7.5 GeV at the end of this tenth linac pass. The beamline follows the CEBAF beam transportation scheme and an optics plot of the accelerated beamline is given in Figure 31.

The $\beta_x(s)$ peaks observed in the top plot of Figure 31 correspond to the regions with vertical bends: arc spreaders, and recombiners. As observed with the individual arc optics plots, peak $\beta_x(s)$ of ≈ 1200 m is at the Arc 7 recombiner. The bottom plot illustrates the dispersion variation along the accelerating beamline. Lower energy arcs show large vertical

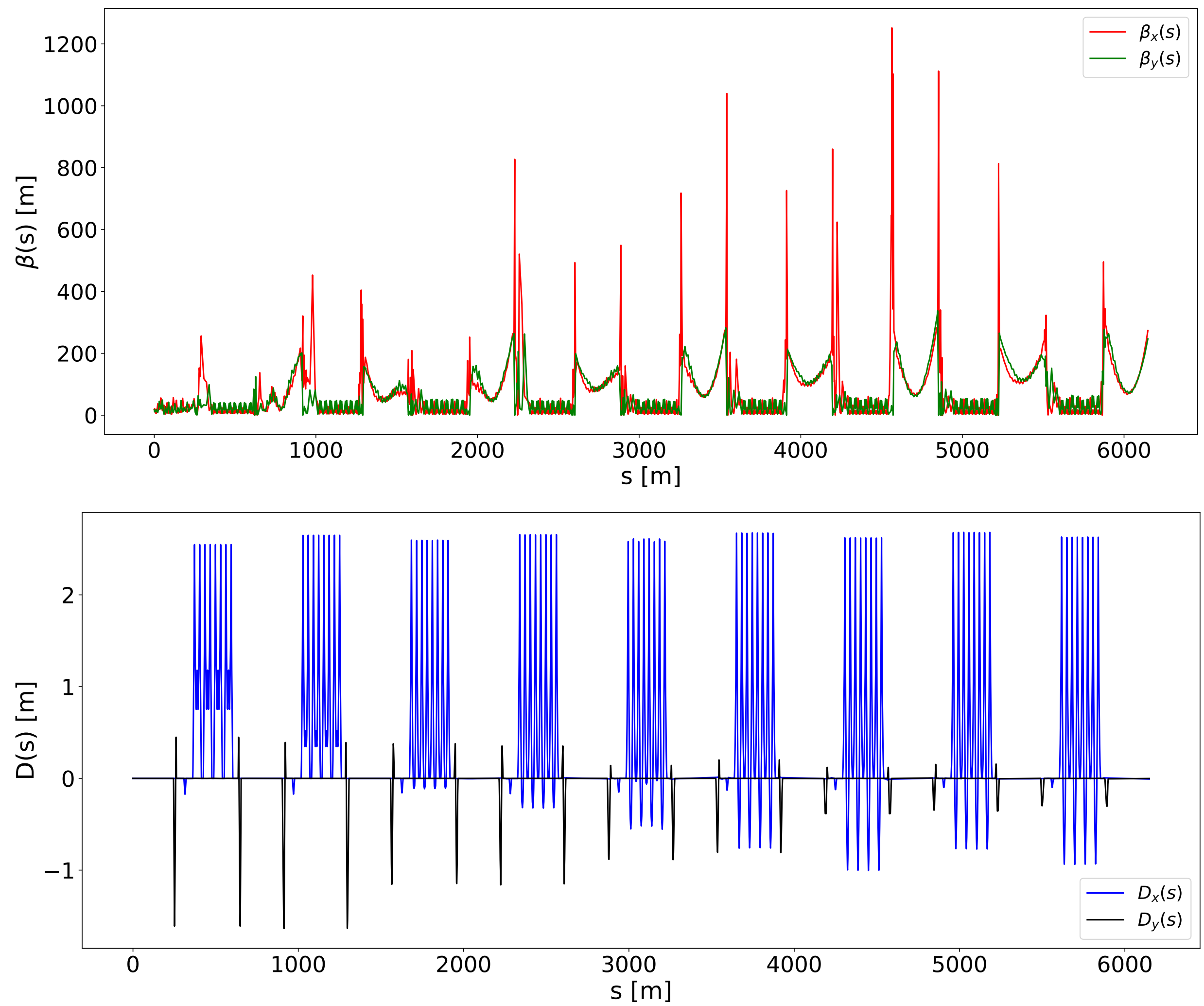

FIG. 31: Twiss function variation along the five Accelerating passes. $\beta(s)$ variation in the top plot, and D(s) variation illustrated in the bottom plot.

dispersion ($D_y(s)$) as they are the arcs with larger vertical elevations. Corresponding arcs with the same elevations in East and West arc segments exhibit similar $D_y(s)$ variations. The peak horizontal dispersion ($D_x(s)$) values for all the arcs $\approx 2.5\,\mathrm{m}$, where the high energy arcs tend to have negative $D_x(s)$ as result of making their M_{56} values zero. The counterbalancing of horizontal and vertical dispersions is clearly visible in this beamline.

6.1.2 DECELERATING BEAMLINE

The path length chicane provides an additional path length of 10 cm to the beam when the beam passes through Arc A. In this context, the energy recovery beamline initiates at Arc A, followed by five more passes through the machine. Initial conditions for the decelerating beamline come from the optimized linac lattice of South linac, the end Twiss of the fifth accelerating pass there.

The decelerating beamline is of 6500 m total length. The designed energy at the end of the tenth pass through the South linac is 84 MeV neglecting synchrotron radiation losses, serving near 100% energy recovery during deceleration.

The plot of Twiss functions variation for the decelerating beamline is illustrated in Figure 32. The designed Twiss functions show a mirrored variation as observed in the accelerating beamline, with no significant dispersion leakage. The radiation losses are unaccounted in the lattice Twiss calculation.

6.2 PARTICLE TRACKING ANALYSIS

The optics design of a lattice involves matching of the beam Twiss values to the lattice values. The values of the designed lattice Twiss functions are obtained from the `Elegant` particle tracking program.

The Twiss calculation for the beam requires transportation of macro particles through the designed beamline. The beam parameters used in the particle tracking analysis are listed in the Table 3. An initial bunch length of 0.1 mm and fractional momentum spread of 2×10^{-5} are used as they satisfy the conditions listed in Table 3.

Initial tracking analysis was performed using 1024 particles. Table 9 contains the beam energy values at each arc during accelerating and decelerating passes through the ER@CEBAF lattice. The observed energy losses are due to synchrotron radiation emission at the bend magnets. The beam loses a total energy of approximately 25 MeV through the ten passes. The beam energy at the exit of South linac, after energy recovery is found to be 60.12 MeV.

The beam and lattice energy profiles along the beamline are plotted in Figure 33. Both the model and the beam energy variation follow a similar trend. The highest beam energy is recorded at the end of the fifth acceleration. The end of the accelerating beamline is marked with the vertical dashed line near $s = 6147$ m. No significant energy difference is visible in the Figure 33, as the recorded total energy difference of 24.665 MeV is insignificant compared to the maximum design energy of 7584 MeV. However, the energy difference between the design and the beam at the last deceleration linac pass is significant as now the percentage

TABLE 9: Detailed energy description of beam energies at Arcs, at each pass. Energy loss at each arc and the cumulative losses are calculated.

Arc (Accelerating)	$E_{entrance}$ [MeV]	E_{exit} [MeV]	ΔE [MeV]	cumulative ΔE [MeV]
Arc 1	834.79	834.78	0.010	0.010
Arc 2	1584.78	1584.73	0.047	0.057
Arc 3	2334.73	2334.55	0.181	0.238
Arc 4	3084.54	3084.25	0.295	0.533
Arc 5	3834.25	3833.60	0.647	1.180
Arc 6	4583.60	4582.38	1.222	2.402
Arc 7	5332.37	5330.90	1.475	3.876
Arc 8	6080.90	6078.48	2.421	6.298
Arc 9	6828.47	6824.91	3.561	9.859
Arc A	7574.91	7569.85	5.063	14.922
Arc (Decelerating)	$E_{entrance}$ [MeV]	E_{exit} [MeV]	ΔE [MeV]	cumulative ΔE [MeV]
Arc 9	6819.85	6816.30	3.546	18.467
Arc 8	6066.30	6063.91	2.398	20.866
Arc 7	5313.91	5312.45	1.455	22.320
Arc 6	4562.46	4561.26	1.200	23.520
Arc 5	3811.26	3810.63	0.632	24.152
Arc 4	3060.63	3060.34	0.286	24.438
Arc 3	2310.35	2310.17	0.173	24.611
Arc 2	1560.17	1560.13	0.044	24.656
Arc 1	810.13	810.12	0.009	24.665

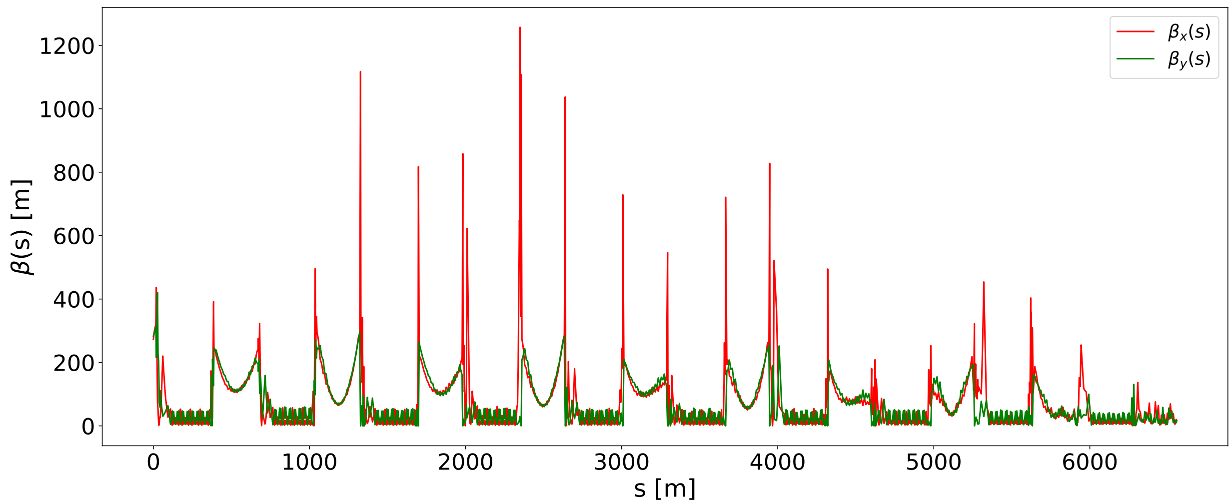

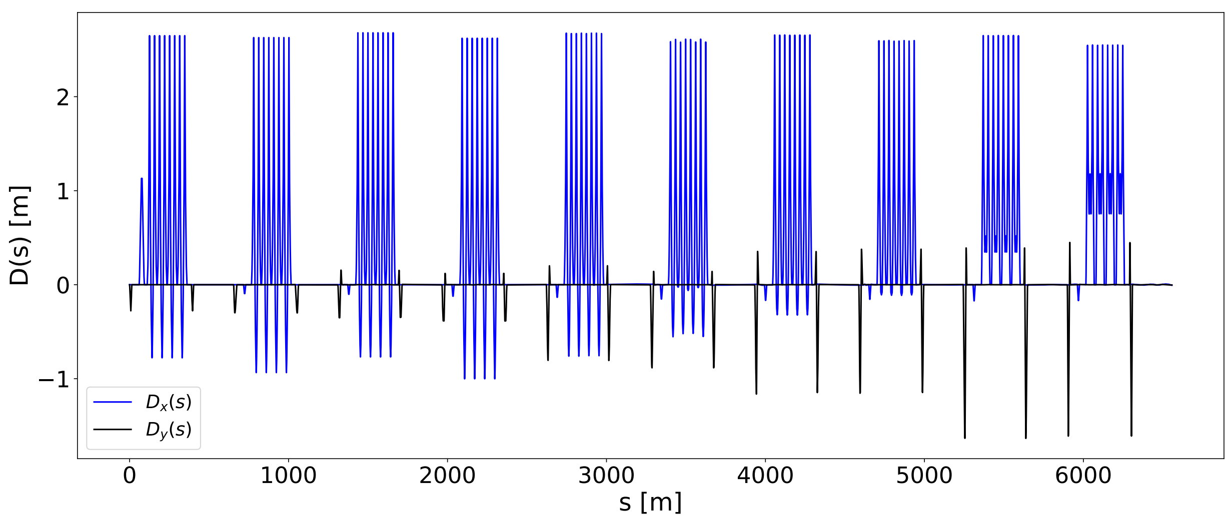

FIG. 32: Twiss function variation along the five Decelerating passes. $\beta(s)$ variation in the top plot, and $D(s)$ variation illustrated in the bottom plot.

energy mismatch is 28.1%.

The comparison of the beam Twiss functions with the lattice functions is carried out using a beam consists with 100,000 particles. The comparison plots of $\beta(s)$ functions in horizontal and vertical planes are illustrated in Figure 34. The top plot illustrates the horizontal $\beta(s)$ variation of the model lattice and the beam. Both curves exhibit a closer agreement between the beam and lattice values. The bottom plot displays the $\beta(s)$ variation of the beam and the model lattice. For both comparison plots, the same vertical scale is used, highlighting the

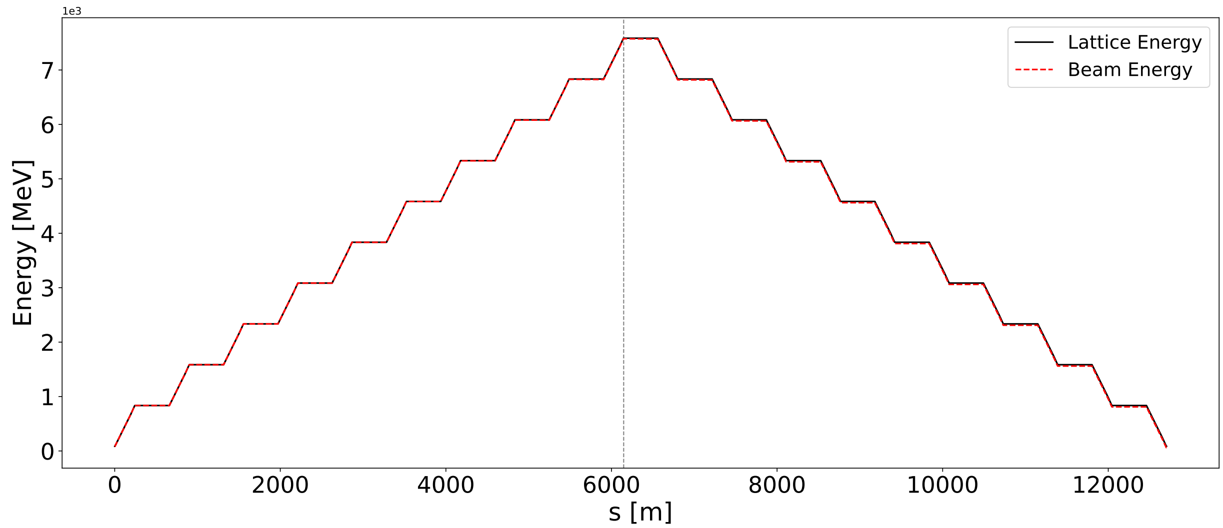

FIG. 33: The energy profiles of the beam and lattice, through the 10-pass beamline, Design lattice energy is shown in the black curve, and the beam energy is denoted by the red-dashed curve.

noticeably smaller $\beta_y(s)$ values when compared to $\beta_x(s)$. Additionally, it is evident that the peaks in both planes are situated in regions corresponding to arc spreaders and recombiners. The beam $\beta_x(s)$ values are slightly larger at each peak compared to the corresponding lattice value.

In arcs 1 to 8, each spreader and recombiner segment are equipped with three quadrupole magnets, for the purpose of proper closure of the $D_y(s)$ function. The first quadrupole magnet defocuses the beam in the horizontal plane which leads to an increase in the $\alpha_x(s)$ values in that region, consequently resulting in the peak β_x values. As described in the Chapter 5, these peak values depend on the initial Twiss at each arc.

Similarly, for the $\alpha(s)$ variation, the gradients of the $\beta(s)$ function at each element are extracted from an `Elegant` output files. The Twiss output file contains the lattice parameters and Sigma output file contains the beam parameters. Comparison plots for both horizontal and vertical planes are provided in Figure 35. The upper plot illustrates the $\alpha_x(s)$ variation in the horizontal plane, where the $\alpha_x(s)$ values are much higher up to 400. Larger $\alpha(s)$ implies a sudden change in the shape and orientation of the beam ellipse, which necessitates meticulous control of the beam transportation. These large values can also introduce noise

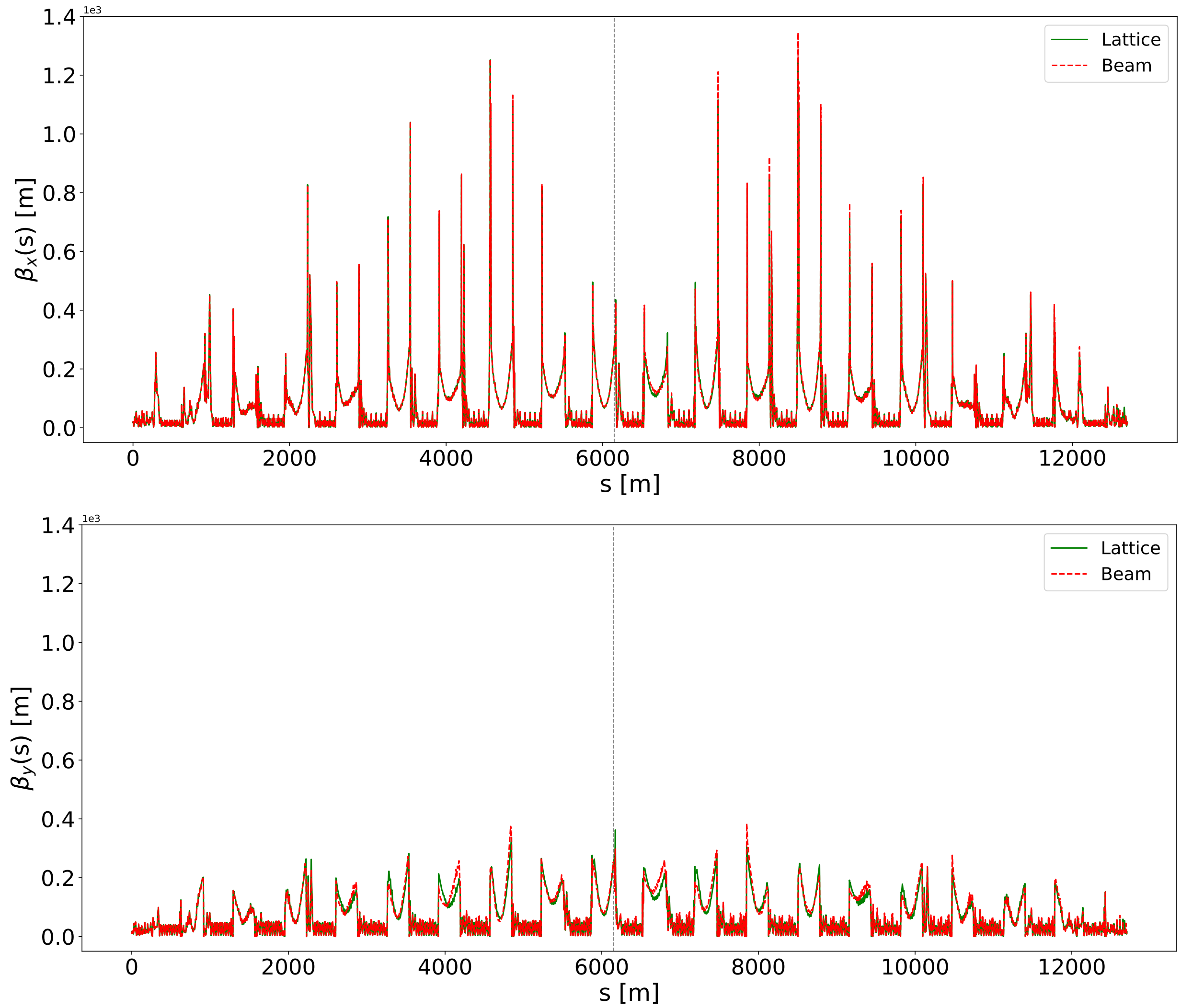

FIG. 34: The $\beta(s)$ functions of the beam and model plotted together for horizontal (top) and vertical (bottom) planes. Model values are presented with green curves and beam values are illustrated in the red-dashed lined.

errors in the tracking simulations as well. Comparatively, the $\alpha_y(s)$ are much smaller. Both planes exhibit proper agreements between the model lattice and the beam values.

The $\alpha(s)$ values depend on the $\beta(s)$ variation, and the $\alpha(s)$ peaks are observed at the locations where the $\beta(s)$ peaks are observed. It was observed that without proper modeling of beamline elements to suppress the statistical errors in the calculation of beam parameters,

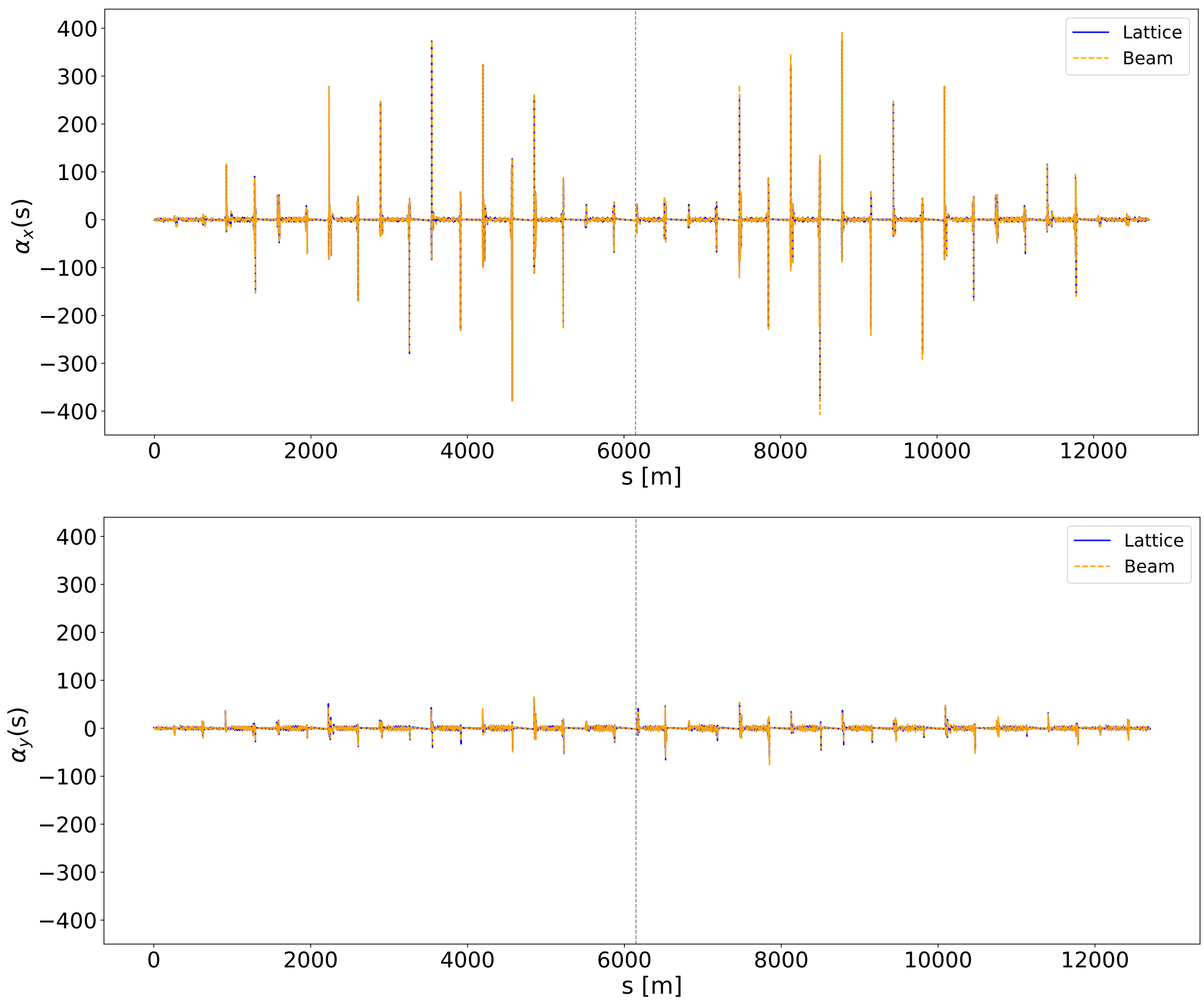

FIG. 35: The $\alpha(s) \equiv -1/2(d\beta/ds)$ functions of the beam and model plotted together for horizontal (top) and vertical (bottom) planes. Model values are presented with blue curves and beam values are illustrated in the orange-dashed lined.

significant mismatches between the beam and lattice Twiss values are observed. With proper element modeling and beam control strategies, smooth beam transportation is possible in this situation. An analysis performed on the dipole and quadrupole model parameter is described in Appendix A.

The horizontal and vertical beam sizes are compared in Figure 36. The initial beam distribution used in this tracking analysis is a Gaussian beam distribution symmetric in x -

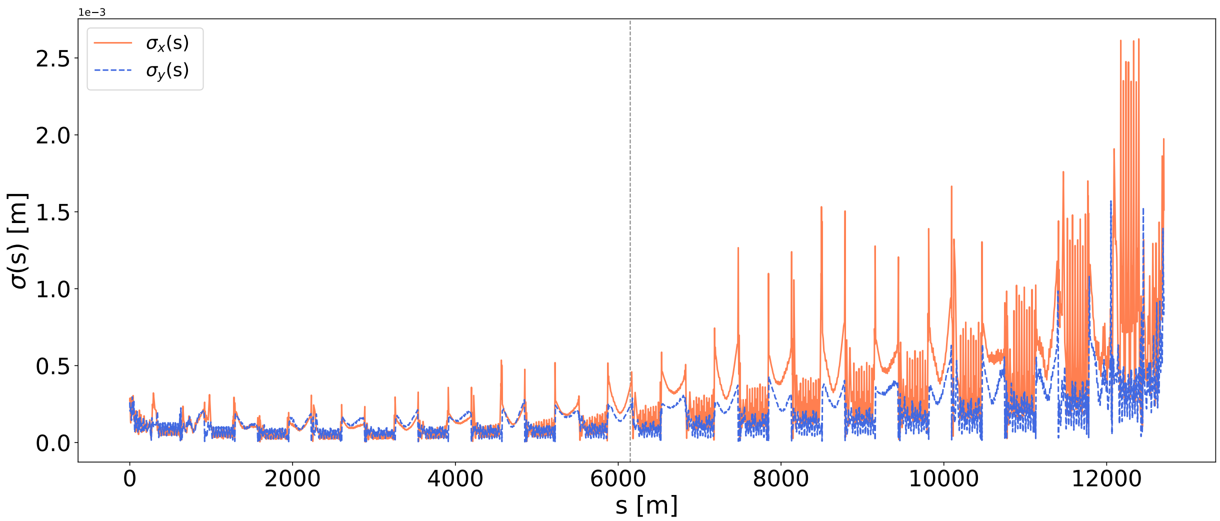

FIG. 36: The beam size evolution in the x and y planes are plotted. The orange curve illustrates the horizontal beam size and the blue curve represents the beam size in vertical plane.

y space.

In the accelerating beamline, both horizontal and vertical beam sizes evolve with similar magnitudes. But within the energy recovery passes, horizontal beam size ($\sigma_x(s)$) become much larger compared to the vertical beam size ($\sigma_y(s)$). The maximum beam size recorded is approximately 2.5 mm, compared to the beam pipe aperture, which is approximately 2 cm.

In the presence of acceleration, the behavior of transverse beam focusing deviates from that observed under constant energy conditions, as detailed in Chapter 2. The longitudinal momentum increases as acceleration occurs, while transverse momenta remain same. The equations of motion in transverse plane now are under the influence of both transverse magnetic fields and accelerating electric fields. Hence the area of the phase space ellipse and the geometric emittance decrease due to acceleration. This phenomenon is known as 'adiabatic damping' and the geometric beam emittance (ϵ) scales with the energy as

$$\epsilon \approx \frac{1}{E}. \tag{73}$$

Despite its name implying "adiabatic damping," it's important to note that this process is not a true damping mechanism. The decrease in geometric emittance during acceleration is applicable to all three degrees of freedom. Given that the quantity ϵ varies scaled with momentum, a new parameter known as 'normalized emittance' denoted as $\epsilon_n = \beta\gamma\epsilon$, has been introduced to make this scaling explicit. This normalized emittance is invariant even in beam transport with energy changes [1].

The reduction in geometric transverse emittance during the beam acceleration provides a clear explanation for the smaller beam sizes observed in within accelerating beamline. Conversely, during deceleration, the transverse emittance experiences an anti-damping effect as the beam loses energy. This leads to an increase of beam sizes in both x and y planes as observed in Figure 36.

However, it is also essential to note that the normalized emittance can undergo changes in the presence of radiation losses, beam scattering or damping. In such cases, Liouville's theorem, which hinges on the conservation of phase space, no longer applies and the normalized emittance also changes when these dissipating effects come into play. In the specific case of the ten-pass beamline under consideration here, the beam does not experience radiation losses in the straight linacs. As a result, we can clearly observe the adiabatic damping and anti-damping contributions from acceleration and deceleration in the linacs and synchrotron radiation in the arcs.

To provide a visual representation, Figure 37 displays both the geometric and normalized emittance evolution along the same beamline. To enhance clarity, the emittance values on the vertical scales are presented in a logarithmic scale. In the top plot of the figure, one can clearly observe the described patterns of reduction and increase in $\epsilon(s)$. The corresponding variation in $\epsilon_n(s)$, as shown in the bottom plot, aligns with the adiabatic damping and anti-damping characteristics described previously.

The $\epsilon_n(s)$ values remains constant within linacs, in both x and y planes. However, within the arcs, the horizontal normalized emittance experiences an increase due to the presence of horizontal dispersion, and radiation losses due to horizontal bends at the proper-arc sections. Additionally, the vertical normalized emittance undergoes changes, showing slight increments in regions corresponding to spreaders and recombiners, where non-zero vertical dispersion is present along with radiation losses.

The beam sizes depend on the Twiss parameters, dispersion functions and fractional momentum spread as described in Eq. (48). The dispersion functions are controlled to be localized, suppressing both the $D(s)$ and $D'(s)$ at each arc. Hence the effect on beam sizes from the dispersion function should be same for accelerating and decelerating passes. But the relative momentum spread of the beam increases during the energy recovery as the beam

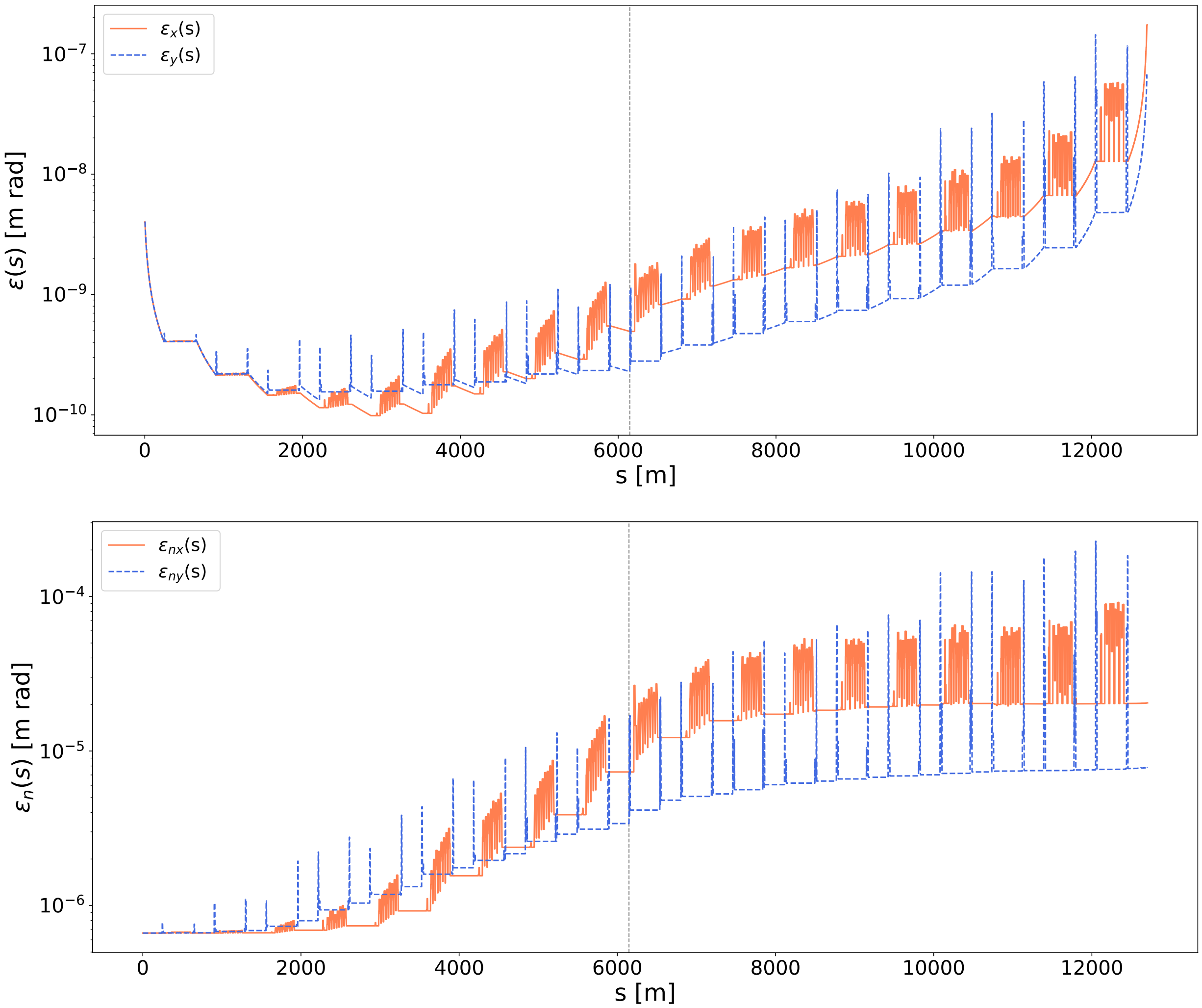

FIG. 37: The comparison of the beam emittances is x and y planes. Top plot illustrates geometric beam emittances and the bottom plot illustrates the normalized beam emittances.

loses its energy. According to the beam size equation, the product of the $D(s)$ and $\delta(s)$ linearly depend on the beam size. The plot in Figure 36 clearly emphasizes the beam size increase within the proper arc segments of the arcs. The horizontal dispersion is non-zero at the proper arc regions, and this observation clearly states the increase of the horizontal beam size in the energy recovery passes. The vertical beam size also exhibits a small increase within the energy recovery passes, but now significantly at the spreaders and recombiners. Therefore it can be concluded that the increase of the relative momentum spread causes the

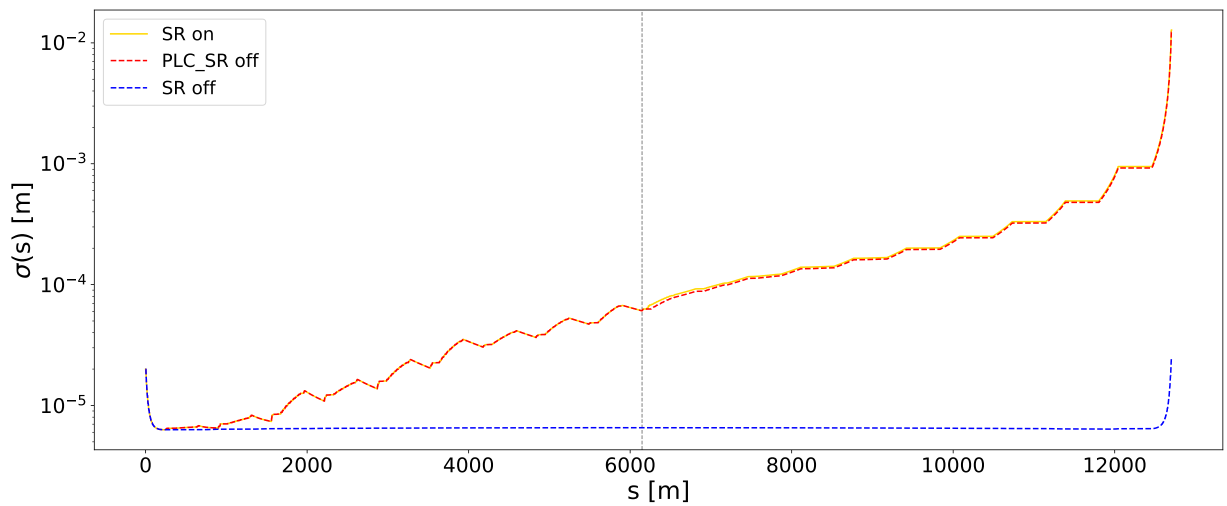

FIG. 38: The beam energy spread variation for three scenarios plotted in logarithmic scale: (yellow) incorporating SR losses at beamline elements, (red) turning off SR losses at the PLC dipoles, (blue) turning off SR losses at all elements.

beam size growth.

Apart from the adiabatic anti-damping, radiation losses observed in the arcs contribute to the observed beam size growth. Radiation losses increase the energy spread of the beam, leading increase in momentum offset, and the relative momentum spread evolution on the designed ten pass beamline is illustrated in Figure 38. The $\delta(s)$ values are plotted in a logarithmic scale. The red and yellow curves represent the $\delta(s)$ variation, taking the synchrotron radiation losses accounted, where the red curve represent the $\delta(s)$ with turning off the synchrotron radiation losses in the four dipoles in path length chicane. The blue curve represents the $\delta(s)$ evolution when there is no radiation losses, which is closely a symmetric behavior. This curve represents the ideal energy spread variation in an ERL.

The beam acceleration conducted was on-crest, without the use of any additional bunch length compression techniques. A reduction in the $\delta(s)$ is observed in all three scenarios, specifically during the first pass through the North linac, which clearly demonstrates the adiabatic damping in longitudinal space. The relative momentum spread exhibits a gradual increase in low-energy arcs, where the energy loss due to radiation remains below 1 MeV. However, once the beam energy surpasses 1 GeV, the relative momentum spread increase at arcs is visible in this figure. Furthermore, the gradients of the $\delta(s)$ slopes increases as the beam energy progresses along the accelerating beamline.

It is worth noting that $\delta(s)$ slopes with negative gradients are observable within the accelerating linacs. Nevertheless, this damping effect cannot fully counteract the increase in $\delta(s)$ attributed to synchrotron radiation. The black-dashed vertical line marks the end of the five accelerating beamline, and the subsequent downstream beamline exhibits increase in the $\delta(s)$. The positive gradient slopes are indicative of the linacs, where energy recovery takes place. The figure clearly illustrates that the $\delta(s)$ blows up at the tenth linac pass, where the lowest energy beam passes within South linac while decelerating.

The redesigned ten pass ER@CEBAF beamline exhibits closely matched Twiss functions and the observed beam sizes are within reasonable limits, with no recorded particle losses. However, it is essential to recognize that synchrotron radiation losses play a significant role in beam transportation, necessitating the implementation of an energy compensation mechanism. Effective control of the momentum spread is necessary to mitigate the observed growth, and this can be achieved by manipulating the longitudinal phase space.

From an operational perspective, mitigation and correction of dispersion closure within regions of trajectory bends is important. Lowering dispersion results in a reduction of relative momentum spread within the corresponding regime. Therefore, a dedicated beam study was conducted to establish the methodology for addressing this issue in the two lowest energy CEBAF arcs. The following chapter offers an in-depth analysis of this beam study.

CHAPTER 7

LOW DISPERSION ARCS

In CEBAF, arcs 1 and 2 are the lowest energy arcs in the east and west arc areas respectively. In the 2023 CEBAF optics, Arc 1 and Arc 2 have mirror symmetric optics over the horizontal bend regions (Figure 39). The peak $D_x(\mathrm{s}) \approx 6.0\,\mathrm{m}$ for optimized diagnostics of momentum spread and energy diagnostics using the Synchrotron Light Monitors (SLMs). However, this large dispersion in the low-energy arcs limits the momentum aperture for decelerating beams in ER@CEBAF, necessitating design of a low dispersion arc option.

The low dispersion requirement for ER@CEBAF, for the increase of arc momentum aperture, leads to a four-fold symmetry magnet layout in the horizontal bend regime of all ten arcs. The requirements of having localized dispersions in either x or y planes within the arc segments allows the arc lattices to be achromats. Isonchonicity was ensured by constraining the net momentum compaction factor α_c to be zero over the entire arc; this in turn depends on the dispersion functions ($D(s)$) and the local dipole bend radii ($\rho(s)$) in the lattice.

Changing the M_{56} value of a lattice affects the localized dispersion, and fully isochronous lattices are obtained by tuning M_{56} to be zero. Using four-fold symmetric optics, we were able to lower the $D_x(\mathrm{s})$ peaks to approximately 2.5 m, a value similar to other CEBAF arcs, while maintaining overall arc isochronicity. SLM diagnostics for beam energy and energy spread still have sufficient resolution for CEBAF operations with these updated optics, and increased dispersion periodicity supports several possible locations for additional SLM diagnostics if needed.

Additionally, these optics provide improved orthogonality of horizontal dispersion $D_x(s)$ and M_{56}, enabling their independent correction. Hence the use of these low dispersion arc 1 and 2 optics is also being considered for 12 GeV CEBAF operations.

7.1 CEBAF ORBIT MEASUREMENTS

Identifying the sources of orbit deviation is crucial in beam transportation through an accelerator. Multiple factors can cause the beam trajectory to shift from its design orbit, such as magnet misalignment, focusing errors, and non-linear effects due to fringe fields in

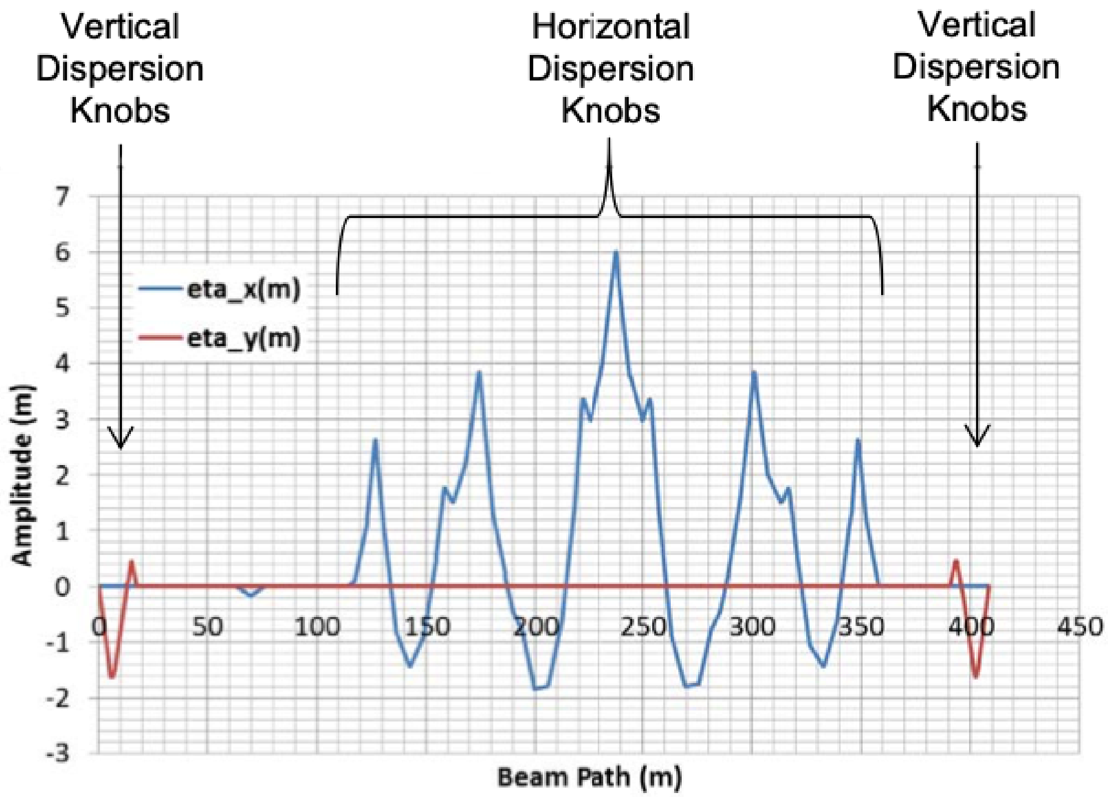

FIG. 39: 2023 operations CEBAF Arc optics, with large peak horizontal dispersion (blue curve) for improved energy monitoring resolution by a synchrotron light monitor located near the dispersion peak [15].

magnets. Beam position monitors (BPMs) use the electric field created by the beam to measure the transverse positions of the beam inside the beam pipe at the BPM locations. BPMs are also used to measure dispersion in CEBAF, through measurements of orbit deviations caused by intentional, controlled beam energy changes from design values.

Many BPMs are installed within the CEBAF beamline. These BPMs consist of four thin quarter-wave pick-up antenna wires, centered on the beam axis and placed symmetrically at the corners of a square that is perpendicular to the beam. There are two types of quarter-wave BPMs installed in the beamline. M20 BPMs have larger apertures (4.7 cm) and are installed within the Arc 1 and Arc 2 beamlines and at the extraction regions. M15 BPMs have smaller apertures (3.5 cm) and are used in the linacs and elsewhere. The schematic layout of a CEBAF quarter-wave BPM is given in Figure 40 [45].

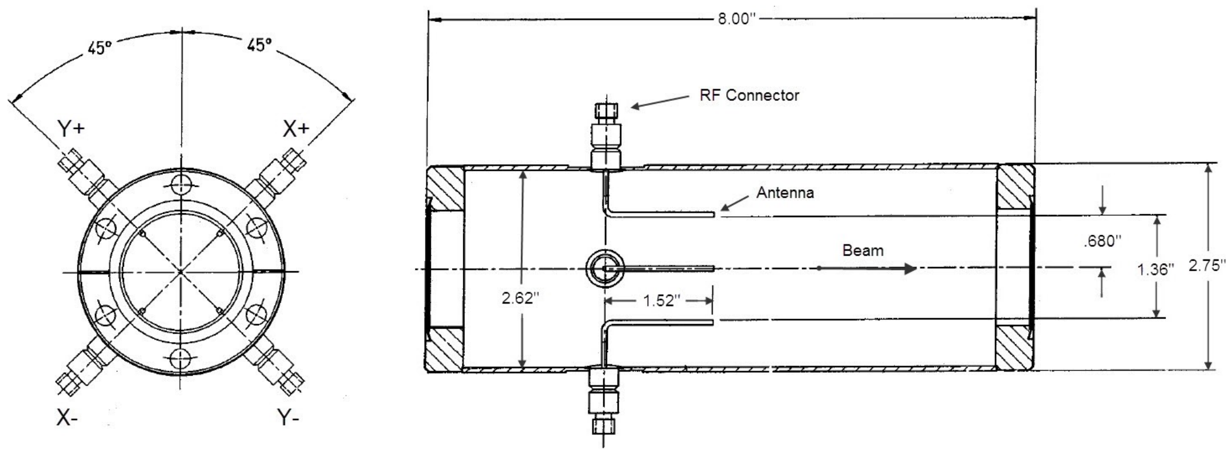

FIG. 40: Schematic drawing of a quarter-wave antenna style BPM [45].

The electron beam exhibits a micro pulse structure with the RF frequency of 1497 MHz, generating an electric field that interacts with the quarter-wave antenna pickups located inside the BPM enclosure. The beam position is proportional to the difference of the voltages divided by the sum of the voltages

$$r \propto \frac{V^+ - V^-}{V^+ + V^-} = \frac{\Delta}{\Sigma}. \tag{74}$$

Each BPM consists of two opposing pairs of antennas (X^+, X^-, Y^+, Y^-) and are oriented 45° to the lab frame, as a precaution of saving the antennas from the synchrotron radiation.

The beam positions of X and Y, in the rotated frame are denoted as X_{rot} and Y_{rot} are determined using the equation below

$$X_{\mathrm{rot}} = k\frac{(X^+ - X^+_{\mathrm{off}}) - (X^- - X^-_{\mathrm{off}})}{(X^+ - X^+_{\mathrm{off}}) + (X^- - X^-_{\mathrm{off}})}. \tag{75}$$

A similar equation is used to calculate Y_{rot}, using $'k'$ as a proportional constant. The $\alpha_{x,y}$ - relative gain ratios and $X^{\pm}_{\mathrm{off}}$ and $Y^{\pm}_{\mathrm{off}}$ are measured by an RF calibration signal to one of the antennas. To measure α_y an RF signal is applied to the X^- antenna and the values can be calculated using the following equations

$$\alpha_x = \frac{X^+ - X^+_{\text{off}}}{X^- - X^-_{\text{off}}}, \tag{76}$$

$$\alpha_y = \frac{Y^+ - Y^+_{\text{off}}}{Y^- - Y^-_{\text{off}}}. \tag{77}$$

To obtain the position of the beam centroid in the lab frame, the BPM frame needs to be rotated 45°. The beam position values after rotation of 45° is calculated using the following relation

$$\begin{pmatrix} X \\ Y \end{pmatrix} = \frac{1}{\sqrt{2}} \begin{pmatrix} 1 & -1 \\ 1 & 1 \end{pmatrix} \left[\begin{pmatrix} X_{\text{rot}} \\ Y_{\text{rot}} \end{pmatrix} - \begin{pmatrix} X_{\text{rot,off}} \\ Y_{\text{rot,off}} \end{pmatrix} \right]. \tag{78}$$

Here, $X_{\text{rot,off}}$ and $Y_{\text{rot,off}}$ are the offsets in the rotated coordinate frame. The BPM readouts determine the corrector strengths required to apply for orbit correction when the beam motion is off-axis [46], and screens displaying BPM position changes from beam energy changes were used in the beam study to directly measure and correct arc dispersions.

7.2 BEAM STUDY

A dedicated beam study test plan was submitted to test beam optics of the low dispersion arc 1 and 2, with an associated optics correction procedure. This beam study was performed near the end of the CEBAF operations period in March 2023. The CEBAF linac energy gain per pass was 1047 MeV, constrained by a bypassed C100 cryomodule. The injector beam energy was correspondingly scaled to 117 MeV, to be compatible with the linac energy gain per pass.

During the beam study, beam was transported from the injector up to the 3R dumplet at the end of Arc 3. The symmetric test optics for arcs 1 and 2 with reduced peak horizontal dispersions are shown in Figure 41.

7.2.1 OPTICS INITIALIZATION

The beamline settings of the low dispersion optics beam test were saved in a dedicated workspace in the CEBAF control system. Quadrupole settings of Arc 1 and Arc 2 were loaded into the beam operation system from the saved directory. Following CEBAF operations procedures [47], we used the C laser (associated with the highest pass hall at the time) to generate a tune mode beam with a beam current of 6 µA. This tune mode beam current was

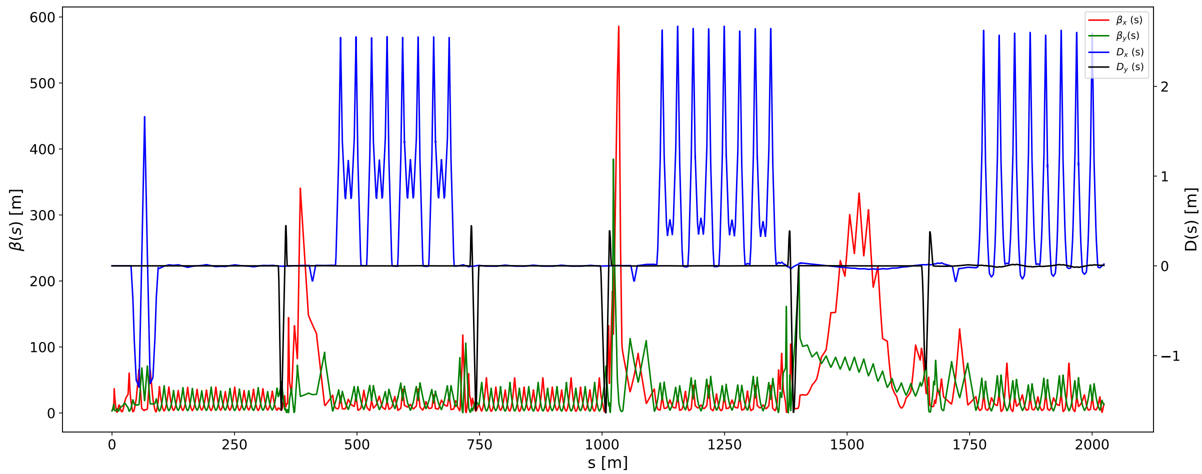

FIG. 41: Optics plot of the used beamline: injector to 3R dumplet.

sufficient to use all relevant CEBAF diagnostics for the study, particularly beam position monitors (BPMs) to measure the dispersion with the modified optics.

Prior the beam transport, all magnets were cycled with the application *HYST AREA* to reset their hysteresis curves. Path length corrections were performed using operations applications *Pathlength* and *DogCalc12* by following a CEBAF operations procedure [48]. Dogleg dipole magnets located in the arc 1 and 2 extraction regions were adjusted during the path length correction process. This is a routine process for initial beam tuning of CEBAF.

Dispersion measurements were performed by observing 30 Hz BPM orbit variations in the linacs, spreaders, arcs, and recombiners correlated with 30 Hz variations of a beam energy vernier. BPM screens are synchronized with this vernier to display position differences of orbits at different energies, effectively displaying scaled dispersion functions at these BPMs. During CEBAF operations, dispersion measurements and corrections procedures were performed following the *ORFP* optics procedure [47]. According to that procedure, a differential orbit amplitude of 7.5 mm at IPM1A21 on the Arc1 *Absolute* 30 Hz *BPM screen* was equivalent to the nominal design dispersion of $D_x = 6$ m.

Dispersive BPM variations in the CEBAF linacs and arcs up to $\approx 300\,\mu$m are acceptable during this procedure for both x and y planes. This can be acceptably exceeded in the horizontal arc BPMs, requiring horizontal dispersion correction for the corresponding arc.

Vertical dispersion correction procedures followed steps in the [47] standard operations correction procedure, as the low dispersion arcs have similar D_y(s) function variation to the standard 2023 CEBAF optics. We first proceeded with D_y(s) correction, maintaining the existing design vertical orbits in each arc. For Arc 1, the 1S01 quadrupole was adjusted to minimize the vertical dispersion leakage and restore the 1S vertical spreader achromat. The 2S01 and 2R10 quadrupoles were adjusted to similarly restore the 2S vertical spreader achromat.

However during the beam study, vertical dispersion correction led to a large change in the field integral ($B.dl$) of 2S01, which in turn led to a considerable orbit distortion in the 2S region that we did not have time to entirely correct. We decided to forego the 2S spreader vertical dispersion correction as the dispersion correction was not very large, and focus on horizontal dispersion correction for the new arc 1 and 2 optics.

We then proceeded with horizontal dispersion ($D_x(s)$ corrections for this low-dispersion optics. A special correction procedure was written, since optics including horizontal dispersions were different than the nominal CEBAF design optics in Arcs 1 and 2. Instead of the differential orbit amplitude of 7.5 mm, the new optics required an amplitude of 2.45 mm at the BPM IPM1A18. Moreover, for the dispersion correction, new quadrupole combinations listed in Table 10 were used to maintain optical symmetry.

TABLE 10: New D_x(s) Correction Quadrupoles For March 2023 Beam Study.

Arc	D_x(s) correction quads
Arc 1	1A35, 1A38
Arc 2	2A35, 2A38

Figures 42 and 43, is the snapshot of the *30 Hz BPM Screen of Linac 3* before and after horizontal dispersion correction of both arcs. The observed BPM readings in Linac 3 suggest that the D_s(s) correction procedure of Arc 1 and Arc 2 were successful. A small

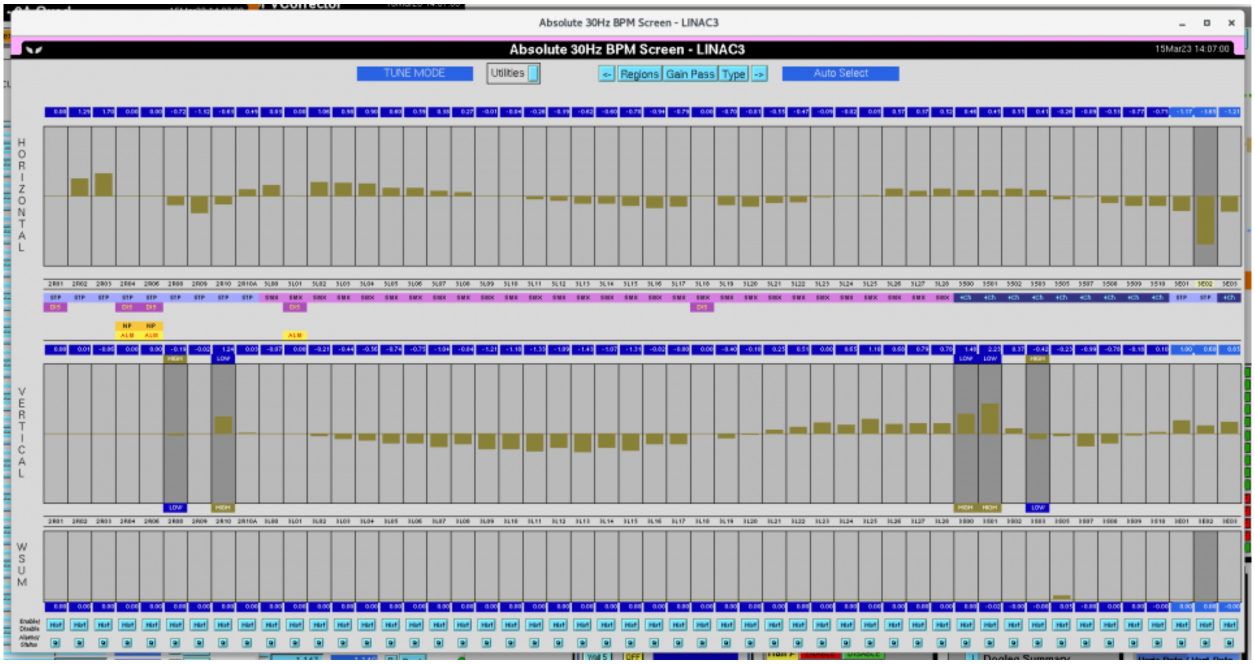

FIG. 42: 30 Hz BPM screen of Linac 3 before horizontal dispersion correction.

D_y(s) leak observed in Linac 3 remained after backing out of the 2S vertical dispersion correction mentioned earlier. Limited beam study time was the main limiting reason for not re-correcting vertical dispersion in Arc 2, but we expect that proper D_y(s) closure and orbit correction would be feasible with more setup time.

7.3 M_{56} MEASUREMENT AND CORRECTION

The low-dispersion Arc 1 and Arc 2 optics have M_{56} values of 1.79 mm and 2.72 mm respectively. The third portion of the beam study involved measurements and correction of the M_{56} values of these two arcs after dispersion closure and orbit corrections.

The M_{56} measurement procedure followed the steps listed in [47]. Operations applications *NLPathlength, EnergyLocks, and MyaPlots* are used in this process. Special quadrupole magnet groups were defined to correct M_{56} for the modified optics as listed in table 11 [49].

First, M_{56} measurements of Arc 2 were performed. A relative momentum offset $dp/p = 0.001$ was applied to Arc 2 and allowed to settle. During this time Arc 1 dp/p value was

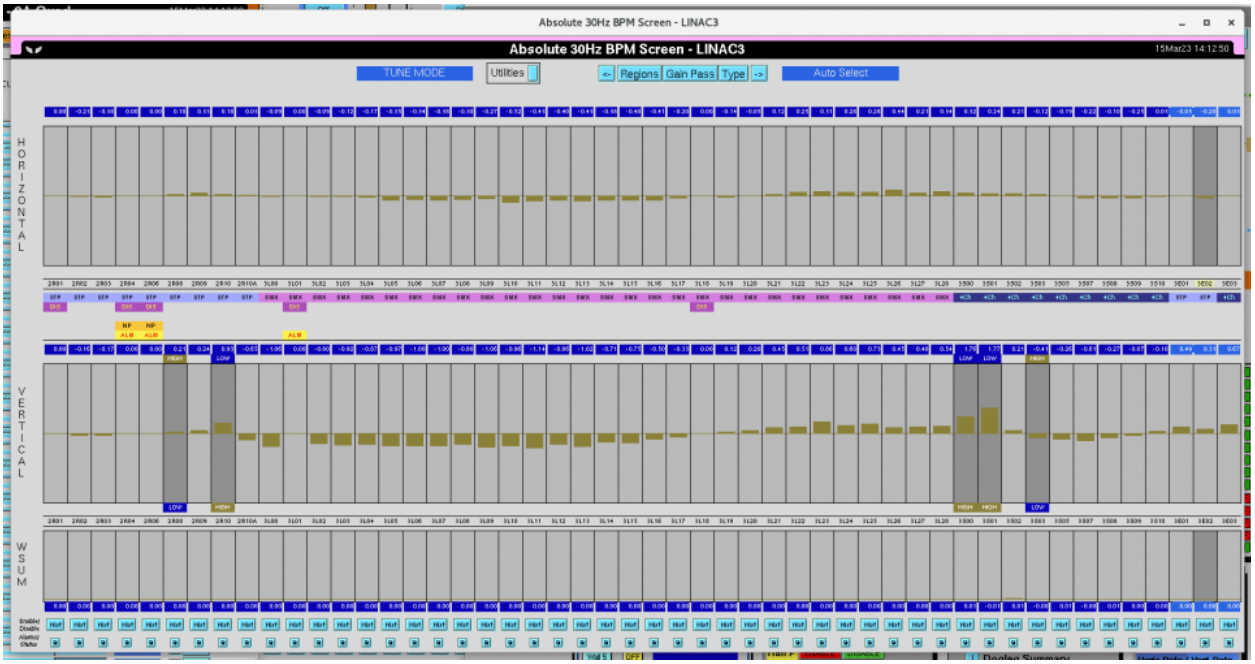

FIG. 43: 30 Hz BPM screen of Linac 3 after horizontal dispersion correction.

TABLE 11: New M_{56} Correction Quadrupoles.

Arc	Correction quadrupoles
Arc 1	1A04, 1A08, 1A14, 1A18, 1A24, 1A28, 1A34, 1A38
Arc 2	2A04, 2A08, 2A14, 2A18, 2A24, 2A28, 2A34, 2A38

kept at zero. Eq. (79) was used for the calculation of M_{56}:

$$M_{56}[m] = \frac{\text{(M56N:PEAK2\_after - M56N:PEAK2\_before)/1000}}{\text{ARC2:dpp\_after - ARC2:dpp\_before}}. \tag{79}$$

The observed M_{56} deviation was less than 0.2 mm; Figure 44 illustrates the variation of dp/p and M_{56} signals.

The calculated M_{56} value is 7.56 ± 7.83 cm, using the formula given in Eq. (79). The correction quadrupoles listed in table 11 were adjusted by applying an additional magnetic

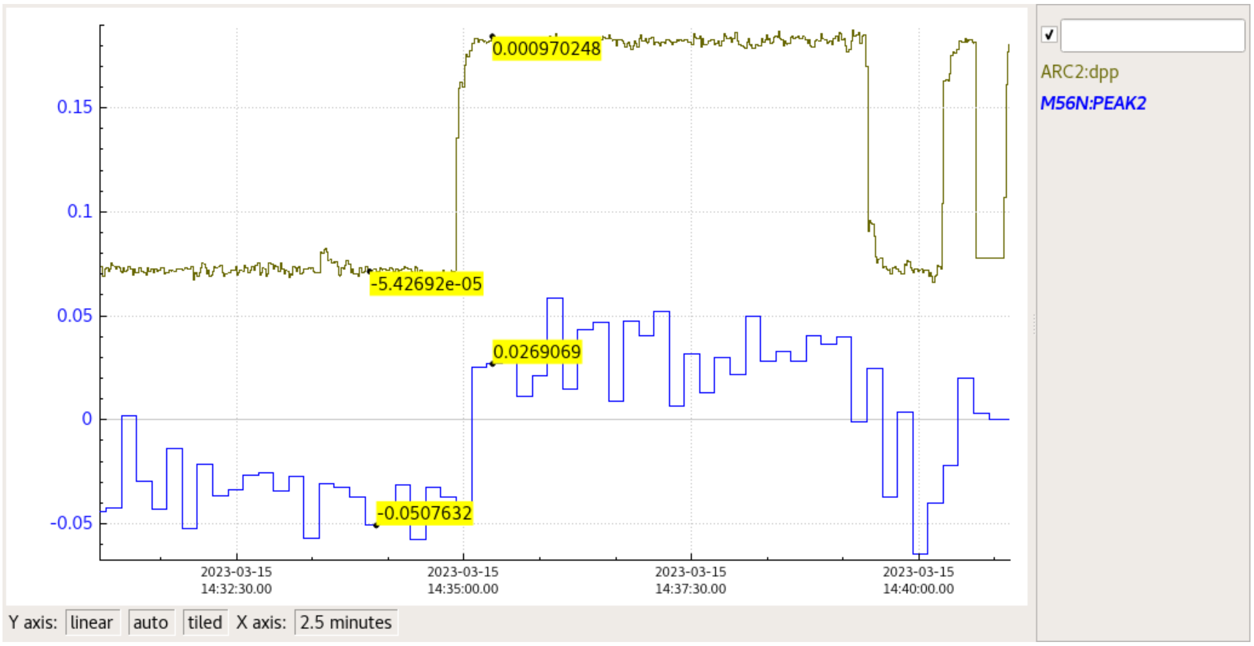

FIG. 44: M_{56} signal variation corresponding to the applied momentum offset for Arc 2.

field of -110 Gauss at each quadrupole to correct the small variation in Arc2 M_{56}. The correction process was done quickly, as expected, and the Arc 2 M_{56} and dp/p signal variation after correction is illustrated in Figure 44.

Next, the M_{56} measurement and correction for Arc 1 was performed. As done for Arc 2, we applied an additional 0.001 relative momentum offset using the *EnergyLock*. The observed M_{56} signal response was a bit slow, but we observed that both the dp/p and M_{56} signal variations of Arc 1 were consistent with M_{56} being approximately 0 for Arc 1.

7.3.1 FAST OPTICS DATA ANALYSIS

The new transverse optics of arcs 1 and 2 were also measured during this beam study. This was done with beam orbit measurements using the operations Fast Optics (Fopt) tool that measures orbit changes from applying transverse dipole kicks to the electron beam. These kicks were applied using four air-core kicker magnets in Arc 1 that were installed in the original beamline in 1998 as a part of machine optics characterization tool named the 30 Hz system.

This Fopt tool and its associated application are routinely used during CEBAF beam

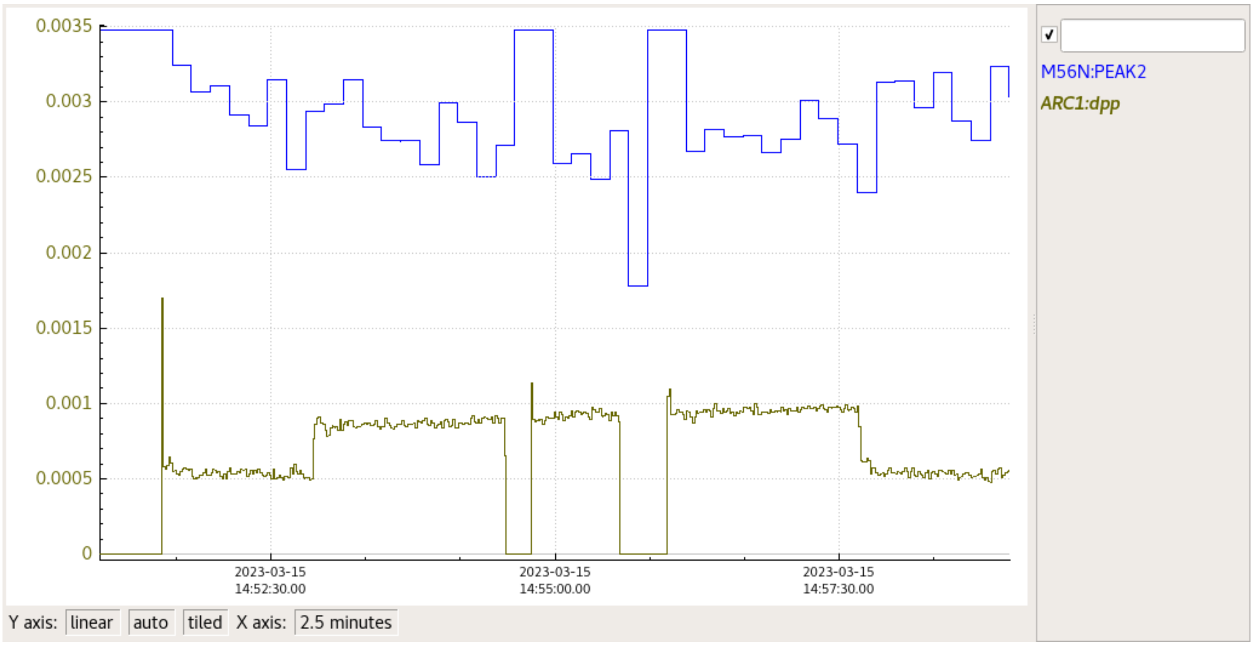

FIG. 45: M_{56} signal variation corresponding to the applied momentum offset for Arc 1.

operations to evaluate the beam optics changes through the machine after the Arc 1 spreader. The Fopt tool enables multiple orbit excitation schemes, as described in the manual [50]. The standard 1S region orbit excitation Fopt procedure was used during this study.

For the data collection on low dispersion arcs 1 and 2, a kick of 1.481 65 V was applied for all the transverse kickers and RF kickers in Fopt. Multiple sets of files with BPM readings through arcs 1 and 2 were created during a single Fopt data collection cycle.

Separate files for differential orbit data for the BPMs are created for each excitation applied. BPM data for coupling between transverse planes of the accelerator are generated for each kicker; these are named xfromyn.dat and yfromxn.dat. BPM readings for horizontal and vertical planes with RF excitation were saved in files energx.dat and energy.dat. Using the collected data within multiple orbit excitations, magnet and BPM misalignments, and magnet focusing errors, can be identified. Another tool named *CourantSnyder* is used to visualize the real-time optics of Fopt data collection. This helps the operator to identify any significant mismatches between model and beam optics.

Analysis of the collected orbit measurements was performed by comparing the collected machine data and orbit data to the Elegant beamline model. Required kicks at the excitation

TABLE 12: Required kick strengths to replicate orbit excitation in the lattice model.

Kicker magnet	Kick strength [mrad]
MAZ1S08H	-3.00E-02
MAZ1E01H	-3.00E-02
MAZ1S09V	-2.70E-02
MAZ1E01V	-4.50E-02

dipoles were determined by calculating predicted orbit variations in the model lattice using various Fopt corrector kicks. The next step was to determine orbit corrections from applying kicks in the model listed in Table 12:

After a comparison of corresponding orbits, we observed that all four orbits start to deviate at the end of the Arc 1 recombiner. Required orbit corrections and corrector magnets were then determined by through comparison between the model and measurements.

In the case of horizontal orbits, all the applied dipole corrector kicks were within the regions where vertical spreaders and recombiners. The corrector dipoles within the nearest downstream beamline at each kicker were employed for initiation of orbit correction. This procedure was iterated with additional corrector magnets until convergence. This orbit matching was independently performed, subsequently determining the necessary kicks for specific correctors capable of reproducing both excited orbits in each plane.

The data collected from the downstream beamline BPMs, as recorded in the differential orbit file, were utilized for comparison with the excited model orbit. Table 13 provides a breakdown of the required strengths of the corrector dipoles capable of replicating both horizontal orbit excitations initiated by S08H and E01H excitation kickers.

Figure 46, visually depicts the comparison between the corrected orbit and the orbit measurements of the BPMs, in the horizontal plane. The red circles on the diagram mark the positions of the nearest downstream BPMs for each corrector dipole. A small deviation during the second pass at the North linac was observed, which may be attributed to various factors. It is possible that defects in the BPMs or misalignment of the BPMs may lead to readings that are not 100% accurate.

Similarly, for the vertical plane, reproducing the excited orbits in the beamline model

TABLE 13: Required kick strengths to correct the horizontal orbit excitation in the lattice model.

Kicker magnet	Kick strength [mrad]
MBT1R09H	5.00E-02
MBT2S03H	1.30E-01
MBT2S10H	-1.15E-02
MBC3S05H	-3.00E-01
MBC3S10H	1.50E-01

followed a similar procedure as described. For reference, Table 14 provides a list of the required kick strengths for each vertical corrector dipole used in the process.

TABLE 14: Required kick strengths to correct the vertical orbit excitation in the lattice model.

Corrector	Kick strength [mrad]
MBT1R07V	6.0E-02
MBT2R07V	9.0E-02
MBT2R09V	-9.0E-02
MBC3S10V	-5.0E-02
MBC3A04V	2.3E-02

Figure 47 illustrates the comparison between the matched model orbit and the excited beam orbit obtained from the BPM readings. With regards to the horizontal orbit deviation,

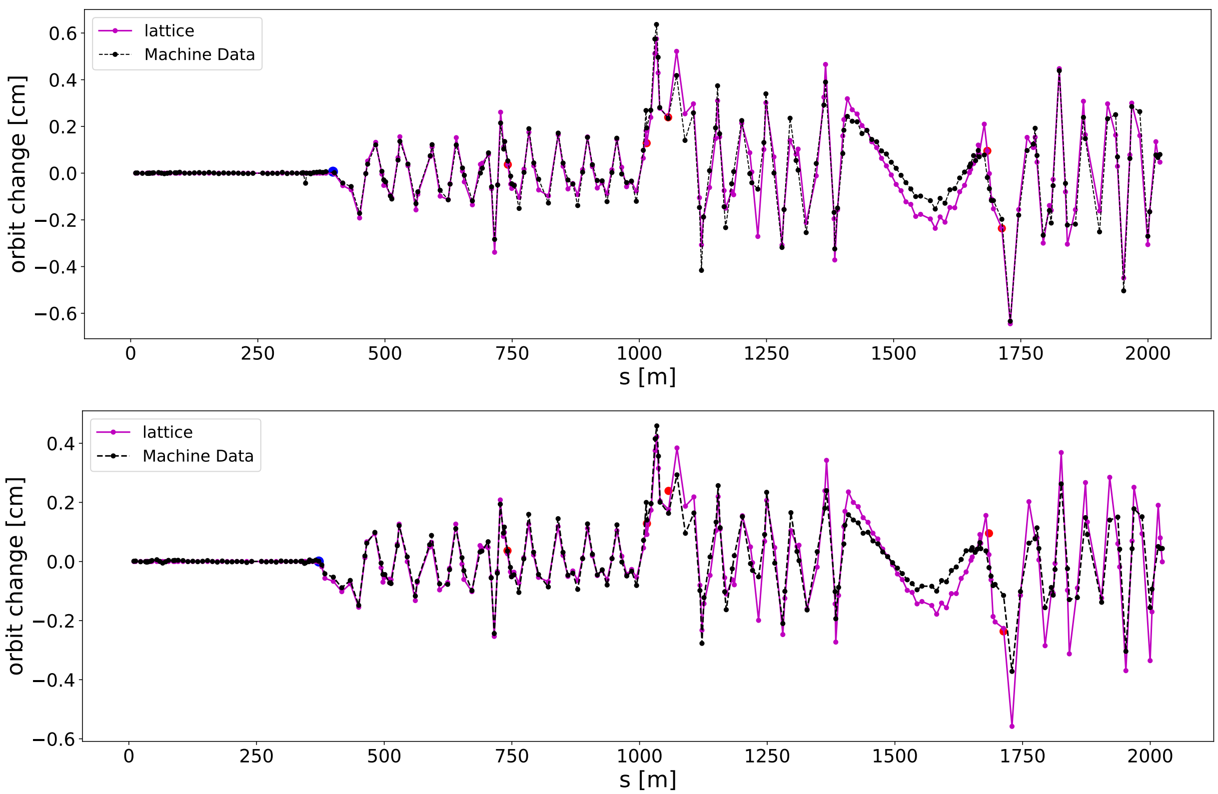

FIG. 46: Matched orbits with horizontal excitation, same corrector strengths are used to correct both orbit excitation from E01H and S08H kickers.

the corrector kicks utilized in the model originate from the areas where the beam trajectory exhibits curvature. In the plots, the red circles indicate the locations of the nearest downstream BPMs that correspond to each of the orbit-matching correctors listed in Table 14.

The Fopt data analysis is used to determine the gross optics errors. It is worth noting that a single Fopt data cycle can yield multiple degenerate solutions. The excited orbit data analysis is used to identify potential sources of beam excitation within the beamline. It's important to note that misalignments in dipoles have minimal impact since the force exerted on a particle does not depend on the position within the dipole. However, in the case of quadrupole magnets, particles at the center of the magnet are unaffected by the magnetic field. When particles are misaligned with a non-zero distance from the magnet center, they can experience additional dipole-like kicks from the quadrupole magnet. Furthermore, it is

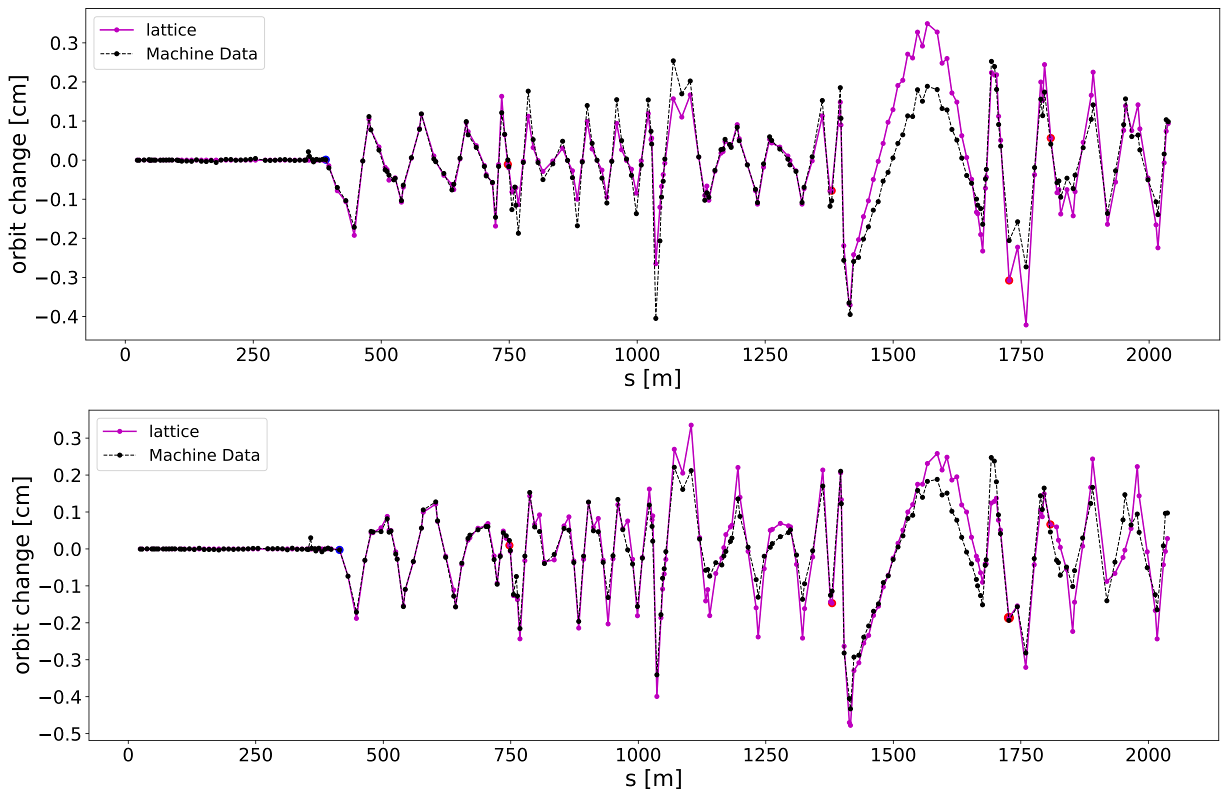

FIG. 47: Matched orbits with vertical excitation, same corrector strengths are used to reproduce both orbit excitation from S09V and E01V kickers.

worth noting that the quadrupole-focusing gradients may not be precisely matched with the design values. These magnets are of the electrostatic type, constructed with copper windings on an iron core. As a consequence, field errors are an inherent consideration in real-time beam transportation systems that make use of these magnets, potentially leading to orbit deviation [51].

Table 15 lists the applied percentage changes of the quadrupole focusing strengths in the model beamline which were necessary to achieve a similar orbit to the beam's actual path obtained from the BPM readings. Figure 48 illustrates the matched orbits for the two horizontal orbit excitations. Similar to previous plots, the blue color circles represent the nearest downstream BPM corresponding to excitation dipoles, while the red circles indicate the nearest BPM locations for the quadrupoles listed in the table 15. It is important to

TABLE 15: Percentage errors of quadrupole focusing strengths observed with horizontal orbit excitation.

Quadrupole	Percentage change of K1
MQL1R09	5.0 %
MQA2S02	5.0 %
MQA3S01	10.0 %
MQA3S03	15.0 %
MQA3S04	20.0 %

note that the changes listed in there are applicable to the orbit matching of both horizontal excitations.

Similar to the previous case, the third linac pass exhibits slight discrepancies, but reasonably matched orbits are observed elsewhere. These deviations may arise from either BPM misalignment or magnet misalignment, both of which can impact the phase of the beam.

When the *K1* values of quadrupole magnets change to replicate excitations in one plane, the Twiss functions in the other plane get affected too. Centroid motion, on the other hand, is impacted solely when the beam is not precisely centered on those quadrupole magnets, experiencing additional kicks. To achieve a vertical orbit match, it was necessary to deliberately misalign certain quadrupole magnets within the beamline to replicate the off-centered beam motion, without affecting the match in the horizontal orbits.

The vertical orbits align with the field errors as defined in Table 15. However, it was necessary to add a misalignment four quadrupoles in the vertical plane to achieve further matched orbits. The magnitudes of these quadrupole misalignments are listed in table 16 and there were no significant deviations observed in the horizontal orbits with these changes. The observed misalignment values are in mm range, which can be considered negligible and can be more challenging to correct in practical scenarios. The application of an additional kick could rectify the orbit excitation.

Figure 49 showcases a closely matched design orbit to the Fopt data. The positions of the misaligned quadrupole magnets in the beamline are highlighted with yellow circles.

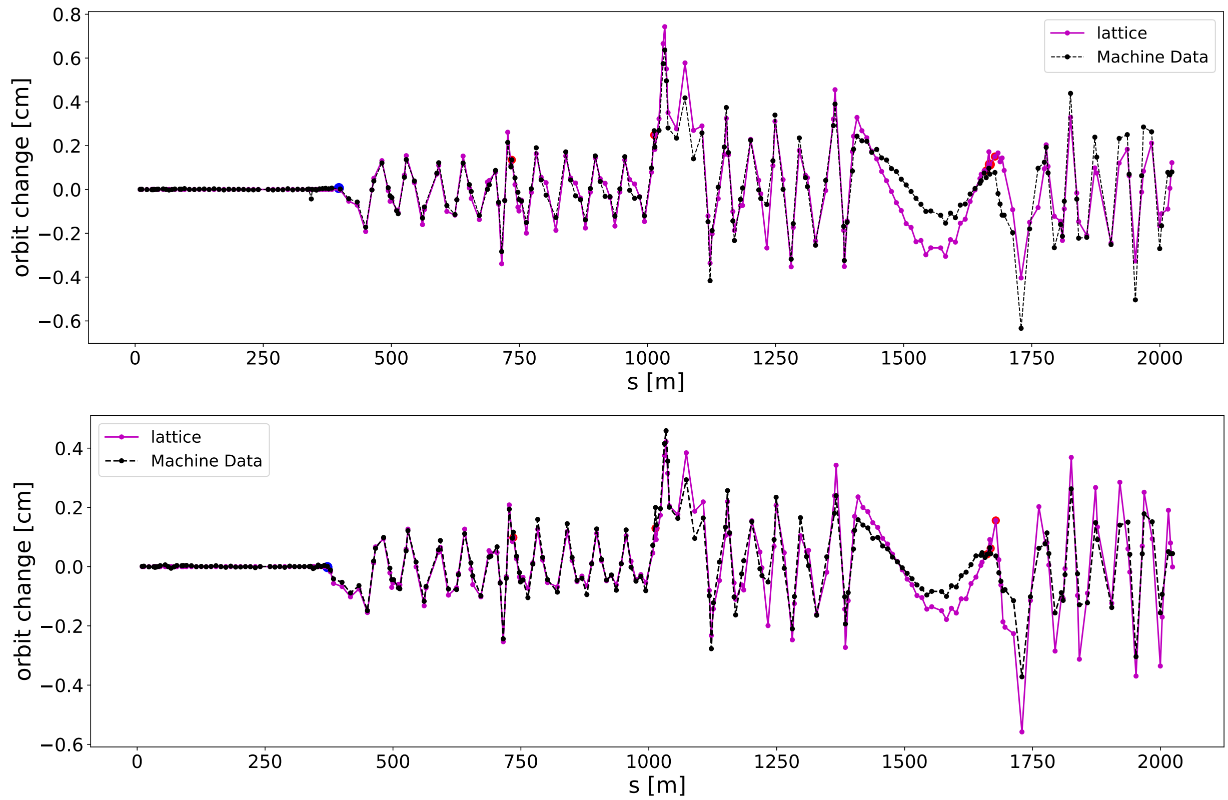

FIG. 48: Matched orbits with focusing field errors of quadrupole. Locations of the quadrupole magnets with field errors are marked with red circles.

Both vertically excited orbits closely correspond to the replicated focusing errors and misalignments. Consequently, these values represent one viable solution for orbit correction. However, validation of this obtained solution would involve another beam study, where the obtained results are utilized for orbit correction. Regrettably, due to time constraints, this task couldn't be demonstrated.

TABLE 16: Misaligned quadrupole magnets to obtain matched orbits with vertical excitation.

Quadrupole	Misalignment [cm]
MQC2S10	0.05
MQN1L00	0.01
MQA3S01	-0.02
MQA3S09	0.12

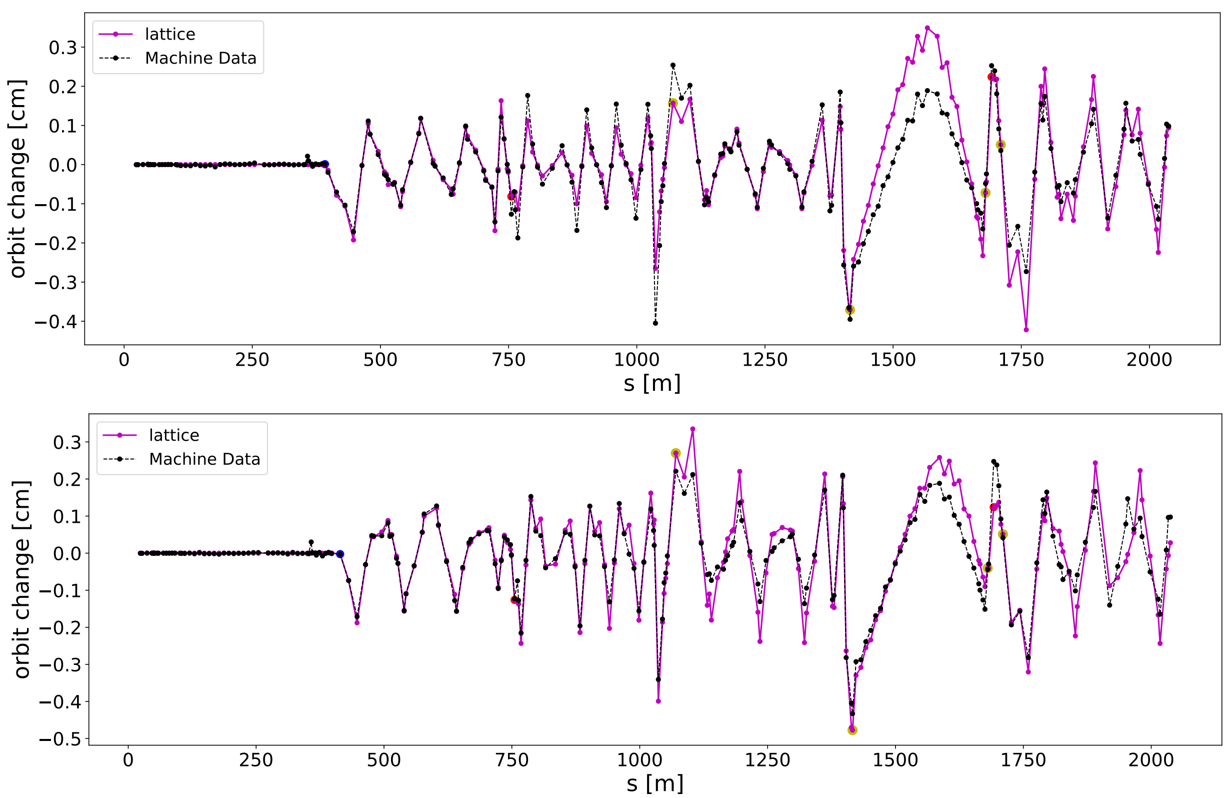

FIG. 49: Matched orbits with focusing field errors of quadrupole (red), and vertically misaligned quadrupole (yellow) in the beamline. Locations of the quadrupole magnets that are subjected to changes are marked with colored circles.

CHAPTER 8

CONCLUSIONS

The work presented in this dissertation focuses on the preliminary optics design for the ten pass energy recovery beamline for the CEBAF accelerator. The research goals were divided into two: first goal involve adopting and demonstrating of the use of MOGA techniques for lattice optics optimization and the second goal is to perform end-to-end simulation particle tracking analysis.

The optimization procedure for the linac lattice was carried out using a Python framework 'pymoo', which implements a Multi-Objective Genetic Algorithm search problem by integrating the 'NSGA-II' algorithm. Three objective functions were employed in this MOGA optimization process, and the resulting Pareto front from the search with a population of 500 individuals over 250 generations, was obtained as the final set of solutions. The North linac lattice elements were used in the special ten pass linac lattice arrangement used in the optics optimization process. The symmetry between the two CEBAF linacs proved to be advantageous, as solutions derived from the ten pass North linac lattice could be applied to formulate solutions for the ten-pass South linac lattice. However, the computational time emerged as a limiting factor in this optimization, due to the larger variable space. The MOGA optimization involving 30-variables was performed in the Jefferson Lab's scientific computing cluster, a meticulous consideration of the objectives employed and the permissible search space. The arcs require sharing of both the accelerating and decelerating beam passes, with the same energy. Despite the fact that the designed energies for corresponding passes are identical, the beam undergoes synchrotron radiation losses as its trajectory bends, resulting in the loss of a portion of its kinetic energy.

This leads to a slight energy mismatch in between the accelerating and decelerating beams. In addition to reducing the top beam energy, lowering the dispersion within the arcs allows for an increase in the momentum acceptances of each arc lattice. The introduction of the four-fold symmetry in to 180° horizontal bend region enabled a reduction in the horizontal dispersion in the two lowest energy arcs, Arc 1 and Arc 2. The isochronous arc lattices provide a path length equal to integer multiple of the CEBAF RF wavelength, ensuring beam synchronization at linac entrances. Moreover, arc lattices were designed as achromats to ensure that there is no dispersion leakage into the linacs.

The beam and the design Twiss parameters exhibit a close agreement within the ten pass ER@CEBAF beamline, particularly with on-crest acceleration. Nonetheless, it's important to perform careful modeling of the focusing elements within the regions with large $\alpha(s)$ values, to avoid potential statistical noise errors associated with the optics calculations. The tracking analysis was performed using `Elegant` particle tracking code. The beam size evolution, indicates a growth in relative momentum spread, which is a result of RF anti-damping effects during beam deceleration. The evolution of the beam energy spread and bunch length suggests the manipulations in the longitudinal space are necessary. Introduction of chirped beam, with few degrees off-crest beam transportation with proper bunch compression strategies is required [52].

8.1 FUTURE WORK

One of the primary goals of ER@CEBAF would be to experimentally investigate the scaling of collective instabilities of energy recovery linacs, such as beam-breakup (BBU) instabilities. A future study, with a specific focus on BBU instabilities, SRF higher-order mode (HOM) damping techniques, and their interplay with synchrotron radiation and adiabatic damping and undamping would be beneficial for the design maturity of this ten-pass ER@CEBAF beamline.

8.1.1 COMPENSATION OF SYNCHROTRON RADIATION

The performed comprehensive single bunch tracking analysis revealed a significant energy loss in high-energy arcs due to synchrotron radiation emission. The beam experiences a substantial energy reduction of approximately 30% following five energy recovery passes due to this radiation emission, which offers another plausible explanation for the observed increase in relative momentum spread.

To maintain stable beam orbits and prevent unwanted orbit excitation due to energy mismatches in the lattice and the beam, it is necessary to replenish this lost energy at each arc. Mitigating radiation losses can be accomplished by integrating RF compensation techniques, including the use of higher harmonic cavities. Conducting a future feasibility study to analyze the potential of RF compensation for the ten-pass ER@CEBAF beamline could address and resolve issues arising from radiation losses.

8.1.2 WAKE FIELDS AND HOM DAMPING

The two CEBAF linacs consist of 25 SRF cryomodules each and are designed to transport a maximum beam current of 100 µA. Exciting higher-order modes in these SRF cavities within the ten-pass ER@CEBAF beam transport structure could create substantial challenges in ensuring the stability of beam transportation. Such excitations carry the potential to induce wake field instabilities and BBU instabilities, ultimately resulting in beam losses. A future study involving identifying and analysis of possible HOM excitation resulting BBU and wake field instabilities in the ER@CEBAF beamline.

BIBLIOGRAPHY

[1] H. Wiedemann, *Particle Accelerator Physics* (Springer Cham, 2007).

[2] F. Mèot *et al.*, ER@CEBAF - A High-Energy, Multiple-pass Energy Recovery Experiment at CEBAF, in *IPAC2016* (2006).

[3] T. Agoh, CSR calculation by paraxial approximation, (2006).

[4] K. Wille, *The Physics of Particle Accelerators: An Introduction*, 1st ed. (Clarendon Press, 2001).

[5] S. Y. Lee, *Accelerator Physics*, 3rd ed. (World Scientific, 2011).

[6] R. Williamson, Accelerator physics, lecture 7, CERN Accelerator School.

[7] M. Tiegner, A possible apparatus for electron clashing-beam experiments, Nuovo Cimento **37** (1965).

[8] T. I. Smith, H. A. Schwettman, R. Rohatgi, Y. Lapierre, and J. Edighoffer, Development of the sca/fel for use in biomedical and materials science experiments, Nuclear Instruments and Methods in Physics Research Section A: Accelerators, Spectrometers, Detectors and Associated Equipment **259**, 1–7 (1987).

[9] D. W. Feldman *et al.*, Energy recovery in the los alamos free electron laser, Nuclear Instruments and Methods in Physics Research Section A: Accelerators, Spectrometers, Detectors and Associated Equipment **259** (1987).

[10] R. Hajima, Energy recovery linacs for light sources, Reviews of Accelerator Science and Technology **03**, 121–146 (2010), https://doi.org/10.1142/S1793626810000397 .

[11] L. Merminga, D. R. Douglas, and G. A. Krafft, High-current energy-recovering electron linacs, Annual Review of Nuclear and Particle Science **53**, 387–429 (2003), https://doi.org/10.1146/annurev.nucl.53.041002.110456 .

[12] C. Tennant, Energy recovery linacs, in *Challenges and Goals for Accelerators in the XXI Century*, Chap. Chapter 39, pp. 741–766.

[13] L. Merminga, *Synchrotron Light Sources and Free-Electron Lasers; Energy Recovery Linacs* (Springer Cham, 2016).

[14] C. Leemann, D. R. Douglas, and G. A. Krafft, The continuous electron beam accelerator facility: Cebaf at the jefferson laboratory, Annual Review of Nuclear and Particle Science **51**, 413–450 (2001), https://doi.org/10.1146/annurev.nucl.51.101701.132327 .

[15] M. Spata, Continuous Electron Beam Accelerator Facility Overview, USPAS Winter 2015.

[16] R. Kazimi, 12 GeV CEBAF Injector, Jefferson Lab User Group Annual Meeting 2012.

[17] M. Drury *et al.*, Cebaf upgrade: Cryomodule performance and lessons learned (2014).

[18] R. D. McKeown, The Jefferson Lab 12 GeV Upgrade, Journal of Physics: Conference Series doi:10.1088/1742-6596/312/3/032014 (2011).

[19] C. Tennant *et al.*, CEBAF-ER: extending the frontier of energy recovery at Jefferson Lab, in *Proceedings of the 11th Workshop on RF Superconductivity* (2008).

[20] C. Tennant, *Studies Of Energy Recovery Linacs at Jefferson Laboratory*, Ph.D. thesis, The College of William and Mary (2006).

[21] C. Adolphsen *et al.*, The development of energy-recovery linacs (2022), arXiv:2207.02095 [physics.acc-ph] .

[22] S. A. Bogacz *et al.*, ER@CEBAF: a test of 5-pass energy recovery at CEBAF 10.2172/1336057 (2016).

[23] K. I. Smith, R. M. Everson, J. E. Fieldsend, C. Murphy, and R. Misra, Dominance-based multi-objective simulated annealing, IEEE TRANSACTIONS ON EVOLUTIONARY COMPUTATION (2013).

[24] S. A. Bogacz , Challenges and opportunities of energy recovering linacs (2017), lAL Seminar, Orsay.

[25] R. T. Marler and J. S. Arora, Survey of multi-objective optimization methods for engineering, Structural and Multidisciplinary Optimization **26**, 369–395 (2004).

[26] A. Konak, D. W. Coit, and A. E. Smith, Multi-objective optimization using genetic algorithms: A tutorial, Reliability Engineering & System Safety **91**, 992–1007 (2006), special Issue - Genetic Algorithms and Reliability.

[27] X. Yu and M. Gen, *Introduction to Evolutionary Algorithms*, Decision Engineering (Springer London, 2010).

[28] D. Beasley, D. R. Bull, and R. R. Martin, An overview of genetic algorithms: Pt1, fundamentals, University Computing archive **15**, 58–69 (1993).

[29] M. Lukac and G. Krylov, Study of gpu acceleration in genetic algorithms for quantum circuit synthesis (2017) pp. 213–218.

[30] K. Deb, S. Agrawal, A. Pratap, and T. Meyarivan, A fast and elitist multiobjective genetic algorithm: Nsga-ii, IEEE Trans. Evol. Comput. **6**, 182–197 (2002).

[31] D. Pellegrini, A. Latina, D. Schulte, and S. A. Bogacz, Beam-dynamics driven design of the lhec energy-recovery linac, Phys. Rev. ST Accel. Beams **18**, 121004 (2015).

[32] J. J. Bisognano and R. L. Gluckstern, Multipass beam breakup in recirsulating linacs, CEBAF-PR-87-008 (1987).

[33] G. A. Krafft and J. J. Bisognano, Multipass beam breakup in the cebaf superconducting linac. (1986).

[34] D. Pellegrini, *Beam Dynamic Studies in Recirculating Machines*, Ph.D. thesis, École Polytechnique Fédérale de Lausanne (2016).

[35] S. A. Bogacz, Maximizing number of passes in recirculating energy recovery linacs (2016).

[36] I. Neththikumara, T. Satogata, S. A. Bogacz, R. M. Bodenstein, and A. Vandenhoeke, An evolutionary algorithm approach to multi-pass erl optics design, in *IPAC 21* (2021).

[37] I. Neththikumara, T. Satogata, S. A. Bogacz, R. M. Bodenstein, and A. Vandenhoeke, Linac optics optimization with multi-objective optimization, in *IPAC 22* (2022).

[38] J. Blank and K. Deb, pymoo: Multi-objective optimization in python, IEEE Access **8**, 89497–89509 (2020).

[39] M. Borland, *elegant, A Flexible SDDS-Compliant Code for Accelerator Simulation*, Advanced Photon Source LS-287 (2000).

[40] D. R. Douglas, R. C. York, and J. Kewisch, Optical design of the CEBAF beam transport system (1989).

[41] D. Hardy, J. Tang, M. Tiefenback, M. Crofford, and G. A. Krafft, Automated path length and M56 measurements at jefferson lab, in *IEEE* (1998).

[42] I. Neththikumara, T. Satogata, and S. A. Bogacz, Re-design of CEBAF optics for ER@CEBAF, in *IPAC 23* (2023).

[43] I. Neththikumara, *CEBAF arcs with tunable Momentum Compaction*, Tech. Rep. (Jefferson Lab, 2023).

[44] A. Camsonne *et al.*, A proposal for compton electron detector R&D, (2014).

[45] M. Spata, *Application of Chebyshev Formalism to Identify Nonlinear Magnetic Field Components in Beam Transport Systems*, Ph.D. thesis, Old Dominion University (2012).

[46] A. S. Hofler, B. A. Bowling, C. S. Higgins, P. K. Kloeppel, G. A. Krafft, and K. L. Mahoney, Performance of the cebaf arc beam position monitors, IEEE (1993).

[47] Y. Roblin, *Optics restoration & finalization procedure", CEBAF operations document MCC-PR-11-001*.

[48] M. Merz, *Pathlength measurement and correction procedure, CEBAF operations document MCC-PR-11-009*.

[49] I. Neththikumara, D. Moser, D. Turner, S. A. Bogacz, T. Satogata, and Y. Roblin, Beam study on low dispersion CEBAF arcs, in *IPAC 23* (2023).

[50] D. Turner, *Fast Optics (Fopt) Users Guide Version 7.0.1*.

[51] S. Peggs and T. Satogata, *Introduction to Accelerator Dynamics* (Cambridge University Press, 2017).

[52] G. P. Segurana, *Longitudinal Beam Dynamics and Longitudinal Matches in Energy Recovery Linacs*, Ph.D. thesis, Lancaster University (2021).

APPENDIX A

PROPER ELEMENT MODELS

The initial comparison of Twiss plots shows that there were significant mismatches between lattice and the beam $\beta(s)$ functions observed at the latter portion of the accelerating beamline, where the beam energy is larger. The initiation of the mismatches in the horizontal plane was observed to be the Arc 1 spreader, where the vertical bend was introduced into the beam trajectory. Mismatches are observed at all the vertical bend regions in the downstream beamline, and eventually mismatches at the high energy linac passes. Investigating the cause of these mismatches was carried out and found that the focusing elements in the lattice needs to be done properly. Quadrupole magnets are responsible for the focusing of the beam in transverse planes along the beamline. Hence an adequate number of integration steps defined as the parameter N_SLICES, needs to be added in the KQUAD definition.

The quadrupole magnets in this beamline use two different definitions. Quadrupoles in arc lattices use the focusing strength parameter ($K1$) and follow the definition as given below.

```
NAME: KQUAD, L=(double),K1=(double), SYNCH_RAD=(short), ISR=(short),
N_SLICES=(long)
```

The linacs transport multiple energy beams simultaneously due to their recirculating beam transportation strategy. Hence the focusing strength parameter cannot be used, as it includes the dependence on the beam momentum as given in Eq. (80).

$$K1 = \frac{eG}{pc} = \frac{1}{fl_q}. \tag{80}$$

Here, G is the field gradient, p - momentum, c - velocity of light, f - focal length of the magnet & l_q - length of the quadrupole magnet. Hence with $K1$ used, beam gets the same focusing strength disregarding its momentum. Therefore the applied magnetic field ($B_{\text{pole tip}}$) is used as a parameter in the quadrupole definition within the linacs.

$$B_{\text{pole tip}} = G \times \text{Bore Radius}. \tag{81}$$

Then the quadrupole magnets in the linac lattices are defined as follows;

NAME: KQUAD, L=(double), BORE=(double), B=(double), TILT=(double), SYNCH_RAD=(short), ISR=(short), N_SLICES=(long)

The rule of thumb for selecting the adequate number of integration steps is that the length of a slice needs to be significantly smaller compared to the focal length of a quadrupole magnet which can be calculated from Eq. (80). Hence the differences between the lattice and beam $\beta(s)$ function through the beamline were determined by varying the slice numbers in the quadrupole definition.

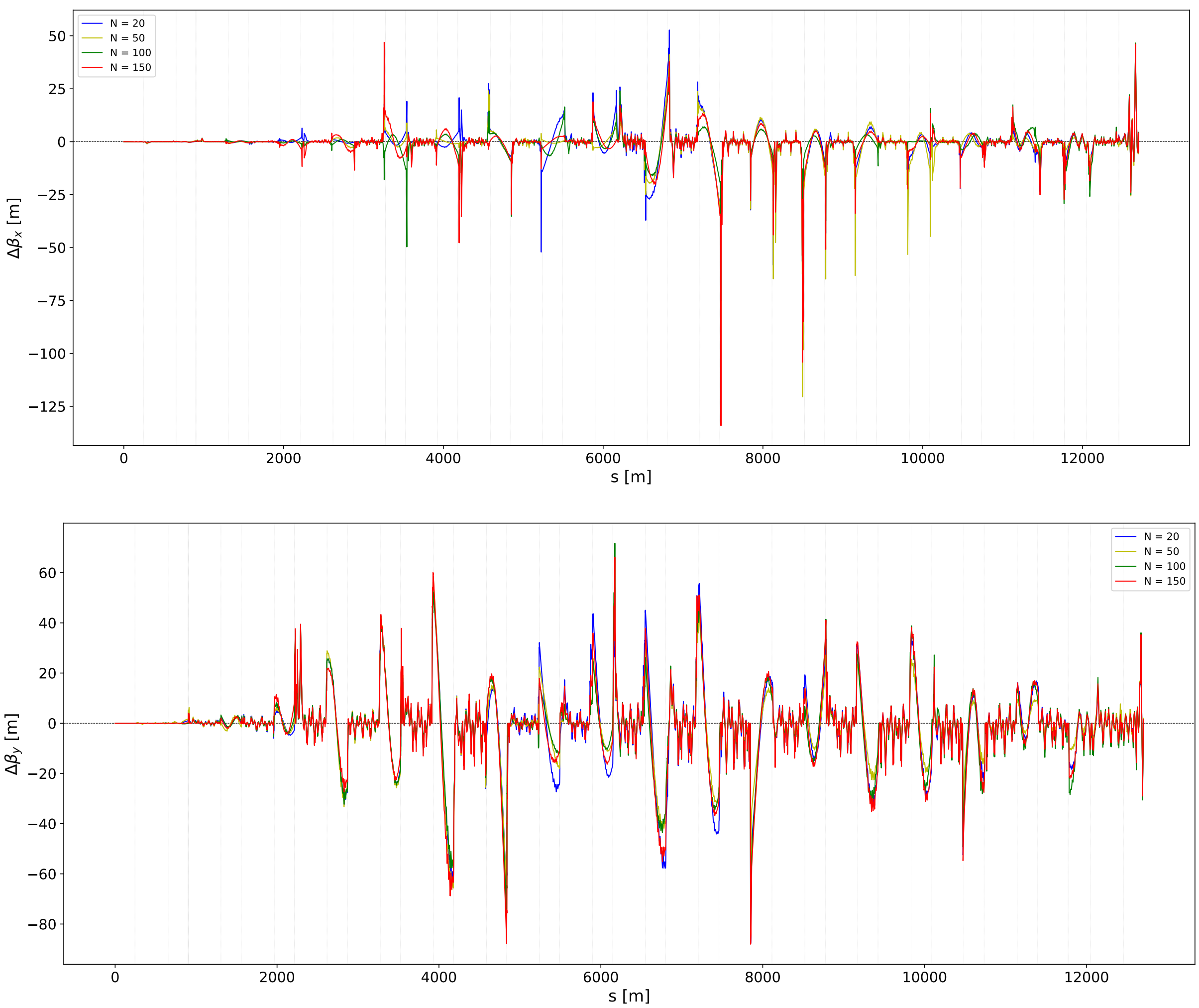

FIG. 50: Differences in β(s) with varying the N_SLICES parameter in quadrupole definition.

The plots in Figure 50 illustrate the differences between the $\beta(s)$ functions along the ER@CEBAF beamline, with varying the number of slices used in the quadrupole element definition. The plots indicate that with the increase of integration steps, beam-focusing models are closer to the design values in the linac regimes, but not much effective within the regions of vertical bends. The dashed vertical lines separate linac and arc lattices. The bottom plot illustrates the β_y differences and it shows no strong relation in between the slice numbers used.

The discrepancies of $\beta(s)$ in both planes are larger within the regions where the beam bends vertically. Dipole magnet modelling in the beamline uses CSBEND elements, where again proper number of slices are required. A similar analysis was carried out to determine the dependence on the integrations steps in dipole elements and the differences of the $\beta(s)$ functions in the x and y plane are plotted in Figure 51.

After these analyses,using a macroparticle distribution of 100,000 particles, beam Twiss values along the beamline is calculated and the results are presented in Chapter 6.

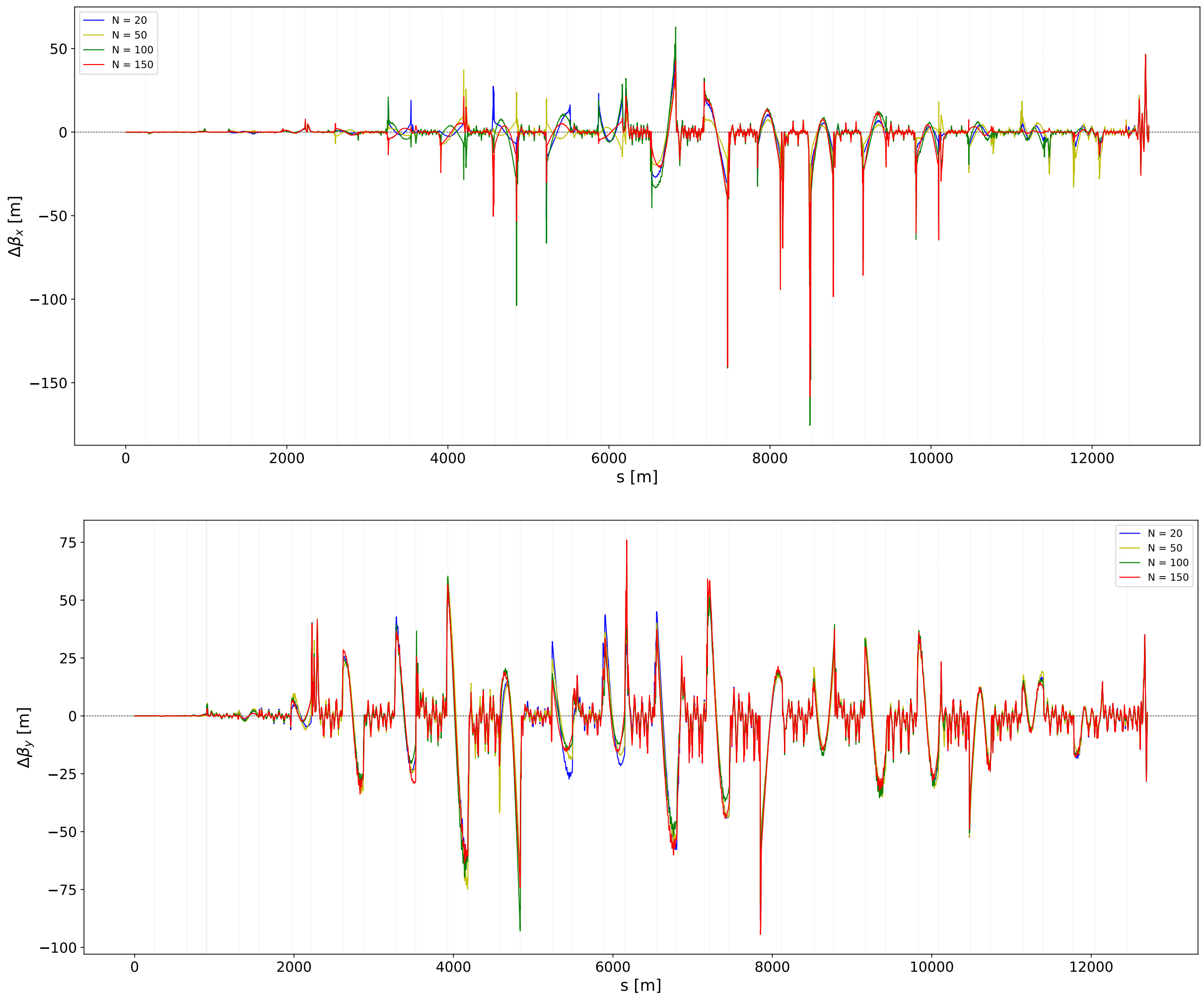

FIG. 51: Differences in β(s) with varying the N_SLICES parameter in dipole definition.

APPENDIX B

RADIATION LOSSES

A charged particle accelerates transversely and radiates photons via a phenomenon *Synchrotron Radiation.* In the classical definition, this radiation shrinks beam sizes by damping the motion of each particle reducing amplitude and action. But in quantum nature, emission of random photons excites each particle, causing amplitude and action increase resulting in beam size increase, hence in storage rings, equilibrium beam parameter definitions take these effects accounted.

The power radiated in the lab frame is given by,

$$P = \frac{1}{6\pi\epsilon_0}\frac{q^2 c}{\rho^2}\gamma^4. \tag{82}$$

Here, $\epsilon_0 = 1/(\mu_0 c^2)$ is the permittivity of free space, ρ is the bend radius, q is the charge of a particle, c is the speed of light and γ is the relativistic factor.

For a particle moving in a closed orbit, the total energy loss per turn is given as

$$U = \oint P(s)\frac{ds}{c}. \tag{83}$$

The ideal design value is

$$U_0 = C_g E_0^4 \frac{C}{2\pi}\left\langle G^2 \right\rangle. \tag{84}$$

Here, E_0 is the design energy, C is the error-free ring circumference, $G = 1/\rho$ is the local geometric bend radius and c_g is the convenient constant.

$$C_g = \frac{4\pi}{3}\frac{r_0}{(mc^2)^3}. \tag{85}$$

The value of C_g is approximated as:
$C_g = 8.85 \times 10^{-5}$ [m GeV^{-3}] : for electrons
$C_g = 7.78 \times 10^{-18}$ [m GeV^{-3}] : for protons
The energy loss per particle, per turn in isomagnetic ring is written as,

$$U_0 = \frac{C_g E_0^4}{\rho}. \tag{86}$$

For electrons this equation is written as:

$$U_0 = 88.5\frac{E_0^4}{\rho}\frac{[GeV^4]}{[m]}. \tag{87}$$

APPENDIX C

ELECTRON-ION COLLIDER PERFORMANCE STUDIES WITH BEAM SYNCHONIZATION VIA GEAR-CHANGE

C.1 ABSTRACT

Beam synchronization of the future electron-ion collider (EIC) is studied with introducing different bunch numbers in the two colliding beams. This allows non-pairwise collisions between the bunches of the two beams and is known as *gear-change*, whereby one bunch of the first beam collides with all other bunches of the second beam, one at a time. Here we report on the study of how the beam dynamics of the Jefferson Lab Electron Ion collider concept is affected by the gear change. For this study, we use the new GPU-based code (GHOST). It features symplectic one-turn maps for particle tracking and Bassetti-Erskine approach for beam-beam interactions.

C.2 INTRODUCTION

The Proposed Jefferson Lab Electron – Ion Collider (JLEIC) [1] is designed to accommodate a wide range of center of mass energies, from 21.9 GeV to 98 GeV. The ion beam energy varies in a range of 40-200 GeV and for electron beam it is 3-12 GeV. The figure-8 shaped electron and ion storage rings have nearly identical circumferences and intersect at two interaction points along two long straights, as shown in Figure 52

The electron beam is ultra-relativistic even for 3 GeV with a velocity of 0.99999971c, where c is the speed of light. But ion beam is not fully relativistic for low energy. This velocity difference in two beams causes a large difference of path lengths in the rings.

Both electron and ion rings are designed to match the revolution times of both beams at a specific center of mass energy (63.3 GeV). Then a particular ion bunch in ion-beam will collide with a same electron bunch at the interaction point (IP) for every turn.

This matching condition maintenance is impossible for the proposed large energy range due to non-relativistic ion velocities. Therefore, for lower energy values, bunches could

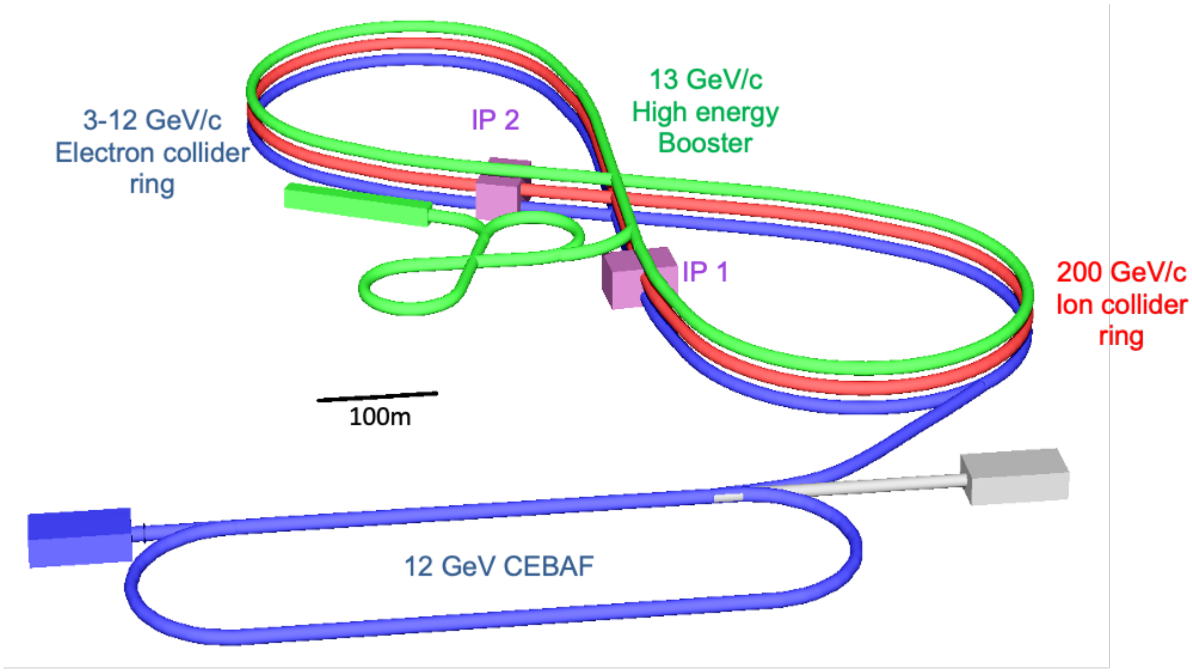

FIG. 52: JLEIC layout for 200 GeV ion ring.

miss each other at the IP due to different path lengths. This issue is known as beam synchronization and becomes more complicated if there is more than one IP in the machine as JLEIC.

Changing ring circumference is cumbersome and ex-pensive. Other implementations to resolve this issue involve variation of bunch numbers, variation of ion path length, variation of electron path length and RF frequency. As the difference of revolution time is equal to ion-bunch spacing, synchronization between beams can be achieved when ion ring accommodates additional bunches. This implementation allows non-pairwise collisions between bunches of two beams at the IR and is known as 'gear-changing' of bunches. In order to avoid parasitic collisions, bunch numbers should satisfy the following relation.

$$N_0\beta_0 = N\beta, \tag{88}$$

where N_0 is bunch number at the matched energy, N bunch number at the new energy, β_0 relativistic beta at matched energy and β relativistic beta at new energy.

For JLEIC, reference beam path lengths are defined for medium energy (ECM = 63.3 GeV) where, $E_{e-beam} = 5\,\text{GeV}$ and $E_{p-beam} = 100\,\text{GeV}$. The electron ring circumference is 2336.003 36 m. Relation between path lengths is,

$$L_{0-ions} = L_{0-elec}\,\beta_{0-ions}. \tag{89}$$

C.3 SIMULATION TOOLS

For this study GPU accelerated Higher Order Symplectic Tracking (GHOST) code was used [3]. In this code, particle tracking through a storage ring in six-dimensional phase space is carried out with arbitrary order symplectic Taylor maps. These maps were generated as in COSY Infinity with omitting zero-coefficient terms to speed up calculations and coefficients are found by,

$$x = \Sigma_{\alpha\beta\gamma\eta\lambda\mu} M\left(x|\alpha\beta\gamma\eta\lambda\mu\right) x^{\alpha} x'^{\beta} y^{\gamma} y'^{\eta} z^{\lambda} \left(\frac{dE}{E_0}\right). \tag{90}$$

For initial and final coordinates (q_i, p_i) and (q_f, p_f) the second kind of generating function satisfies the following relations : $(q_f, p_i) = J\triangledown F_2(q_i, p_f)$. Beam-beam kick calculation for both *strong-strong* and *strong-weak* modes is based on Bassetti–Erskine approximation. It enables solving Poisson equation, assuming collision of infinitely short bunches. This thin-bunch model is used by dividing the realistic bunch length into thin slices, thereby requiring slice-to-slice collisions. In the code, both bunches have same number of slices (M), and the slice size is $\Delta = L/M$, where, L is the bunch length. The collision of two opposing bunches at the interaction point (IP) is simulated as sum of the collisions of individual slices. Beam kicks experienced by two beams are calculated using the Basseti-Erskine.

C.4 BEAM PARAMETERS

Beam-beam interactions for JLEIC is studied for three essential kinematic ranges:

- Low energy range ($E_{CM} = 21.9\,\mathrm{GeV}$) with $E_p = 40\,\mathrm{GeV}$ and $E_e = 3\,\mathrm{GeV}$, where space-charge dominates.

- Medium energy range ($E_{CM} = 44.7\,\mathrm{GeV}$) with $E_p = 100\,\mathrm{GeV}$ and $E_e = 5\,\mathrm{GeV}$, where beam-beam interactions limit the luminosity.

- High energy range $E_{CM} = 63.3\,\mathrm{GeV}$ and $E_{CM} = 98\,\mathrm{GeV}$, where luminosity is affected mostly by synchrotron radiation of high energy electron beam.

For this study, beam parameters optimized for this medium energy are used to study how beam-beam interaction affects the collider performance in general.

Optimal working point for the preferred energy was found by performing tune-scans over a linear lattice model. From the tune diagrams, working points are found to be $\upsilon_x = 0.54$, $\upsilon_y = 0.567$, $\upsilon_s = 0.02$ for the electron beam and $\upsilon_x = 0.081$, $\upsilon_y = 0.132$, $\upsilon_s = 0.054$ for the proton beam. Generation of tune maps was done using BeamBeam3D; a massively parallel beam-beam code based on shifted Green's function to solve Poisson's equation. To achieve the desired high luminosity, JLEIC design relies on high repetition rate along with short bunch lengths. Luminosity of two colliding beams is calculated by:

$$L = \frac{n_b N_e N_p f_{rev}}{2\pi\sqrt{\sigma_{x-p}^2 + \sigma_{y-p}^2}\sqrt{\sigma_{x-e}^2 + \sigma_{y-e}^2}}, \tag{91}$$

where, n_b is number of bunches, N_e number of particles in e-beam, N_p number of particles in p-beam and $\sigma_{x,y}$ rms beam sizes in transverse directions. Also, smaller beam sizes are required for higher luminosity. Matching beam spot sizes at the IP is essential to minimize non-linear beam-beam forces and it is achieved by adjusting beta-function value at the IP (β^*).

C.5 RESULTS

For this study beam parameters listed in Table 1 were used.

TABLE 17: Beam Parameters Used for the Study.

Parameter	e-beam	p-beam
Energy	5 GeV	100 GeV
No. of Particles	3.7×10^{10}	1.38×10^{10}
$\beta{*}_x$	0.051 m	0.06 m
β_y^*	0.01 m	0.012 m
σ_x	21.77×10^{-6}	21.77×10^{-6}
σ_y	4.33×10^{-6}	4.33×10^{-6}
Bunch Length	0.008 m	0.012 m

First 1-to-1 bunch collision was studied, and it was verified that GHOST results are acceptable. Comparison was done using BeamBeam3D and the luminosity output from both are shown in Figures 53.

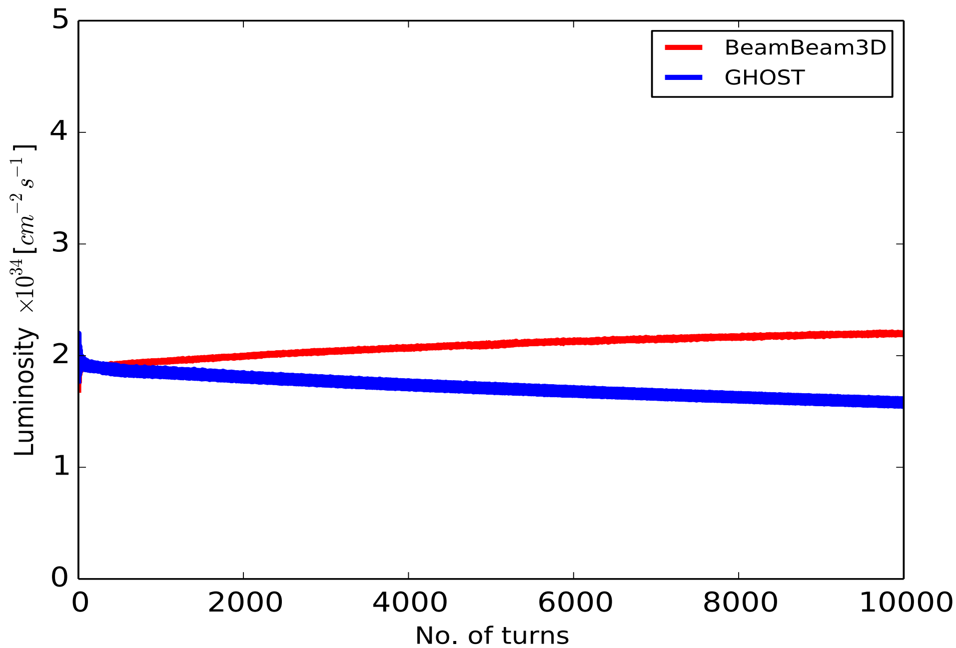

FIG. 53: Luminosity output for 1-on-1 collision from Beam-Beam3D and GHOST.

The expected peak luminosity value is 1.948 x 1034 cm-2 s-1 with hourglass reduction of 0.906. Hence the average luminosity is 1.76 $\times$ 1034 cm^{-2} s^{-1}, and from GHOST the average value is 1.86 $\times$ 1034 cm^{-2} s^{-1} and BeamBeam3D value is: 2.19 $\times$ 1034 cm^{-2} s^{-1}. Beam-Beam3D gives higher value than expected, as it takes into account the dynamic beta effect and this proves the work-ing points used are optimized for the symmetric design. For this simulation 1024K microparticles were used and each bunch is slices into 10 slices to facilitate slice-by-slice collision.

C.6 BEAM DYNAMICS WITH GEAR CHANGE

Let N_1 be the number of bunches in the proton beam and N_2 be the number of bunches in electron beam ($N_1 > N_2$). If they are relatively prime, there will be $N_1 \times N_2$ collisions for one iteration.

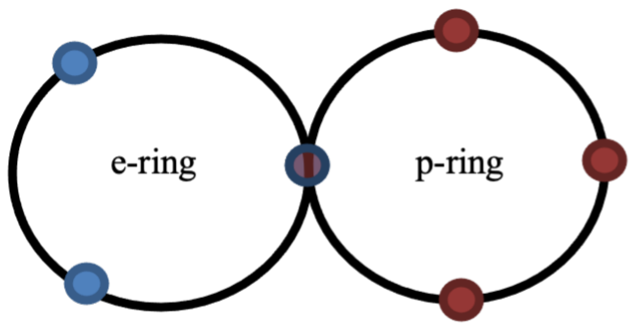

FIG. 54: Schematic for 4×3 bunch collision.

Since 3 and 4 are relatively prime, there will be $3 \times 4 = 12$ different pairs of bunch collisions. For JLEIC actual number of bunches required is over 3000. Simulating that much larger number takes a large computational time and memory. Therefore, this paper is focused on basic cases of bunch number variations. Currently, GHOST enables only 1×1 and $N \times (N-1)$ bunch collisions. Hence the cases studied are 4×3, 7×6 and 11×10. For each case, 5000 tuns were simulated with collision frequency of 1 and revolution frequency of 476 MHz. Luminosity output from GHOST is shown in Figure 4 below.

Above figure shows luminosity variation with respect to turn number for the cases mentioned above. According to these curves there is a large fluctuation of luminosity with a sudden drop in the beginning, but then they tend to stabilize after few thousands turns. Even though the system self-stabilizes, there is a small loss in luminosity. Luminosity loss increases with the increase of bunch number. Also, higher the bunch number, higher the initial luminosity fluctuation. The blue curve which corresponds to 11×10 has the lowest stable luminosity after around 2000 turns and the loss of luminosity is almost 4 times

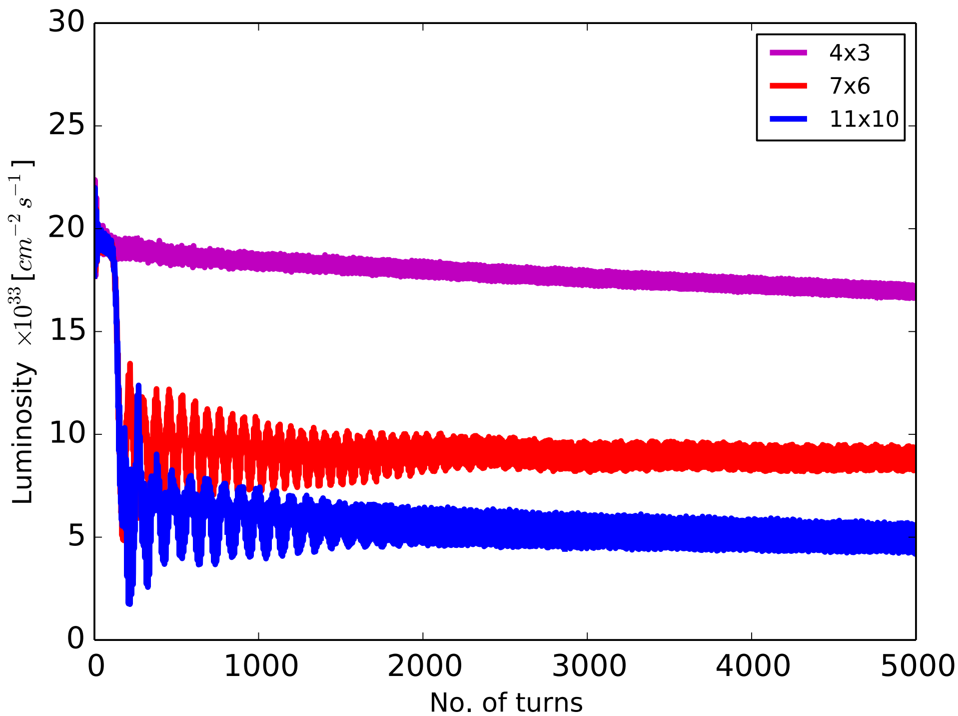

FIG. 55: Luminosity vs turn number for simple $N \times (N-1)$ gear-change.

compared with the 1×1. To benchmark these, simplest gear-changing simulation was done using BeamBeam3D and the comparison of luminosity results are given in Figure 56

Unlike 1-to-1 collision, with different bunch numbers the collisions are not symmetric as they collide with multiple bunches. These asymmetric collisions introduce complications to the beam dynamics in the collider ring. They can be categorized in to two types:

- Multi-bunch offset or dipole instabilities
- Multi-bunch beam size or quadrupole instabilities

These effects create linear and non-linear effects on beam stabilities, affecting transverse and longitudinal beam sizes and beam centroid offsets.

Working points were optimized for symmetric collisions, but with different bunch numbers (N) working points change. More resonances occur when the system operates at a point near to its theoretical working point, destabilizing two beams.

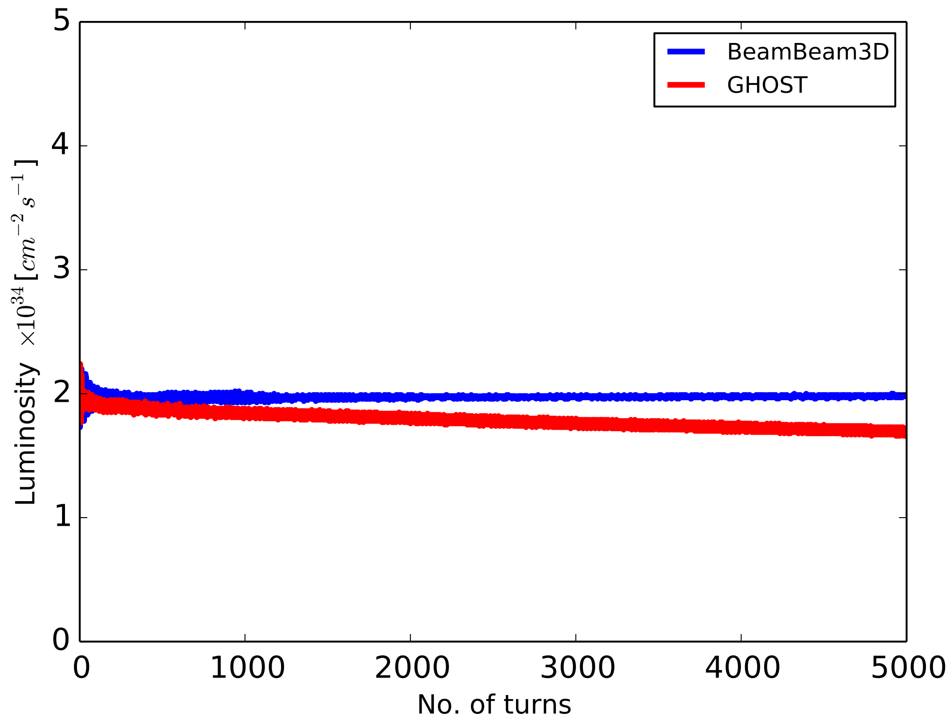

FIG. 56: Simplest gear-changing (4×3) luminosity output comparison of BeamBeam3D and GHOST

Various amount of oscillations at the beginning of luminosity curves reflect that the fixed working point used for the 1-to-1 collision is not optimized for different N values. Resonance strengths also vary as N value changes as there are different working points for different N values. These unwanted resonances can be minimized by optimizing tune for a range of $1/N$.

Dipole errors can be suppressed with the use of a feed-back system and recover a portion of luminosity loss. But correcting quadrupole instabilities need further study. To restore luminosity loss due to quadrupole and higher order instabilities, transverse damping methods are need-ed. These will be a focus of a future study

VITA

N. H. Isurumali Neththikumara
Department of Physics
Old Dominion University
Norfolk, VA 23529

EDUCATION:

- Master of Science (Physics), Old Dominion University, Norfolk, Virginia, USA, 2019
- Bachelor of Science (Physics), University of Peradeniya, Sri Lanka, 2015

AWARDS:

- Jefferson Science Associates graduate fellowship for the year 2022-2023

RECENT PUBLICATIONS:

- I. Neththikumara, S. A. Bogacz, T. Satogata, "Re-design of CEBAF optics for ER@CEBAF", International Partical Accelerator Conference Proc 2023, doi: 10.18429/JACoW-IPAC2023-WEPL056.
- I. Neththikumara, D. Turner, D. Moser, S. A. Bogacz, T. Satogata, Y. Roblin, "Beam study on low dispersion CEBAF arcs", International Particle Accelerator Conference Proc 2023, doi: 10.18429/JACoW-IPAC2023-WEPL055.
- I. Neththikumara, A. Vandenhoeke, R. M. Bodenstein, S. A. Bogacz, T. Satogata, "Linac optics optimization with multi-objective optimization", International Partical Accelerator Conference Proc 2022, doi:10.18429/JACoW-IPAC2022-MOPOTK050.
- I. Neththikumara, A. Vandenhoeke, R. M. Bodenstein, S. A. Bogacz, T. Satogata, "An Evolutionary Algorithm Approach To Multi-Pass ERL Optics Design", International Partical Accelerator Conference Proc 2021, doi:10.18429/JACoW-IPAC2021-WEPAB383

Typeset using LaTeX.